CHALMERS
UNIVERSITY OF TECHNOLOGY

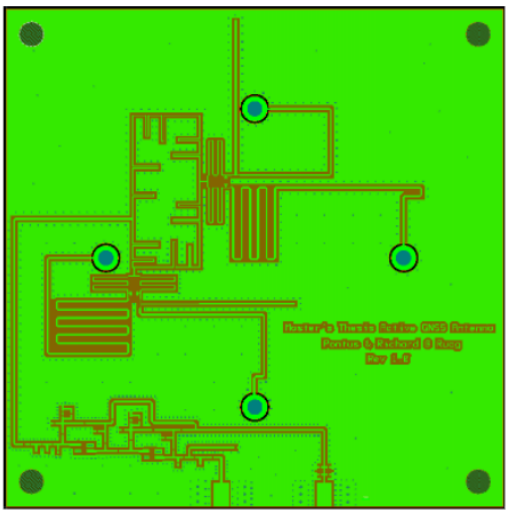

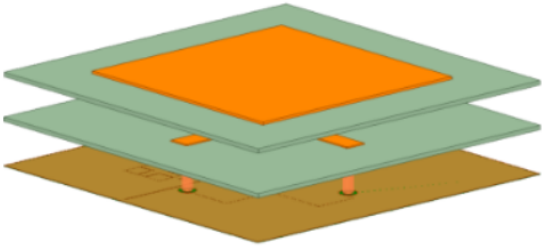

Active new space GNSS receiver antenna

The design of a circularly polarized antenna connected to a Low Noise Amplifier for the receiver stage of a space antenna targeted towards interstellar communications.

Master's thesis in Wireless, Photonics and Space Engineering

PONTUS LJUNGQVIST
RICHARD JELINEK

DEPARTMENT OF MICROTECHNOLOGY AND NANOSCIENCE
CHALMERS UNIVERSITY OF TECHNOLOGY
Gothenburg, Sweden 2022
www.chalmers.se

Master's thesis 2022

Active New Space GNSS Receiver Antenna

The design of a circularly polarized antenna connected to a Low Noise Amplifier for the receiver stage of a space antenna targeted towards interstellar communications.

PONTUS LJUNGQVIST
RICHARD JELINEK

CHALMERS
UNIVERSITY OF TECHNOLOGY

Department of Microtechnology and Nanoscience
Chalmers University of Technology
Gothenburg, Sweden 2022

PONTUS LJUNGQVIST
RICHARD JELINEK

Supervisors: Per Magnusson, Dennis Kleen and Richard Udiljak at beyond gravity
Examiner: Professor Jian Yang, Department of Antenna Systems/Communication.

Master's Thesis 2022
Department of Microtechnology and Nanoscience
Chalmers University of Technology
SE-412 96 Gothenburg
Telephone +46 31 772 1000

Cover: Layout of feeding network combined to LNA on the bottom layer (left) and the antenna (right).

Typeset in LaTeX
Printed by Chalmers Reproservice
Gothenburg, Sweden 2022

Abstract

This work concludes the design and construction of an active receiver antenna for interstellar communication between satellite communication systems in Low earth orbit (LEO) and Medium earth orbit (MEO). The work is intended as a breadboard design meaning that space classified parameters are not concluded for this work. Classical antennas consist of passive components connected to a receiver system via cables which introduces losses. By connecting the antenna directly to a low noise amplifier these losses can be removed to further improve the performance of the antenna. The work is separated to the antenna, feeding and amplifier section respectively. An axial ratio of 3 dB and return loss of 10 dB has been achieved for the entire GNSS bandwidth. Results are presented with and without the amplifier section present.

Acknowledgements

We would like to thank our supervisors at beyond gravity: Per Magnusson, Dennis Kleen and Richard Udiljak for all the help that they have provided during this project. We would also like to thank our friends and family for listening to our practice runs of our presentation. It has been a stressful time with a lot of ups and downs, but given the freedom to create anything we wanted has resulted in us gaining tons of knowledge which is the main objective for any Master Thesis.

Pontus Ljungqvist, Gothenburg, June 2022
Richard Jelinek, Gothenburg, June 2022

List of Acronyms

Below is the list of acronyms that have been used throughout this thesis listed in alphabetical order:

AR	Axial Ratio
BW	Bandwidth
CP	Circular Polarization
LNA	Low Noise Amplifier
RCHP	Right Hand Circular Polarization
LHCP	Left Hand Circular Polarization
MEO	Medium Earth Orbit
LEO	Low Earth Orbit
HFSS	
ADS	Advanced Design Systems
NF	Noise Figure

Contents

List of Figures

List of Tables

1
Introduction

Antennas come in a vast array of shapes and sizes, but how can the size be reduced while still retaining the original properties? This thesis focuses on two different areas of microwave engineering merged into one another. The design of a small wide-band right hand circular polarized (RHCP) antenna connected directly to a low noise amplifier (LNA) in order to reduce losses occurring due to signals travelling in long coaxial lines. Satellite communication has the disadvantage of signals suffering heavy attenuation due to the long distance travelled but also because of rain-droplets in the troposphere, ionospheric effects and losses due to long cables between the receiver and the amplifier to name a few examples. If the losses due to the distance the signal travels in coaxial cables from the receiver to the amplifier can be minimized, causing the overall attenuation to be decreased by a few decibel, the minimum input power to the antenna can be decreased meaning that the signal can travel even further before being indistinguishable from the noise floor, i.e the magnitude of unwanted background noise.

1.1 Aim

The scope of this thesis is to evaluate similar attempts and reports to manufacture an active antenna system with a low return loss over a dual-band characteristic. The dimensions of the entire system should be smaller than 10x10 cm to fit on a Sat-cube model, and preferably have the height minimized.

1.2 GNSS

Global Navigation Satellite System or GNSS is associated with a constellation of several satellites in space with the purpose of providing data containing time and position. The term GNSS is an umbrella term containing several satellite systems from different nationalities and is the "correct" term for what people most commonly refer to as "GPS" (Global Positioning System), the American GNSS system developed in the early 1970s and being fully operational in the 1990s. GNSS also includes other systems like the Russian GLONASS, China's BeiDou and Europe's Galileo. A number of other countries have also implemented their own regional satellite navigation systems to constitute the GNSS. What this enables is a complete worldwide coverage with an increased accuracy, integrity, continuity and availability towards the system.

For this Master Thesis, an antenna is desired for the lower GNSS band (1164-1214 MHz) and upper (1559-1610 MHz) with the listed specifications as can be seen in section 3.1. The GNSS bands consists of three major operators, GPS, GlONASS and Galileo, which can be seen in figure 1.1.

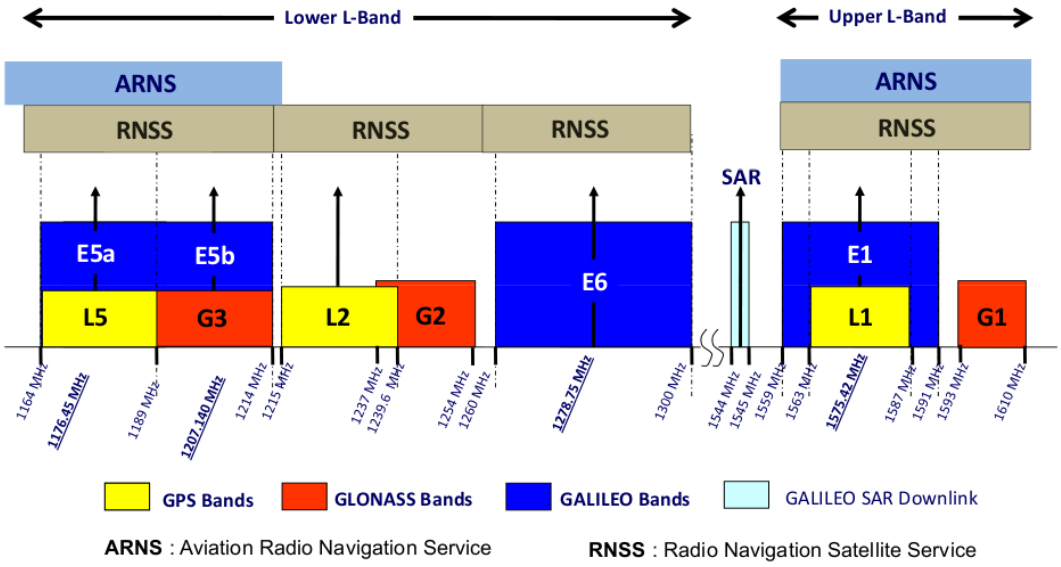

Figure 1.1: GNSS frequency-bands. [1]

2
Theory

This section gives a brief introduction to different concepts regarding antenna theory to give a better understanding to the method sections where an antenna, feeding network and LNA is constructed.

2.1 Antenna Fundamentals for GNSS

A receiver antenna is an imperative component for any communication system, where space and satellite communication poses further difficulties such as increased noise, signal attenuation due longer distances travelled and atmospheric interference. There are also multipath and interference effects that can cause a significant signal strength variability [14]. In GNSS systems RHCP is used as the standard mean of polarization for transmitting signals, meaning that both the transmitter and receiver are RHCP. Circular polarization is used due to it being the polarization that suffers the least from the attenuation caused while propagating through the rain droplets in the troposphere, while simultaneously being non-sensitive to Faraday rotation caused by the ionosphere [15]. CP also has the characteristic of suffering the least from any orientation mismatch between transmitter and receiver. The following are some of the key aspects of designing a GNSS antenna.

- Circular polarization
- Axial Ratio
- Bandwidth
- Gain

2.2 Electromagnetic fields

The source to any sinusoidal electromagnetic field [16] is a current that varies its direction over a time period, which results in an electromagnetic field that reverses its' polarity depending on the current direction. The electromagnetic field is most often characterized in the form below where the E and H field components of the EM field are separated:

$$\vec{E}\{x, y, z, t\} = \Re\{E(x, y, z)e^{jwt}\} \tag{2.1}$$

$$\vec{H}\{x, y, z, t\} = \Re\{H(x, y, z)e^{jwt}\} \tag{2.2}$$

where the E(x,y,z) and H(x,y,z) is the magnitude of a three-dimensional vector and e^{jwt} is the time variation.

2.2.1 Polarization

Polarization [16] is a term that characterizes how the wave propagates from transmitter to receiver in the far field region where the field can be described as a plane wave

$$W_{ave}(x,y,z) = \frac{1}{2}\Re\{E \times H^*\} = \frac{1}{2\eta}[E \times \hat{n} \times E^*] = \frac{1}{2\eta}[|E_x|^2 + |E_y|^2]\hat{z} \tag{2.3}$$

where the E_x, E_y and H_x, H_y define the polarization of the electric and magnetic field respectively. There are three different definitions of polarization: linear, circular and elliptical polarization. For all three cases there are co-polar and cross-polar polarization apparent, i.e wanted and unwanted polarization that are characterized differently depending on what type of polarization the transmitted wave possesses. The E-field of a vertically linearly polarized wave (y-polarized), assuming that the y-axis is located vertically and x horizontally while being orthogonal to the z-axis has its' co-polarization in the y-axis and its cross-polarization located on the x-axis.

$$\hat{co} = \hat{y} \quad \hat{xp} = \hat{x} \tag{2.4}$$

likewise a horizontally polarized wave (x-polarized)

$$\hat{co} = \hat{x} \quad \hat{xp} = -\hat{y} \tag{2.5}$$

When the wave is circularly polarized the wave rotates around the Z-axis while propagating through space with an equal amplitude in both X and Y axis. Circular polarization does not exist in reality, due to the fact that there is always a slight variation in amplitude of the E-field during circular polarization resulting in elliptical polarization. The elliptical polarization can be either LHCP or RHCP depending on the rotation of the E-field is rotating clockwise (LHCP) or counter-clockwise (RHCP). Figure 2.1 shows both modes of operation while 2.2 illustrates an ideal circularly polarized electromagnetic wave.

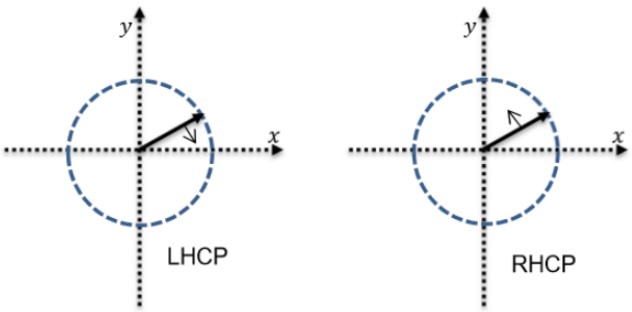

Figure 2.1: Left and Right hand circular polarization

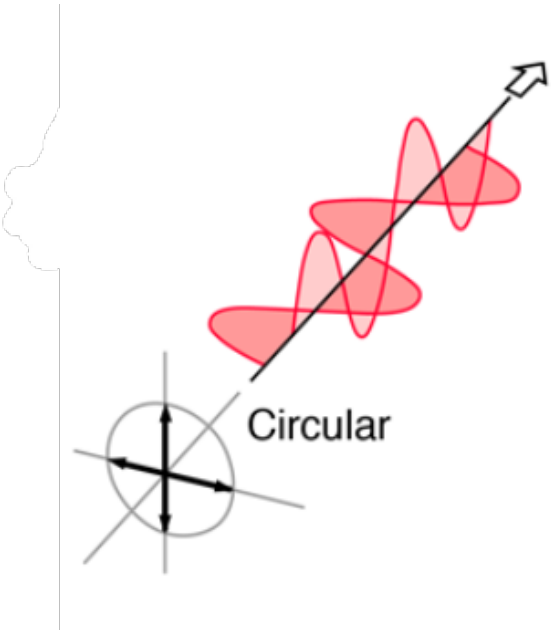

Figure 2.2: Circular polarization characteristics

2.2.2 Axial Ratio

A truly circular polarization can never be attained due to the fact that there will always be a difference in magnitude resulting in a major and semi-major axis, i.e elliptical polarization. Axial ratio is a measurement of the difference between the strongest point of the E-field vector compared to the weakest point of the E-field vector in one revolution, i.e how close to circular polarization the elliptical polarization is.

$$AR_{dB} = 10log_{10}|\frac{E_{max}}{E_{min}}|^2 \tag{2.6}$$

When attaining an axial ratio lower than 3 dB the elliptical polarization is considered to be almost circular, which is a standard specification for most antenna designs using circular polarization. Figure 2.3 shows an exaggerated explanation to this. The AR bandwidth of an antenna is the measurement of all frequency points where the axial ratio of the specified design has a axial ratio below 3 dB, and is most commonly presented in a percentage:

$$BW_{AR}(\%) = \frac{f_u - f_l}{f_c} \tag{2.7}$$

where f_u,f_l corresponds to the upper and lower cutoff frequency, likewise f_c to the center frequency of operation.

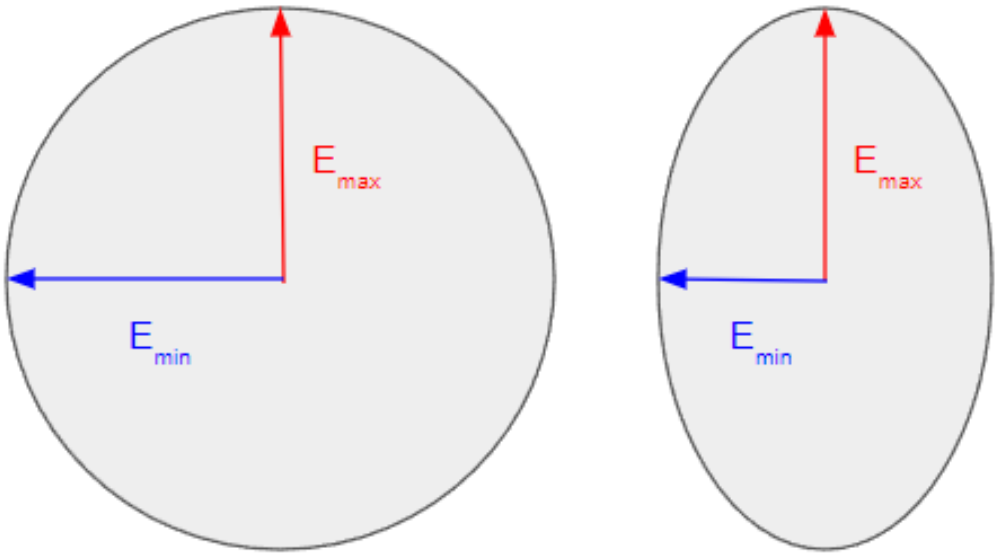

Figure 2.3: Ideal Circular Polarization (Left) Elliptical Polarization (Right).

2.2.3 Bandwidth

The bandwidth is often described in terms of voltage standing wave ratio (VSWR) which is directly correlated to the return loss of the input power, most commonly specified as 20, 15 or 10 dB depending on specification. The bandwdith is then defined as all frequencies having a lower reflection than the specified limit and is commonly defined in percentage:

$$BW(\%) = \frac{f_u - f_l}{f_c} \tag{2.8}$$

There are numerous techniques to modify and ultimately increase the BW which is described more thoroughly in the antenna design section.

2.2.4 Antenna Gain

The gain of the antenna can be defined as the directivity, meaning the amount of the total power that can be directed in a wanted direction, compared to an isotropic antenna where the power is radiated equally in all directions of a sphere.

$$D_0 = 10log_{10}|\frac{G_0^2}{G_{iso}^2}| \tag{2.9}$$

2.3 Low Noise Amplifier

The active section of the antenna is the low noise amplifier stage. This type of amplifier is almost always the first stage of any receiver system where the amplifier

is designed trying to add as little noise as possible, in order to guarantee that the signal can be distinguished from noise meaning that later amplifier stages can have less noise consideration since the Signal-to-Noise ratio (SNR) already being relatively high. Noise is always present in communication systems and is an unwanted signal that is added to the transmitted signal.
This ratio be described as the ratio between the available received signal to the noise power ratio. Satellite communication also posses with different types of noise, not only internal noise from the actual circuitry but also natural noise from atmospheric actions and extraterrestrial noise originating from the sun and outer space. The random motion of electrons in conductors is also the reason for thermal noise to be received by the internal circuitry.
In addition to noise, LNAs possess a set of variables that affect the overall performance of the LNA, see figure 2.4. It is the responsibility of the designer to make careful considerations to these characteristics for optimal selectivity and sensitivity.

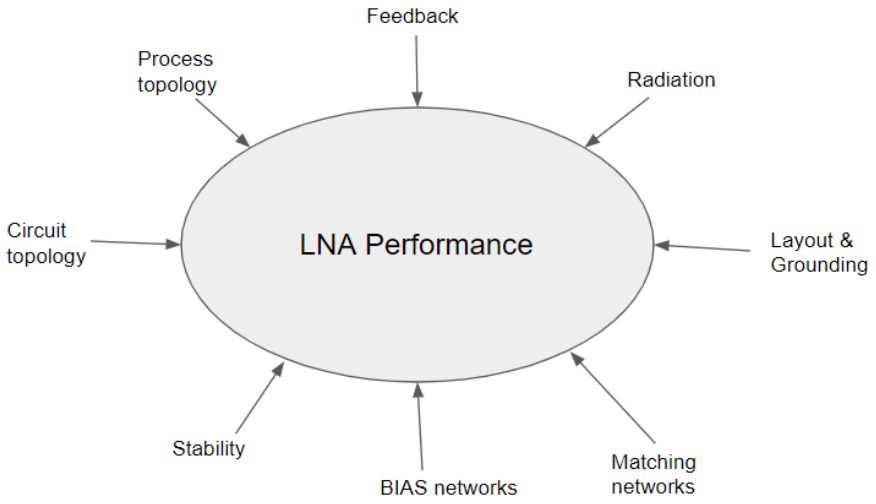

Figure 2.4: LNA Performance variables

2.3.1 Reflection coefficients

Microwave systems often exhibits changes or discontinuities in impedance, at these junctions there will be reflections occurring due to mismatches, and as a result not all the incident power will be delivered to the load but be reflected at this junction. The ratio between the reflected wave versus the incident wave is defined as the reflection coefficient and is commonly expressed in the form below:

$$\Gamma = \frac{Reflectedwave}{Incidentwave} = \frac{Z_L - Z_0}{Z_L + Z_0} \tag{2.10}$$

When the load Z_L has the same impedance as the characteristic impedance Z_0 at all junctions both parameters will cancel out resulting in no reflections, hence all input power will be delivered to the load. The phenomena of reflections is

generally undesirable and even more so in amplifier design because this would further attenuate the already weak signal, it is therefore of great interest to match both the input and output section of the amplifier network to attain as low reflections as possible. Furthermore the reflection coefficient RL provide the basis for return loss which can be seen in table 5.1 that is simply the magnitude of the reflection coefficients.

$$RL = -20log|\Gamma| \tag{2.11}$$

2.3.2 S-Parameters

Scattering parameters or S-parameters [3] is expressed in an S-matrix. It describes the response of the incident and reflected voltage waves at each port, and is commonly used in RF environments where it expresses the complete system behaviour. For a two port network which can be seen in figure 2.5 the characteristics can be defined as four separate S-parameters S_{11} S_{12} S_{21} S_{22} where:

S_{11}: input port voltage reflection coefficient.
S_{12}: Reverse voltage gain.
S_{21}: Forward voltage gain.
S_{22}: Output port voltage reflection.

The wave ratios measurements can be calculated by selectively altering the terminations by the following equations:

$$S_{11} = \frac{b_1}{a_1}|_{a_2=0} \tag{2.12}$$

$$S_{12} = \frac{b_1}{a_2}|_{a_1=0} \tag{2.13}$$

$$S_{21} = \frac{b_2}{a_1}|_{a_2=0} \tag{2.14}$$

$$S_{22} = \frac{b_2}{a_2}|_{a_1=0} \tag{2.15}$$

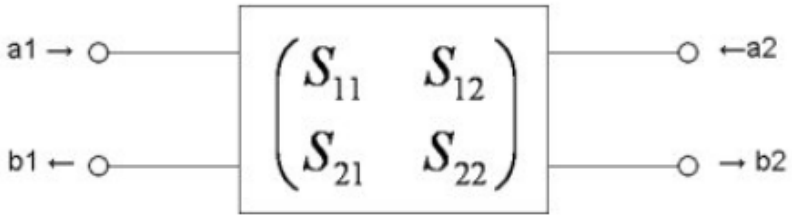

Figure 2.5: Two-port S-Parameter network [2]

2.3.3 Amplifier Gain

The gain of an amplifier circuit is defined as its ability to amplify the magnitude of an incoming signal. In addition, it is widely considered to be one of the most basic and common applications in RF and microwave systems. Thanks to improvements in silicon technology, modern amplifier circuits rely almost exclusively on transistor devices such as BJTs, Si MOSFETS, MESFETS or HEMTS. This also allows amplifier systems to be low cost, achieving high reliability and making them easily integrated [3]. Considering a single-stage transistor with input and output matching that can be seen in figure 2.6. The most useful definition of gain is the transducer gain (G_T), which takes into account the average power delivered to the load versus the maximum available power from the source. This in turn includes both source and load mismatch and will further form the basis for how the gain in the table 5.1 is calculated. As an example, the entire sensor gain can be modeled and calculated using the following equations:

$$G_S = \frac{1 - |\Gamma_S|^2}{|1 - \Gamma_{in}\Gamma_S|^2} \tag{2.16}$$

$$G_0 = |S_{21}|^2 \tag{2.17}$$

$$G_S = \frac{1 - |\Gamma_L|^2}{|1 - S_{22}\Gamma_L|^2} \tag{2.18}$$

Wherethe overall transducer gain is:

$$G_T = G_S G_0 G_L \tag{2.19}$$

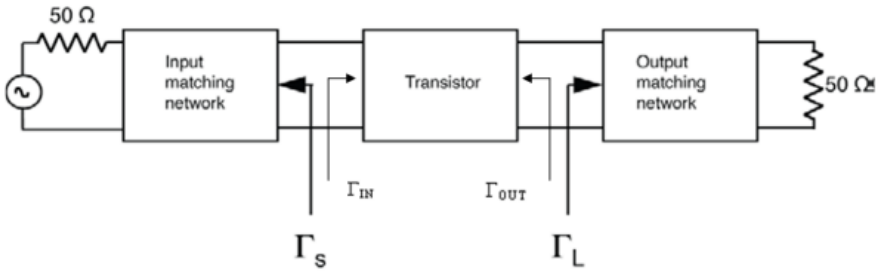

Figure 2.6: General two-port amplifier circuit [3]

2.3.4 Noise Performance

Noise factor (F) is defined as a measure of degradation in the signal-to-noise ratio between the input and output of the component [3]. Noise is more often also described in decibels where its called Noise figure (NF). The total NF can be calculated according to the following equation:

$$NF = \frac{\frac{Signal_{in}}{Noise_{in}}}{\frac{Signal_{out}}{Noise_{out}}} \tag{2.20}$$

This methodology can further be realized by considering a two port network in figure 2.7, which demonstrates the noise and signal power being fed into a two-port network with noisy characteristics. This network considers variables such as Gain (G), Bandwidth (B) and equivalent noise temperature (T_e), therefor one can calculate that the input noise is $Noise_{in} = kT_0B$ where k is the Boltzmann's constant.

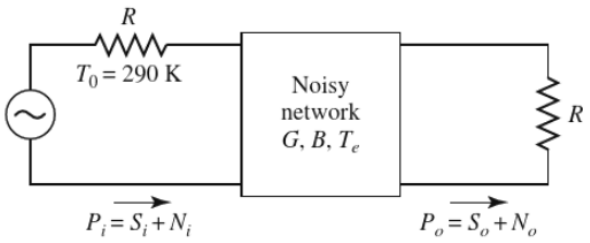

Figure 2.7: Noise figure of two-port network [3]

Then the output noise power can be calculated by taking the sum of the input noise and the internally generated noise, $Noise_{out} = kGB(T_0+T_e)$. Combining the results from before gives the total noise figure by the following equation.

$$NF = \frac{Signal_{in}}{kT_0B}\frac{kGB(T_0 + T_e)}{G * Signal_{in}} \tag{2.21}$$

One can also consider a network with a chain of n-cascaded amplifier circuit, where the total noise figure for this kind of networks can be realised with Friis formula:

$$NF_{tot} = NF_1 + \frac{Nf_2 - 1}{G_1} + \frac{Nf_3 - 1}{G_1 * G_2}....\frac{Nf_n - 1}{G_1 * G_2...G_n} \tag{2.22}$$

When considering a network with cascaded amplifiers, one can clearly see that the noise contribution from the first amplifier stage will add the most noise to the overall system. It is therefor of great interest to achieve the lowest possible noise from this stage and still maintain high gain. This is generally done by trying to match the input of the first amplification stage.

2.3.5 Matching networks

A matching network has its main goal by delivering maximum power while keeping the noise figure low and acceptable gain is achieved. The procedures for achieving an acceptable range for the above parameters are generally seen as difficult. The designer can design the system by first matching for optimal input reflection but must then balance between noise and amplification as these greatly affect each other. Even when designing the matching network, consideration should be given to achieving appropriate stability, bandwidth and small signal gain. Figure 2.6 shows a standard one-step topology for an amplifier with corresponding input and output matching. The matching is usually done by analyzing the S-parameters of the transistor over a set of frequencies at a specific DC bias point. The input and output matching are used to transform the nominal impedance Z_0 of 50Ω to the source

and load impedance of the transistor Z_S and Z_L or the source and load reflection coefficients Γ_S and Γ_L. Again, by referring to figure 2.6, one can see that the maximum power transmission for the input section is the conjugate match to the input impedance:

$$\Gamma_{in} = \Gamma_S^* \tag{2.23}$$

And similarly for the output section:

$$\Gamma_{out} = \Gamma_L^* \tag{2.24}$$

The general case is also that when considering a bilateral transistor i.e when $S_{12} \neq 0$ the sections needs to matched in conjunction to each other.

2.3.6 Stability

Amplifier design including LNA design is based on transistor technology, and one of the most troublesome aspects of amplifier circuits is that they can oscillate when they are not intended, a measure of this is called the stability factor. It is with this measure that one can measure and finally determine whether the system is unconditionally stable, conditionally stable, potentially unstable or unstable. Depending on the project, all of the previously mentioned can be used, but the general design preference for LNA design is to make the circuit unconditionally stable. There are a number of ways to combat instability by either implementing resistors in series or in parallel with the input and output or by capacitor bypassing, one can also use a feedback network or inductive degeneration techniques. The stability can later be verified mathematically by fulfilling the equations below.

$$K > 1 \ \textit{where} \ K = \frac{1 - |S_{11}|^2 - |S_{22}|^2 + |\Delta|^2}{2|S_{12}S_{21}|} \tag{2.25}$$

and

$$|\Delta| < 1 \qquad \textit{where} \quad \Delta = S_{11}S_{22} - S_{12}S_{21} \tag{2.26}$$

or

$$\mu > 1 \qquad \textit{where} \qquad \mu = \frac{1 - |S_1 1|^2}{|S_{22} - S_{11}^*\Delta| + |S_{21}S_{12}|} \tag{2.27}$$

A physical realisation for unwanted oscillation can be consider with a BJT transistor in figure 2.8, here the stability factor can be defined as the rate at which the collector current changes as suppose to when the base to emitter voltage changes. Or as the ratio of change in collector current to change in base current.

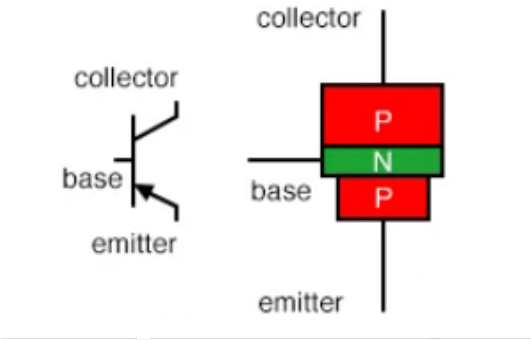

Figure 2.8: BJT, PNP transistor

2.3.7 Stability Circles

It is also common practice to show the stable regions in smith charts, this is performed by plotting the input and output stability circles in the Γ_S and Γ_L plane. While also considering the input and output reflection coefficients, where the conditions for unconditional stability follows [3]:

$$\Gamma_L < 1 \tag{2.28}$$

$$\Gamma_S < 1 \tag{2.29}$$

$$|\Gamma_{in}| = |S_{11} + \frac{S_{12}S_{21}\Gamma_L}{1 - S_{22}\Gamma_L}| < 1 \tag{2.30}$$

$$|\Gamma_{out}| = |S_{22} + \frac{S_{12}S_{21}\Gamma_S}{1 - S_{11}\Gamma_S}| < 1 \tag{2.31}$$

It is then clearly visible that the input and output reflection is dependent on the source and load terminations. Whereas the boundary between the unstable and stable region can be modelled by plotting all values of Γ_S and Γ_L as a circle. The position C and radius r for the load circle is then calculated as [3]:

$$C_L = \frac{(S_{22} - \Delta S_{11}^*)^*}{|S_{22}|^2 - |\Delta|^2} \tag{2.32}$$

$$R_L = |\frac{S_{21}S_{12}}{|S_{22}|^2 - |\Delta|^2}| \tag{2.33}$$

Similarly for the source stability circle

$$C_S = \frac{(S_{11} - \Delta S_{22}^*)^*}{|S_{11}|^2 - |\Delta|^2} \tag{2.34}$$

$$R_S = |\frac{S_{21}S_{12}}{|S_{11}|^2 - |\Delta|^2}| \tag{2.35}$$

The boundary between whether a circuit is stable or unstable can be seen at the input $|\Gamma_{in}| = 1$ circle. And thus be seen that the boundary outside this circle is counted as the stable region and the one inside is unstable. And ultimately the system can be regarded as unconditionally stable if the stability circle is completely outside the $|\Gamma_{in}| = 1$

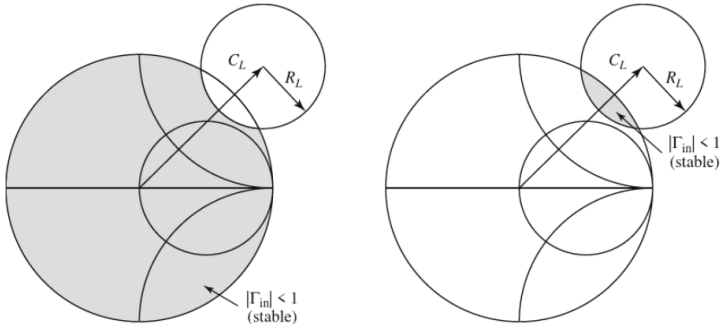

Figure 2.9: Model of output stability circles, grey shade depicts the stable region and demonstrates a conditionally stable system [3]

2.4 High Frequency Structure Simulator

Ansys High Frequency Structure Simulator or HFSS is a tool used to do full EM wave simulations in 3D. The evaluation of complex structures where calculation by hand cannot be performed which is common in antenna design makes this software a very valuable tool for this design [17]. Therefore has this software been used throughout the design process.

2.5 Advanced design system

Advanced design system or (ADS) is an electronics circuit design software mostly used for RF and microwave applications. ADS makes it easy to evaluate performance of proposed circuit designs and further capabilities of layout and layout verification where Momentum EM wave simulations is possible. For this project, ADS has been used to design and simulate the LNA and feed network, further EM wave simulations has been performed for the LNA circuitry for layout verification.

2.6 Vector Network Analyzer

A vector network analyzer or (VNA) is a vital utility for rf designers, in short terms, a VNA is a test equipment that measures the response of a proposed network as a vector of real and imaginary parts to characterise its' performance. It works on the basis of reflected and transmitted waves through and from a circuit for a frequency band of interest. The VNA enables the designer to via a component with two ports

measure it's corresponding parameters and ultimately characterise the device [18]. The VNA has for this project been used to validate antenna impedance bandwidth and to determine the LNA performance and characteristics.

2.7 Anechoic chamber

The evaluation of an antenna could first and foremost be determined by connecting it to a VNA and measure its impedance bandwidth. This gives a good understanding which describes the range of frequencies an antenna can radiate and/or receive energy. But for a deeper understanding of how the antenna actually performs, it is imperative to test the actual performance to determine its specifications. Testing an antenna in an anechoic chamber is one of those ways. The name anechoic means ("non-echoing, echo-free"), its room is shielded for which it is designed to prevent unwanted signals to permeate the room. All of the walls is covered with a highly conductive layer to block unwanted signals entering the room from outside. Above this layer is an absorbent material shaped like a cone to minimize reflections coming from the DUT from any directions [4], see figure 2.10 for material visualization and figure 2.11 for chamber configuration. By doing tests in an anechoic chamber enables the designer to measure antenna efficiency, radiation pattern and gain among others. The anechoic chamber has been used to validate the performance of the antenna both with and without and LNA for determining all of the latter.

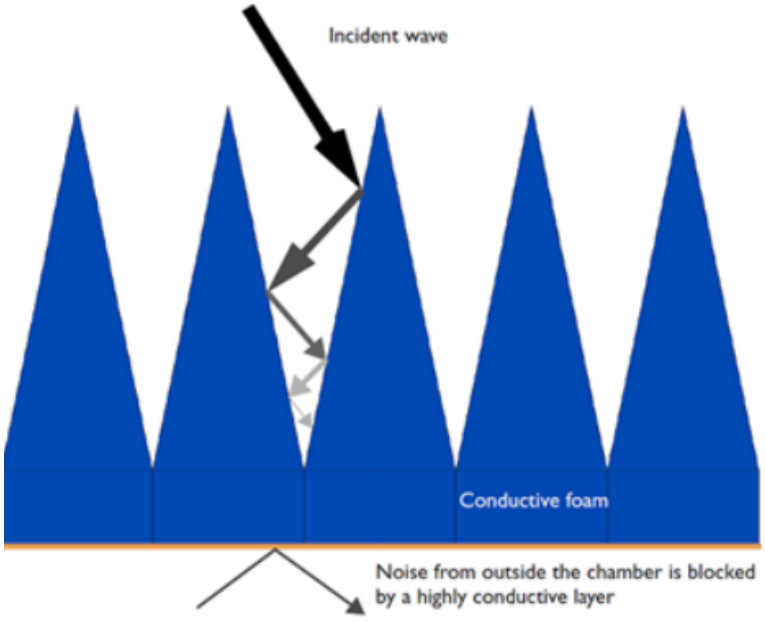

Figure 2.10: Absorbent material covering the inside of the Anechoic chamber, conductive shielding layer below the material [4]

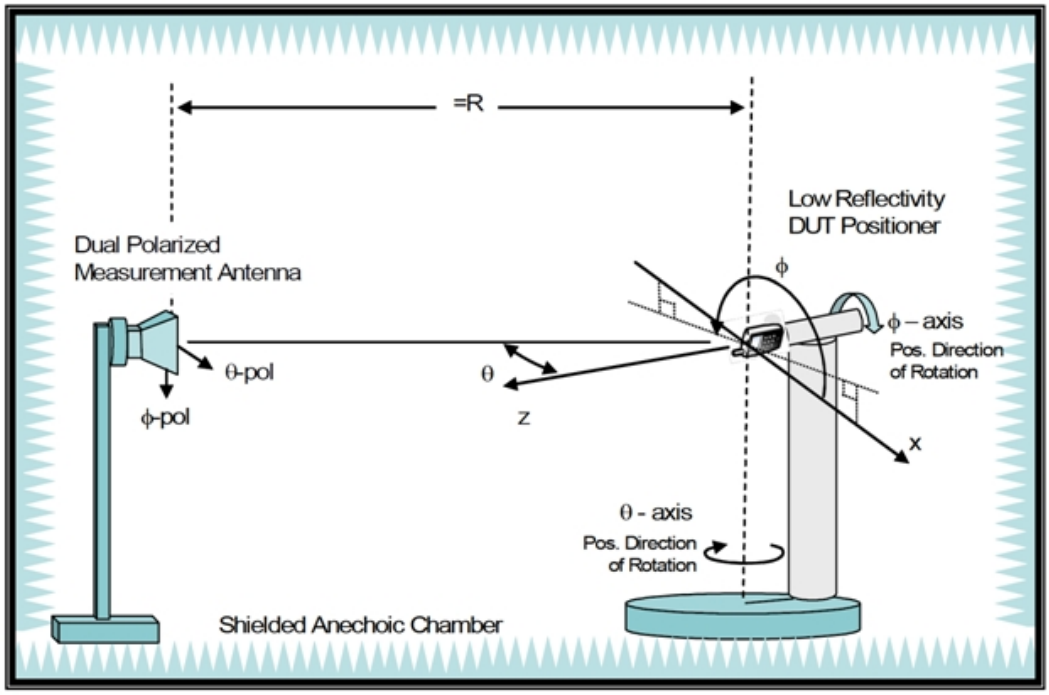

Figure 2.11: Chamber layout and configuration, [5]

3
Antenna Design

This chapter contains earlier work of both dual-band and wideband designs. It also incorporates simulations of the final design to demonstrate how varying particular parameters achievs a different response of VSWR and axial ratio.

3.1 Antenna Specifications

As part of Beyond gravity's continuous product development it is of interest to widen the product range of cost effective, size dependent and a deeper integration with the passive and active elements between the antenna and receiver system. With this in mind the following specifications in table 3.1 is set as the benchmark for this project.

Table 3.1: Project specific specifications

Size	<100x100mm
Axial Ratio	<3dB
Return Loss	<-10dB
Gain, boresight	> 3dB
Gain, $\theta = 65$	>0dB
Gain, $\theta = 80$	>-5dB

3.2 Circular Polarization

Realization of a CP antenna can be obtained from a vast array of strategies. The easiest is to feed different points of the antenna with phase shifted variations of an original signal. Feeding the antenna at four separate symmetrical locations with 0, 90, 180 and 270 degree phase shifted signals possessing equal amplitudes. The same effect can also be realized by feeding the antenna at three separate points with a phase shift of 120 degrees relative to one another. Both these methodologies will realize an approximately ideal circular polarization albeit slightly elliptical. Another method is to make use of truncated corners, effectively cutting of two of the corners at the patch. By utilizing a single feed at the correct position two orthogonal modes [9] will be excited with a 90 degree phase shift relative to one another.

3.3 Patch antenna

To create an antenna while minimizing the overall volume the patch antenna is best suited for this purpose. The design of the antenna is initiated according to the transmission line model, see equations 3.4-3.7. The patch width and length are calculated to ensure that the antenna achieves resonance at the intended frequency. Following the methodology from chapter 14 in [19], calculating the width, length and height of the antenna for a substrate with a specific dielectic constant (ϵ_r), in order to give a first view into what the dimensions of the specified patch will be, which in later stages needs to be optimized in HFSS via simulations.

Firstly: the height, dielectric constant of the substrate (ϵ_r) and resonanting frequency is specified by the user. The first attempted design consisted of the following specifications: a patch with a resonant frequency in the lower GNSS band with a center frequency of 1187 MHz on a single layered FR4 substrate with an (ϵ_r) of 4.6, and a height of 1.6 mm.

$$W = \frac{1}{2f_r\sqrt{\mu_0\epsilon_0}} * \sqrt{\frac{2}{\epsilon_r + 1}} = \frac{c_0}{2f_r} * \sqrt{\frac{2}{\epsilon_r + 1}} \tag{3.1}$$

$$W = \frac{c_0}{2f_r} * \sqrt{\frac{2}{\epsilon_r + 1}} \tag{3.2}$$

$$Q = \frac{f_c}{f_2 - f_1} \tag{3.3}$$

Since the antenna does not have infinite length and width, fringing effects will be apparent which is taken into consideration via equation 3.6. There it is implemented by calculating the effective dielectric constant (ϵ_{eff}) and thereafter shortening the width and length by a fraction of the initial one. This is done because the physical patch will appear wider electrically due to the nature of the fringing effects at the edges of the patch.

$$W = \frac{1}{2f_r\sqrt{\mu_0\epsilon_0}} * \sqrt{\frac{2}{\epsilon_r + 1}} = \frac{c_0}{2f_r} * \sqrt{\frac{2}{\epsilon_r + 1}} \tag{3.4}$$

$$\epsilon_{eff} = \frac{\epsilon_r + 1}{2} + \frac{\epsilon_r - 1}{2}[1 + 12\frac{h}{W}]^{-\frac{1}{2}} \tag{3.5}$$

$$\Delta L = 0.412h\frac{(\epsilon_{eff} + 0.3)(\frac{W}{h} + 0.264)}{(\epsilon_{eff} - 0.258)(\frac{W}{h} + 0.8)} \tag{3.6}$$

$$L = L_{eff} - 2\Delta L = \frac{c_0}{2f_r\sqrt{\epsilon_{eff}}} - 2\Delta L \approx (0.47 - 0.49)\lambda_d \tag{3.7}$$

A rough estimate of the width and length of the ground plane is given in [20] where the minimum requirement for the size is six times the height plus the initial width/length of the antenna patch.

$$W_g = W + 6h \qquad\qquad L_g = L + 6h \tag{3.8}$$

The transmission line model for modelling the rectangular patch antenna above can be used in similar fashion to create a square patch. The antenna will have a somewhat similar resonating frequency, although some tuning is of need.
The major issue creating a single fed patch or stacked patches is the nature of the bandwidth being relatively narrow due to the high Q value of a microstrip patch. Since a wideband behaviour is sought after when trying to implement an antenna for GNSS technologies further investigation of different topologies is required.

There are multiple methods in order to create a dual or wide-band antenna for the higher and lower GNSS bands, and can mainly be differentiated into separate categories which is presented in the next chapter. The first is to make use of a multi-feed network, while other methods are
The first is to use stacked patches with a multi-feed design, or to use a single patch with some geometric oddity or unique feeding method in order to improve the impedance and axial ratio bandwidth. Different methods are presented in 3.4.

3.4 Earlier work

As mentioned earlier, one method to create dual-band antennas is to implement a stacked layout where each patch resonates on a set frequency due to the dimensions of the patch. In [6] this method is used combined with truncation of the corners on each patch in order to create a circularly polarized antenna with a single feed network.

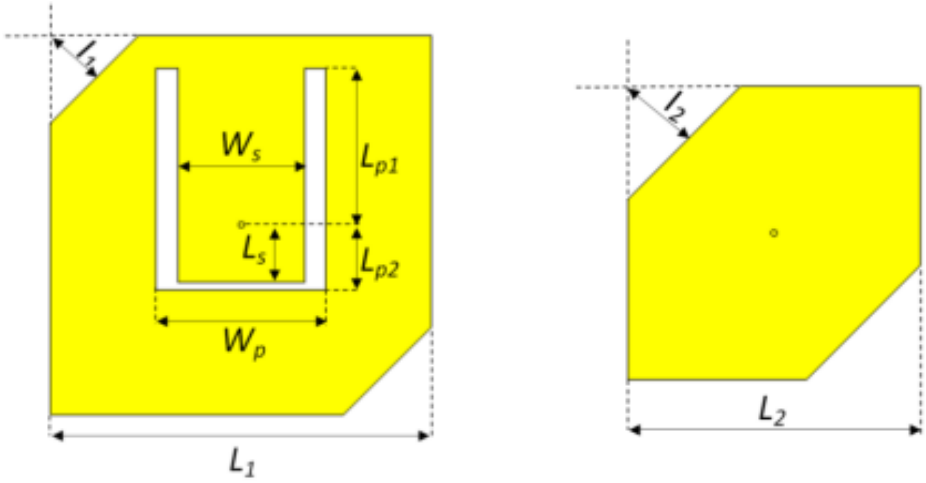

Figure 3.1: Driven main patch (left) and parasitic patch (right) from [6]

Although the impedance bandwidth (the bandwidth where the return loss is lower than -10 dB) is a suitable one, the main issue with this type of antenna making use of truncated corners is the low AR bandwidth, (the bandwidth where the axial ratio is below 3 dB). Ideally for a dual band design our specifications require that we have atleast 50 MHz of bandwidth for both the L1 and L5 band respectively, see figure 1.1, for both the impedance and axial ratio bandwidth.

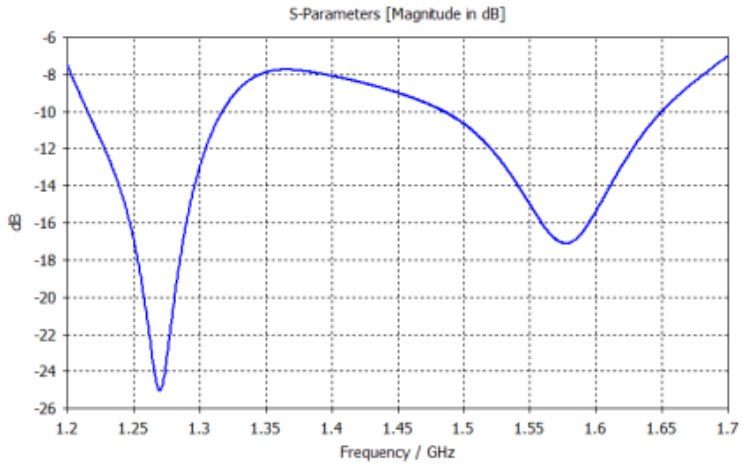

Figure 3.2: Return loss (S_{11}) of proposed design, from [6]

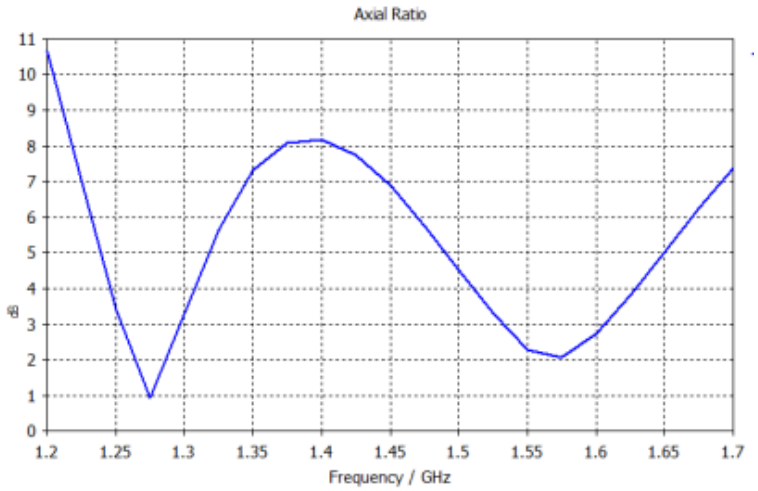

Figure 3.3: Axial Ratio of proposed design, from [6]

3.4.1 Capacitively coupled Dual probe stacked patch

In [7] the engineers make use of stacked patches where the length of each patch is half of the guided wavelength while also using capacitive coupling as the feeding mechanism, see figure 3.4. The capacitively coupled patches introduce a conductivity which counteracts the induced inductance due to long probe lines.

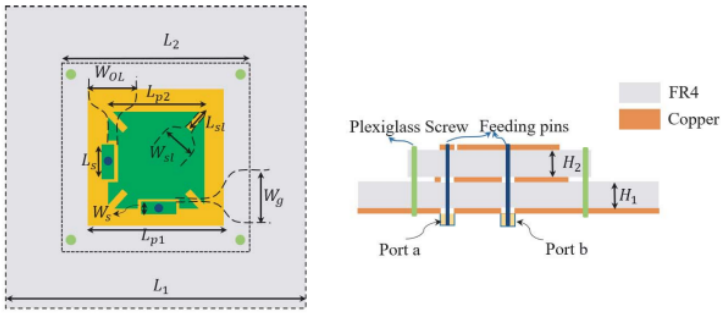

Figure 3.4: Layout of antenna, top view (left), side view (right) from [7]

A wide-band dual-band return loss for L1 and L5 bands are attempted in this report, but the return loss of -10 dB is not achieved for the entire E5 band (E5a) seemingly as the cutoff is above 1189 MHz, see figure 3.5, which is mentioned in the conclusion of the report.

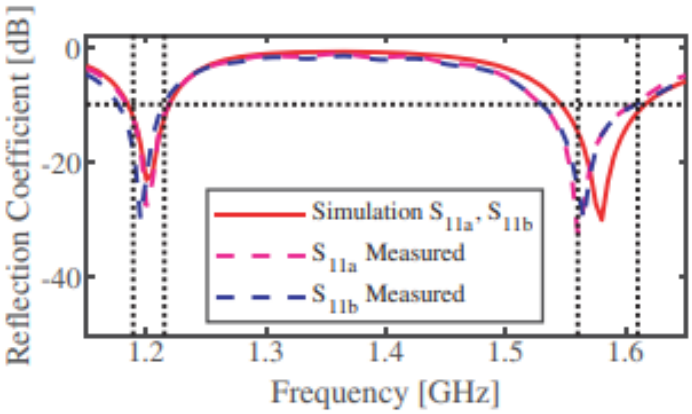

Figure 3.5: Return loss simulated and measured, from [7]

3.4.2 Dual/Quad-feed Circular patch

A wide-band multi-feed antenna is reported in [8] attaining both a wide impedance and AR bandwidth. The design is based on L-type probes used to capacitively feed the antenna which is a major stepping stone to increase the impedance bandwidth of designs regarding patch antennas, whereas patch antennas fed directly via for example a coaxial connector tend to have a lower bandwidth.

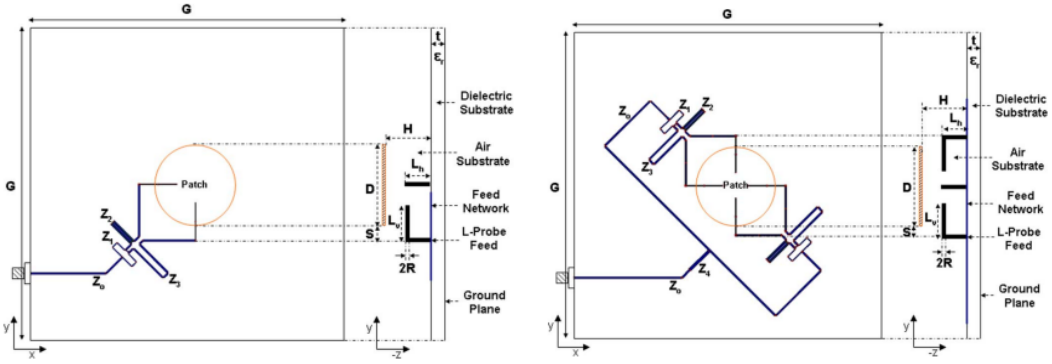

Figure 3.6: Layout of dual-fed patch (left) and quad-fed patch (right), from [8]

The engineers designing this antenna makes clever use of a new "balun" design in which a portion of the ground plane below the coupled lines in the novel Schiffman phase shifter is cutout to further improve the bandwidth of the power distributed to the output ports (P2 and P3), see figure 3.7.

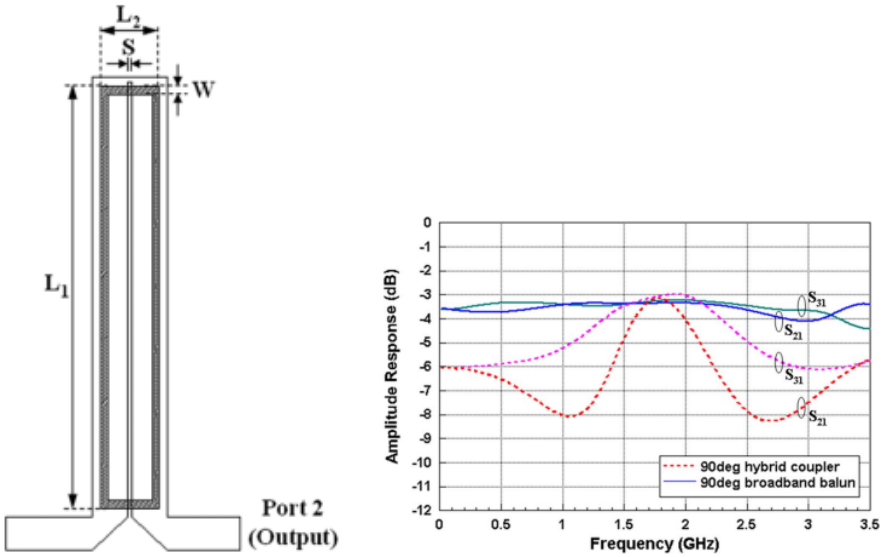

Figure 3.7: C-section with groundplane cutout in gray (left) and the amplitude response to port 2 and 3 (right), from [8]

3.5 Attempted designs

The continuous workflow creating this antenna has been evolving gradually from different designs to others while taking new inspiration from articles meanwhile. The first design consisted of creating two separate patches with dimensions according to the specified resonant frequencies of the L1 and L5 band respectively, see 1.1. Inspired by [9] an attempt was made to create two separate patches with truncated corners on each patch and a single coaxial feed at a precise point in order to induce RHCP. All the designs have been simulated and optimized mainly via parametric analysis in HFSS, see section 2.4.

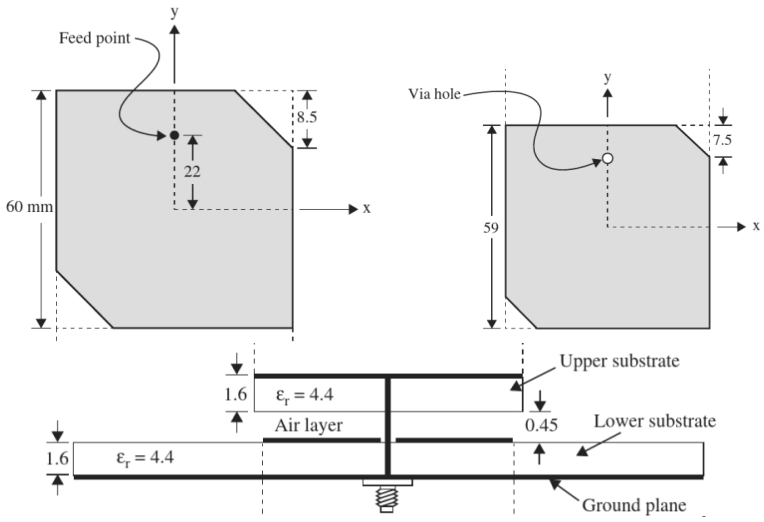

Figure 3.8: Dual-band CP truncated corners patch antenna, Bottom patch (top right), Top patch (Top left), Sideview (Bottom), from [9]

As can be seen in figure 3.9, the return loss for the L5 band of the antenna referenced in [9] the lower cutoff frequency for the L5 band (1195 MHz) could be modified and shifted by 35 MHz in order to satisfy the condition for a return loss lower than 10 dB over the entire band.

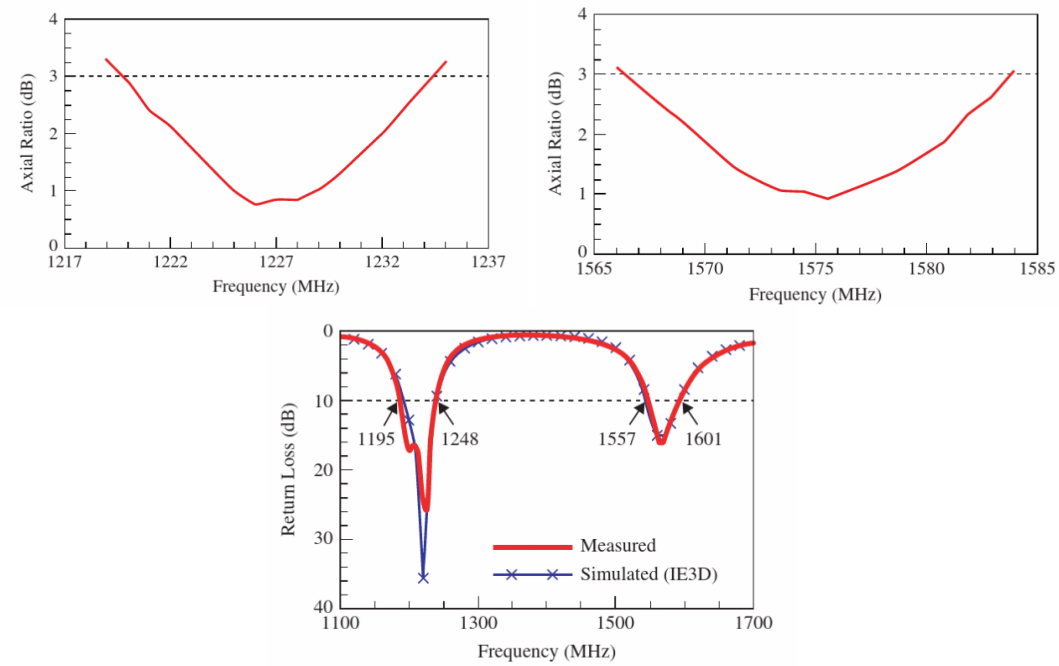

Figure 3.9: Axial Ratio L5 (Top left), Axial Ratio L1 (Top right), Return Loss L1+L5 (Bottom), from [9]

Two major issues were established while working with a similar design in HFSS. Firstly, the band was slightly too narrow for the L5 band. During simulations and

optimizations in HFSS a return loss below 10 dB could not be established in the entire L5 band while staying inside the specified dimensions, either the lower of upper cutoff frequency did not fall within the specifications. Secondly, the AR bandwidth was too narrow for both the L1 and L5 band.

Ideally a single feed CP patch antenna is favored due to the fabrication being less complex, but creating a wide impedance and AR bandwidth for a single feed design is a hard task [9]. This is due to the the fact that the single feed patch antenna has a high Q value, and since the Q value is inversely proportional to both the AR and Impedance bandwidth according to equations 3.9 and 3.10.

$$ARBW = \frac{AR - 1}{\sqrt{AR}Q} \tag{3.9}$$

$$RLBW = \frac{\sqrt{2(VSWR - 1)}}{Q} \tag{3.10}$$

Equation 3.9 and 3.10 can be found in [21].
The Q-factor of the antenna can be decreased [21] by changing the proper material effectively choosing the dielectric constant for the guided wave or by inserting an air-gap between patches. However, by inserting large gaps into the design long probes or transmission lines from the feed point to the antenna will introduce a large inductance due to the increased length of the installed lines.

There are multiple methods to counteract the inductance caused by the long probes, one of which is to make use of L-shaped feeding probes, a corrugated ground plane or an L-shaped patch. In the case of the L-shaped feeding probe, a conductance is introduced due to the electromagnetic coupling [9] between the probe and the antenna patch which counteracts the inductance caused by the long probe itself resulting in less overall impact.

3.5.1 Capacitively fed stacked patch

The work in [7] has a wide bandwidth in the L1 band, but when recreating the design in HFSS, the bandwidth was too low (40 MHz) to cover the L5 band for GPS, Galileo and Glonass. Multiple simulations were performed with the goal to enhance the bandwidth for the lower band; Inserting an airgap between layers, introducing corner-cuts in the lower patch similar to the one in the upper patch and increasing the height of both dielectrics.

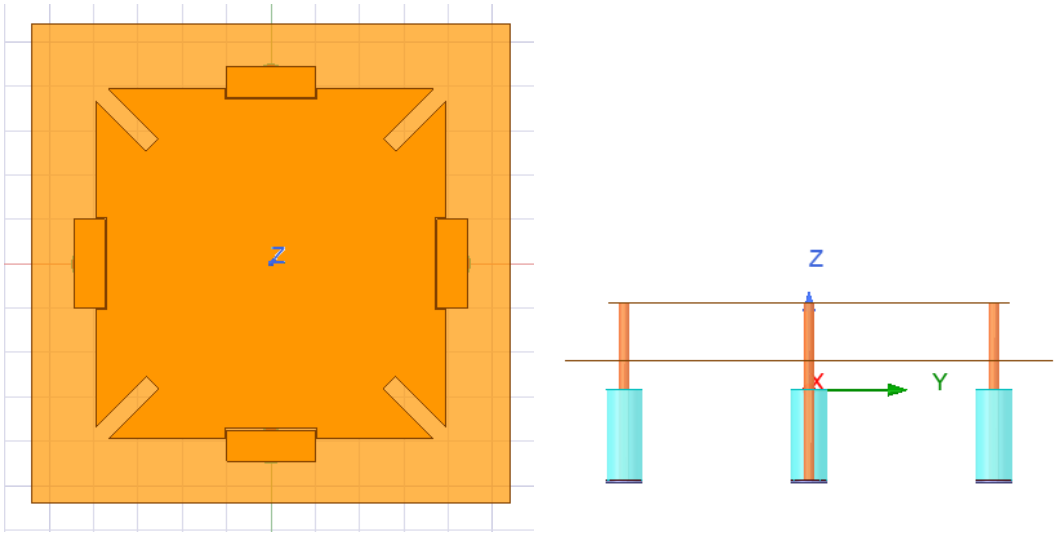

Figure 3.10: Attempted antenna design, topview (left), sideview (right)

An attempt was made to design both a capacitively dual-fed and a quad-fed fed stacked patch antenna similar to the work done in [7], mainly to ensure a wide AR bandwidth in boresight when using a quad feed network. The meet the specifications in 3.1. There were multiple attempts to increase the bandwidth of the L1 and L5 impedance bandwidth but after multiple iterations of simulating and optimizing essentially every parameter the decision was made to not use the design due to it not reaching the goals of "$S_{11} - S13 < -10dB$" bandwidth of 70 MHz in both bands.

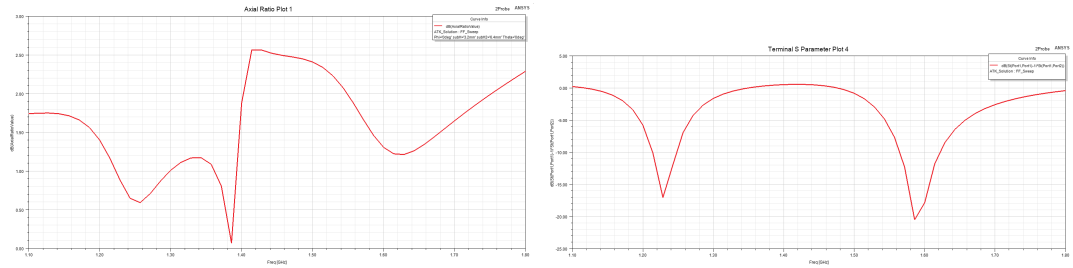

Figure 3.11: Dual fed antenna, Axial Ratio (left), $S_{11} - jS_{12}$ (right)

Only 50 MHz bandwidth is needed for GNSS applications in the L1 and L5 band for communications with GPS, Galileo, Glonass and Beidou but as a safety net we set the minimum requirements for simulations to be 70 MHz in total, having 10 MHz above and below the intended bandwidth to make room for errors caused due to miscalculations or manufacturing processes.

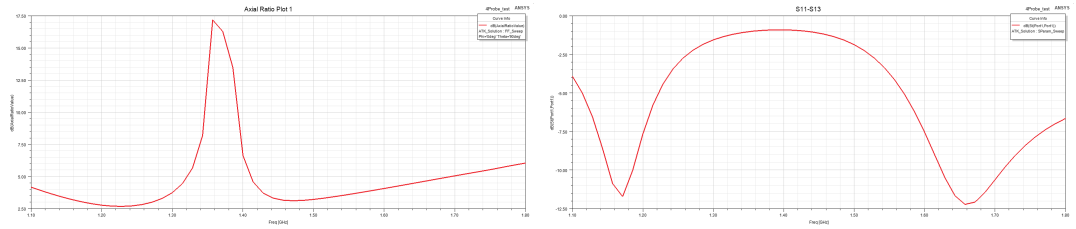

Figure 3.12: Quad fed antenna, Axial Ratio (left), $S_{11} - S_{13}$ (right)

The first attempt to recreate the quad fed antenna was made using the same dimension for the positions of the probes of each feeding points equal to the dual feed version. As can be seen in 3.12 the Axial ratio of the quad feed design has not improved compared to the dual feed design.

3.6 Final design

Keeping all earlier parameters in mind, the finalized design consists of a quad-fed design where each feeding point is fed with an equal input signal 90 degrees out of phase relative to one another. The multi-feed design has a clear advantage in broader AR bandwidth due to the case that a low AR for boresight is guaranteed if the feed network has a stable phase shift in the intended frequency band.

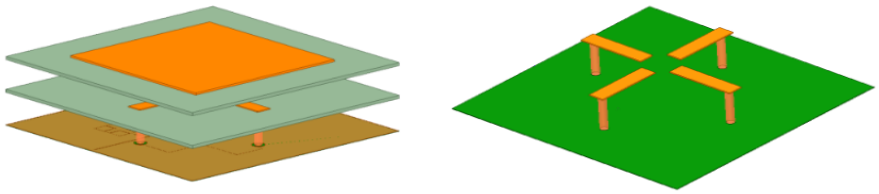

Figure 3.13: Final design with full layout (left), middle layer with L-shaped probes (right).

The design is inspired by the earlier work of [8] consisting of a single capacitively coupled patch with a medium complex feeding network. First, the antenna was simulated to ensure the active impedance matching for a quad-fed networks i.e $S_{11} - S_{13}$ is below 10 dB in the frequency of operation, where each output port of the antenna was connected to a 50 coaxial-line.

The frequency of operation was set to be near the middle of the frequency band (1.38 GHz) thereafter the transmission line model was utilized in order to calculate the approximate width of the antenna to operate at the correct frequency, see equations **??**-3.8 in section 3.3. Secondly, in order to realize a wide impedance bandwidth most parameters was optimized via simulations with the goal to widen the bandwidth in order for operations to be viable in the entire GNSS band, (1164-1610 MHz).

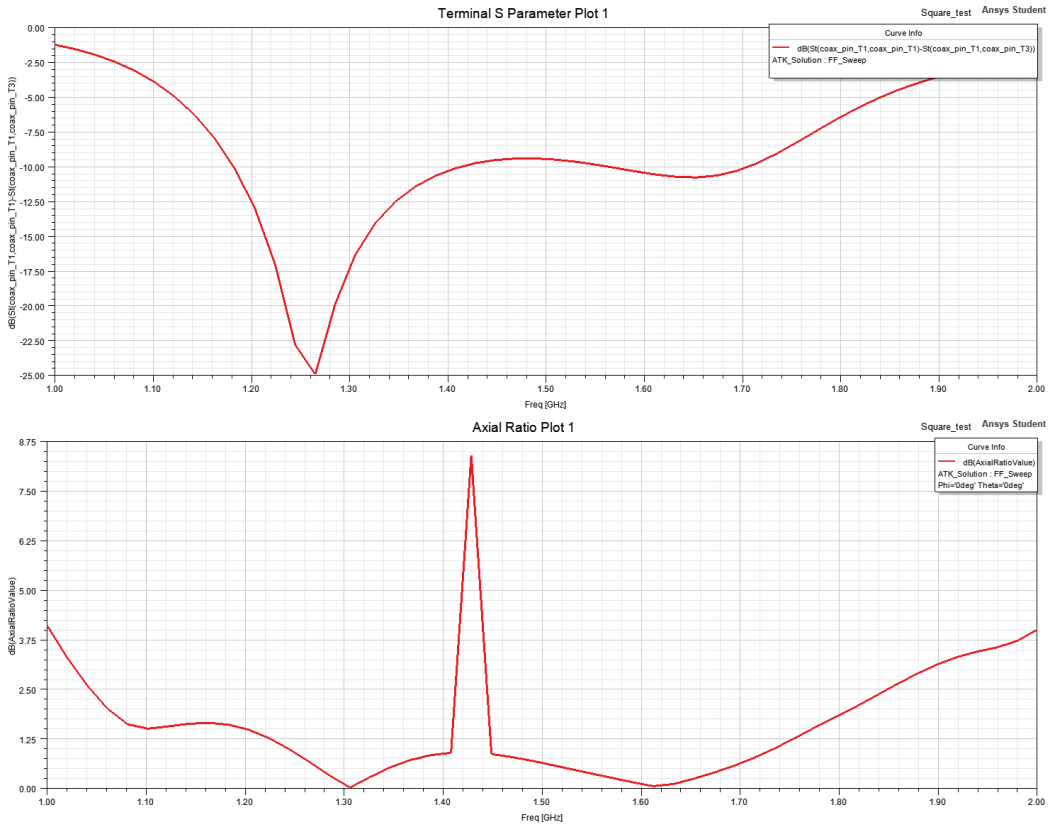

Figure 3.14: Final design, $S_{11} - S13$ (left) AR (right)

This decision was made after the realization that in the near future there will be a need for an antenna covering the entire GNSS band for building applications in need of acquiring pinpoint accuracy of location on centimeter or millimeter level using satellites. A technology that has a need for multiple frequencies in order to cancel out ionospheric and tropospheric effects.

As a challenge this was attempted instead of the earlier work that has the sole focus of acquiring an impedance bandwidth for one or dual-band designs. Compared to the single feed design, small changes to the exact position of the probes did not influence the bandwidth characteristic as long as they acquire a symmetrical position, which can be seen in figure 3.15, where the feeding point of each probe is changed on all 4 points.

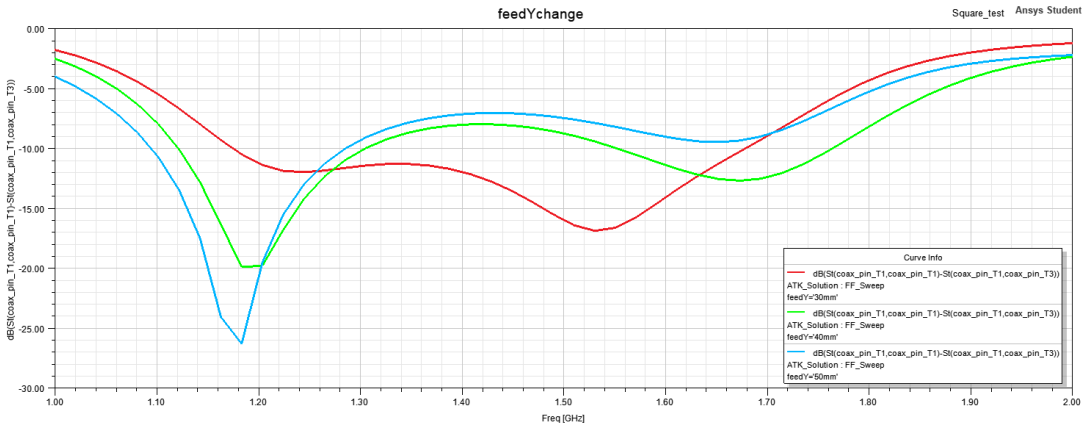

Figure 3.15: $S_{11} - S_{13}$ response when changing the feed points, note that all four probes are moved symmetrically.

The spacing between each substrate, i.e the air portion between each substrate was optimized after rough simulations to approximately 15 mm. The optimum spacing is attained from finer simulations and can be seen in figure 3.16. The widest bandwidth with a level below -10 dB is accomplished by having a 15 mm spacing.

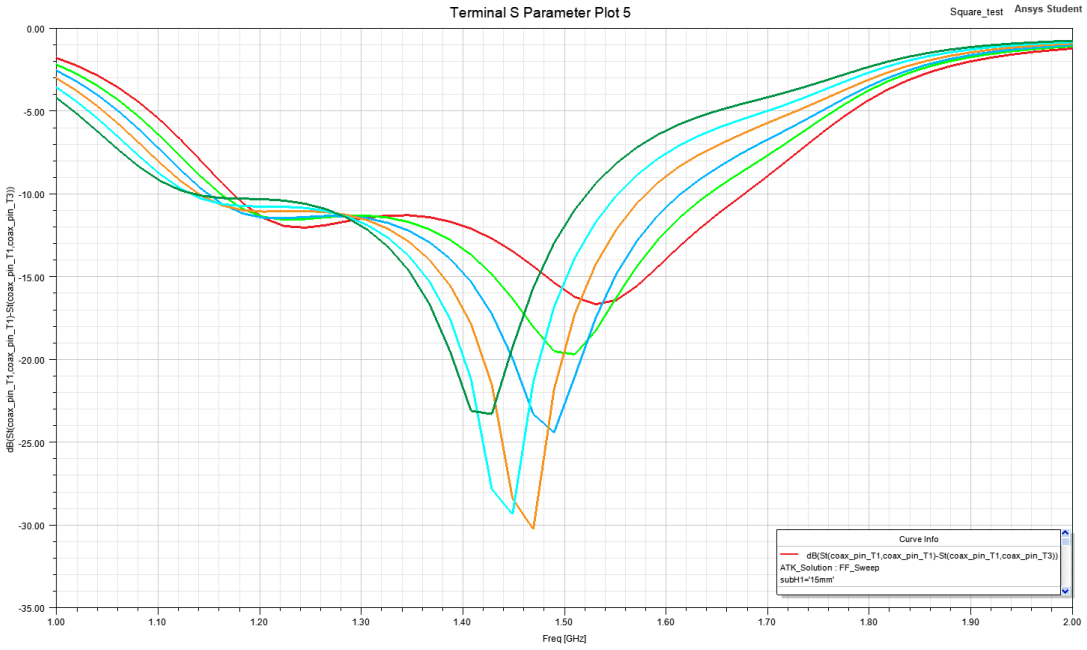

Figure 3.16: $S_{11} - S13$ response with different spacing between substrates (15 to 20 mm), where the red line equals a spacing of 15mm, and the dark green corresponds to a spacing of 20mm.

The same characteristic is obtained for +/- 1 mm, where the entire GNSS band will have a power reflection of -10 dB or lower, see figure 3.17.

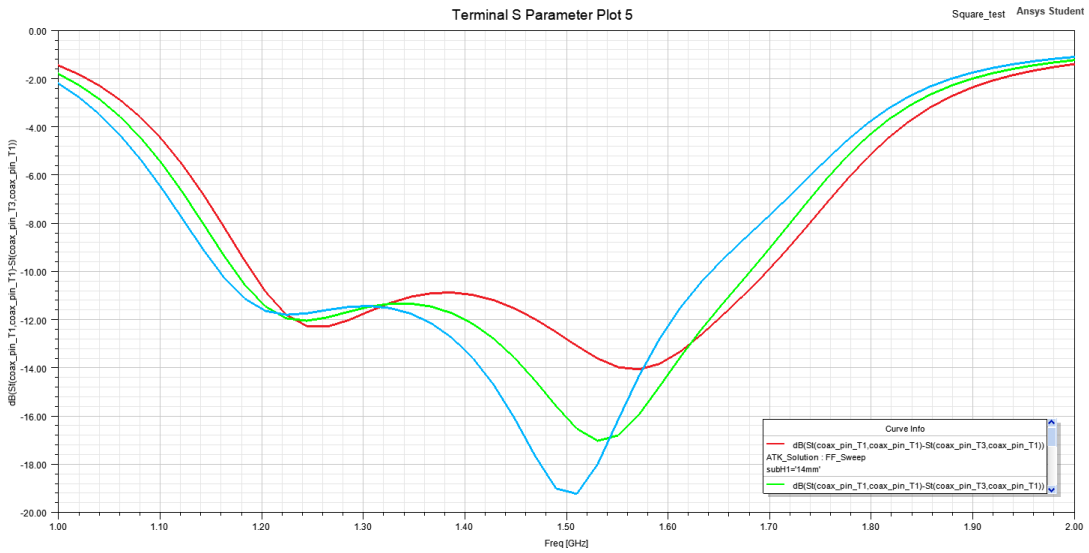

Figure 3.17: $S_{11} - S13$ response with different spacing between substrates (14 to 16 mm), red: 14mm, green: 15mm, blue: 16mm.

While varying both the length of the horizontal section of the L-shaped probe and the length of the antenna patch (see figure 3.18 to 3.19) there was no significant difference to the overall characteristic of the return loss meaning that any small manufacturing mistakes could be overlooked since it would not effect the overall performance to any great extent.

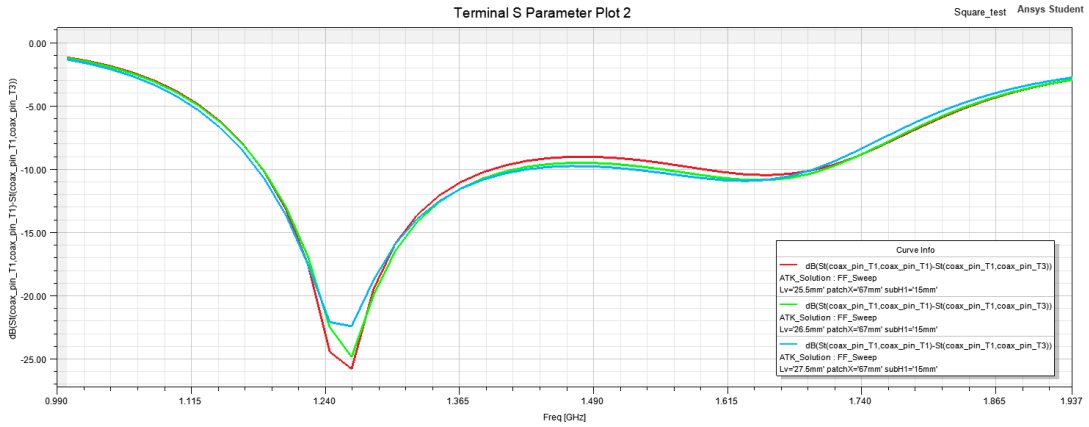

Figure 3.18: $S_{11} - S13$ response with varying lengths of the L-probe patches. L_{probe}=25.5, 26.5, 27.5 mm.

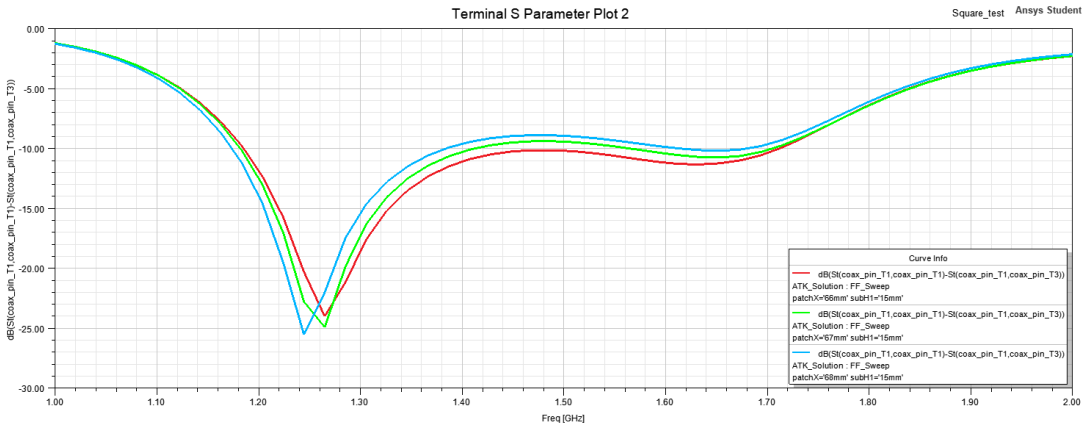

Figure 3.19: $S_{11} - S13$ response varying the patch size of the antenna (W=L=66,67,68 mm).

4
Feed Network

The feeding for the antenna can be realized in a wide variety of ways, but since the simulations of the four-feed network had the widest AR bandwidth this method of feeding was implemented. In order to realize this form of network a wide axial ratio bandwidth and power division bandwidth is sought after. In an ideal measurement the phase shift is 90 degrees between each feeding pin for the entire bandwidth while simultaneously having an equal 6dB power division to each pin, a task that proved relatively hard to accumulate in reality.

After researching and calculating an estimate of the size for the complete feeding network it was decided that the feeding network should consist of a rat race coupler in order to have a broadband phase shift of 180 degrees between two output transmission lines followed by a wilkinson power divider and a schiffmann phase shifter on each of the two output branches, thereby creating a broadband phase shift of 90 degrees between each pin while simultaneously acquiring moderately stable power division over the GNSS bandwidth.

4.1 Wilkinson Power divider

The wilkinson power divider is a crucial component in microwave engineering that has the ability to divide an input signal into two (equal or unequal) output signals. The divider is modeled according to the equal 3dB split in this case, but can also be modeled [3] to have an unequal division according to $K^2 = \frac{P_3}{P_2}$, where P2 and P3 is the power leve on output ports 2 and 3 respectively.

$$Z_{03} = Z_0\sqrt{\frac{1+K^2}{K^3}} \tag{4.1a}$$

$$Z_{02} = Z_0\sqrt{K(1+K^2)} \tag{4.1b}$$

$$R = Z_0(K + \frac{1}{K}) \tag{4.1c}$$

As can be seen in 4.1 when K is set to 1, both tranmission lines Z_{02} and Z_{03} is equal to $\sqrt{2}Z_0$ and the parallel resistor between the tranmission line equals $2Z_0$. In a 50Ω system both tranmission lines is hence 70.7Ω while the parallel resistor is 100Ω. From microstrip theory the width of a tranmission line directly corresponds to the impedance of the tranmission line, as for the final design the width and length of the constructed divider can be seen in the table below.

Table 4.1: Matching network components

W(50)	0.426 mm
W(70.7)	0.24 mm
$l_{\frac{\lambda}{4}}$	x mm

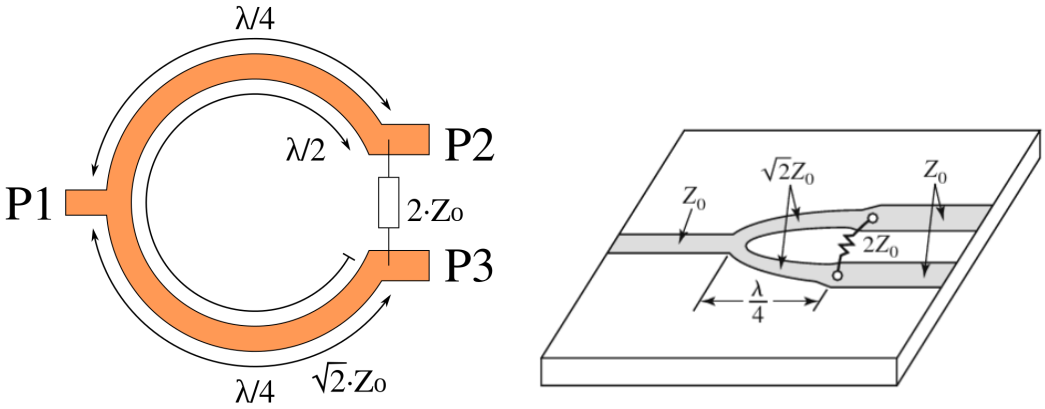

Figure 4.1: Wilkinson Power Divider, from [10] (left) from [3] (right).

Having a maximum size requirement of 100x100mm all components in the feeding network needs to be minimized in order to utilize the space in the best possible way by reducing the area of each component as much as possible. To minimize the design the wilkinson power divider lines are compressed as can be seen in figure 4.2 with a minimum length between each transmission line of atleast $3Z_0$ to ensure that no coupling between the curled tranmission lines is present in the design, (a standard spacing advised by supervisors at RUAG).

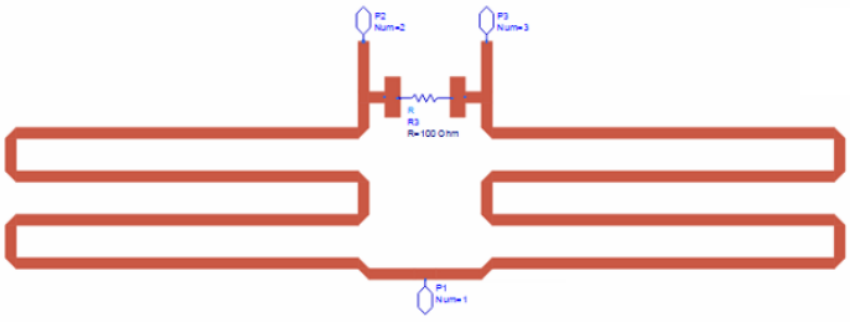

Figure 4.2: Compressed Wilkinson Divider

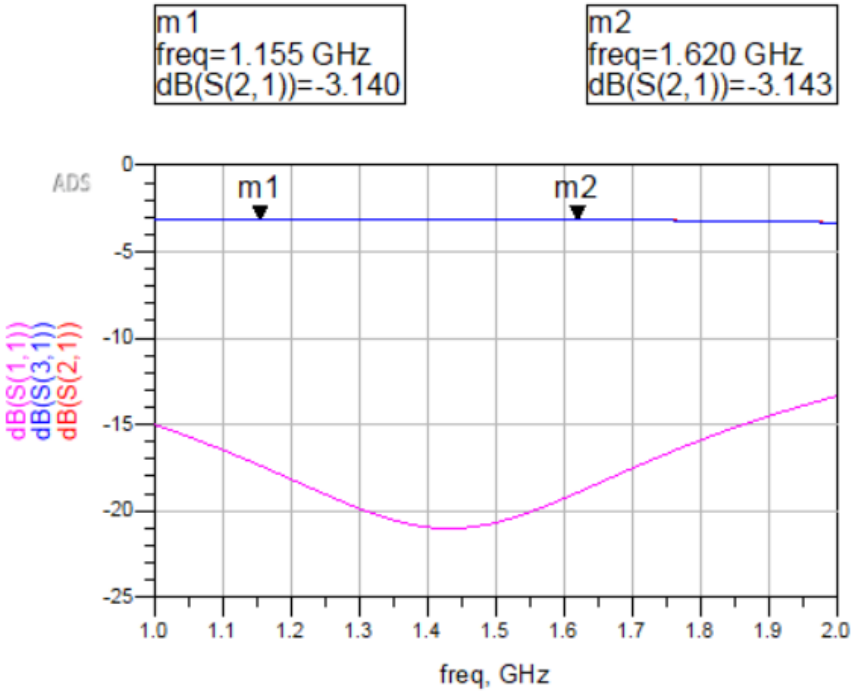

Figure 4.3: S-parameter response of power divider.

4.2 Schiffman phase shifter

The need for a Schiffman Phase shifter is also an essential component for a wideband microwave design since the electrical length of any given transmission line is frequency dependant. Increasing the frequency of the incoming wave, the electrical length of the transmission line will increase and the phase shift of the output signal relative to the input will steadily rise which will result in different relative phase shifts as represented in figure 4.5. As mentioned multiple times this design has the purpose to be a wideband structure ranging from 1164-1610 MHz.

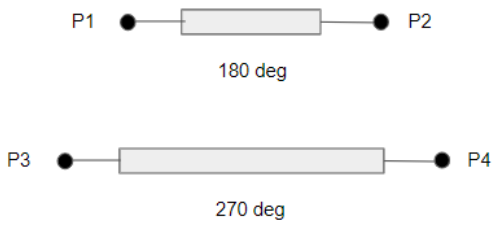

Figure 4.4: Phase shift using transmission lines.

To give a visual presentation of the phase deviation if one was to attempt to create a wideband design using transmission lines, a circuit was simulated in ADS using MoM Microwave EM simulation for 1387 MHz (located at the middle of the band).

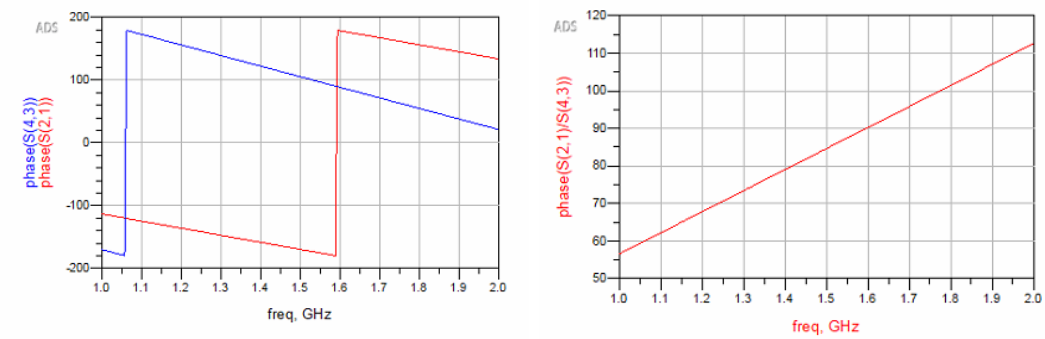

Figure 4.5: Individual phase (left), Phase deviation $\Delta\phi$ (right).

The phase deviation for this application is too broad for the antenna to have a constant AR of <3dB, which is why there is a need for a microwave component that achieves a regular phase shift, hence the need for a Schiffman phase shifter.

Table 4.2: Phase deviation using two transmission lines, parameters from 4.5

Physical length	51.6 mm	77.3 mm	Phase deviation $\Delta\phi$ $(\frac{S_{43}}{S21})$
θ at 1164 MHz	151.06°	226.6°	75.54°
θ at 1387 MHz	180°	270°	90°
θ at 1610 MHz	208.94°	313.41°	104.47°

The Schiffman Type-A network [22] consists of a transmission line with electrical length $\theta = \frac{3}{4}\lambda$ and a coupled line coupler with a total electrical length of $\theta = \frac{1}{2}\lambda$, which is the type of network used in this design.

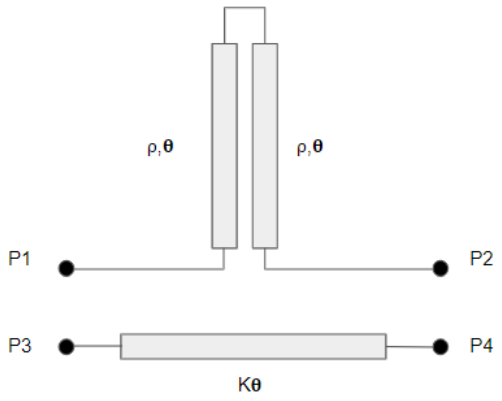

Figure 4.6: Ideal Type-A Schiffman phase shifter

When analyzing the coupled section as done in [22] the analysis is done working in stripline technology, hence working and analyzing pure TEM modes having the same phase velocity for both even and odd modes [3] according to: $\beta = \frac{\omega}{v_p}$. Working in microstrip technology only quasi-TEM modes are supported, i.e odd and even mode of the coupler having different phase velocities since the electromagnetic waves

propagate in both air and the FR4-epoxy, two different materials with distinct dielectric constants. Theoretical approximations are therefore less reliant and tuning is needed in order to realize a wide phase shift.

In order to realize a certain phase shift equation 6, 7 and 8 from [23] is adopted, where K denotes the difference in electrical length between one transmission line the coupled line section and the regular transmission line section. For the Type-A shifter conducted in this design K=3, where θ denotes the electrical length of one section, i.e βl.

$$\rho = \frac{Z_{0e}}{Z_{0o}} \tag{4.2}$$

$$C = -20log(\frac{\rho - 1}{\rho + 1}) \tag{4.3}$$

$$\Delta\phi = K\theta - cos^{-1}(\frac{\rho - tan^2\theta}{+tan^2\theta}) \tag{4.4}$$

Using equation 4.4 with K=3 and θ=90° for the desired frequency (1387 MHz), it can be seen that when the electrical length is approaching $\frac{\lambda}{4}$ the $tan^2\theta$ term is approaching 1, the cos^{-1} term is equal to that of the coupling.
As ρ approaches 1, the coupling (C) approaches infinity and the cos^{-1} term approaches zero hence achieving a phase shift close to $\Delta\phi = 270° - 180° = 90°$.

The conclusion is that when coupling between the lines increase the phase deviation of the two lines approaches 90 degrees. In reality using microstrip technology this cannot be achieves due to manufacturing standards having a minimum requiring of spacing between microstrip lines, but in stripline technology this can be realized due to the fact that the stripline transmission lines can be placed on top of eachother inside the substrate allowing for even smaller distances between the two transmission lines and hence achieving a higher coupling factor C.

$$\Delta\phi = \frac{3\pi}{4} - cos^{-1}(\frac{\rho - tan^2\pi/4}{\rho + tan^2\pi/4}) = \frac{3\pi}{4} - cos^{-1}(\frac{\rho - 1}{\rho + 1}) = \frac{3}{4}\pi - \frac{1}{2}\pi \tag{4.5}$$

Since the phase shift of the transmission line in figure 4.6 has a constant shift dependant on frequency the coupled line coupler has to be designed in such a way that the phase shift of the coupled lines has an equal decline in phase to that of the transmission line over the bandwidth for the phase between the output ports (P2 and P4) to remain constant relative to eachother.

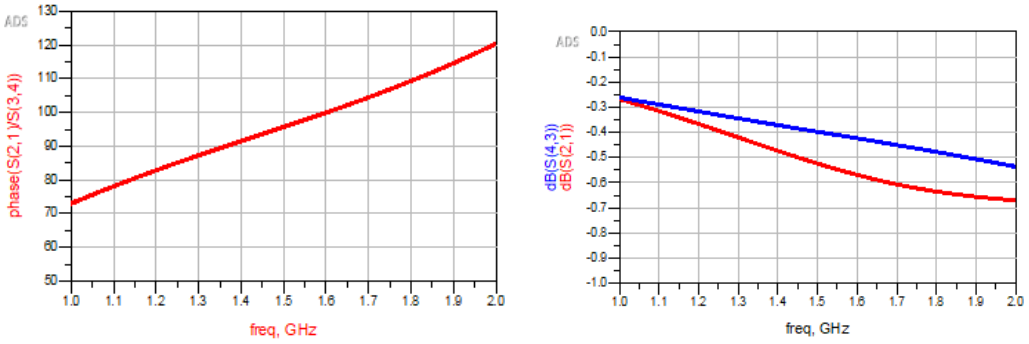

Figure 4.7: Phase difference $\Delta\phi$ between the coupled lines and the transmission line (left) W=0.426 mm, Transmitted power at port 2 and 4 (right).

Using Momentum simulation in ADS the coupled line coupler were simulated with a distance between the lines of the minimum of 0.15 mm, and a width of 0.426 mm. As can be seen in 4.8 the phase differs by roughly +/- 11 degrees over the bandwidth. In an attempt to reduce the phase deviance as much as possible the width of the transmission line was decreased to the minimum of 0.15 mm. This proved to minimize the phase deviation at the expense of increasing the deviation of power at the coupled line output port by roughly 0.5 dB at the highest frequency of 1610 MHz, but reducing the maximum phase deviation to +/- 5 degrees.

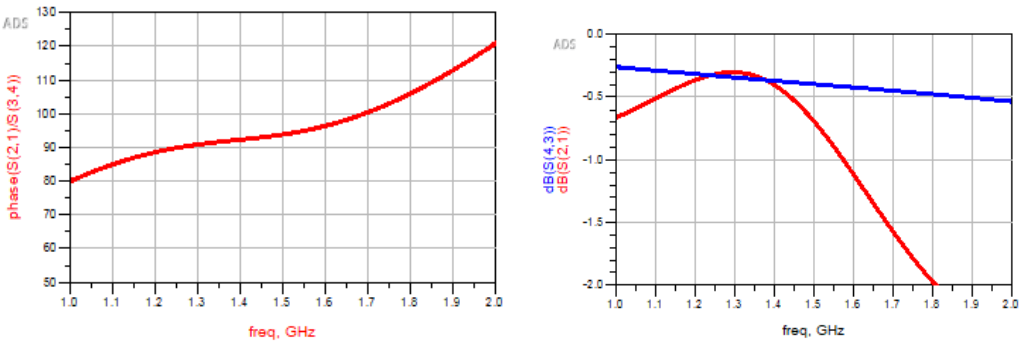

Figure 4.8: Phase difference $\Delta\phi$ between the coupled lines and the transmission line (left) W=0.15 mm, Transmitted power at port 2 and 4 (right).

4.3 Rat Race Coupler

The novel rat-race coupler consists of four different ports, where the incident port can be set as port 1 or 4, also refered to as the sum ($\sum$) and difference (Δ) ports. Having the incident port at the sum port will generate an equal power division with both output ports (2 and 3) in phase, while having the incident port at the difference port will result in the output ports being 180 degrees out of phase.

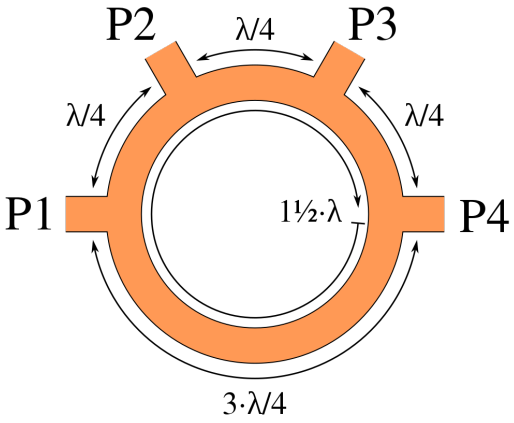

Figure 4.9: Rat race coupler from [11]

The major issue with the novel ring type design is the large size of the the ring. Having a circumference of 1.5λ (177 mm) is equivalent to having a diameter of 56.4 mm. In the current design where the feeding pins are placed carefully on specific locations the ring design would either overlap at the feeding points or keep one point encircled leaving no room to connect the wilkinson power divider and the Schiffman phase shifter.

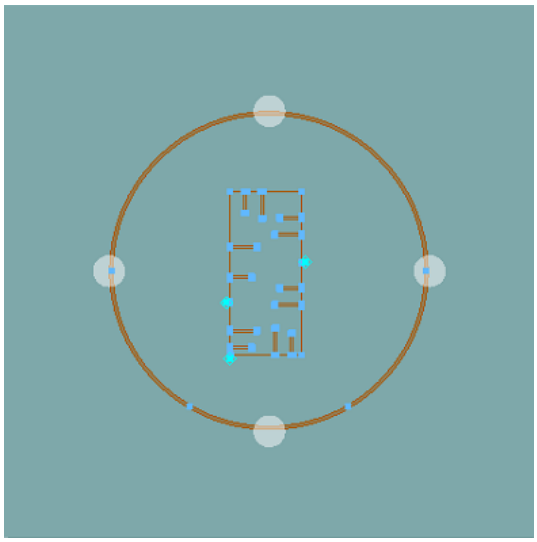

Figure 4.10: Size difference of the standard and compressed design.

In order to reduce the size the ring can either be replaced by passive components by placing inductors and conductors in a specific arrangement to inherit the same characteristics as the ring hybrid or it can be performed with meandered lines [24] to have an equal electrical length to that of the ring hybrid while occupying a fraction of the area of the novel rat race coupler. In [24] a size reduction of 94% is achieved using meandered lines, which is a large improvement especially for circuits operating at lower frequencies. As can be seen in figure 4.10 the standard ring design with a diameter of 56.4 mm will either encircle or overlap the feeding points to the antenna,

as well as trying to design the overall circuitry in such a way as to leave enough space for the LNA circuitry, introduced in section 5. The diameter (56.4 mm) of the ring hybrid with an area of 2'500mm^2 has been compressed to a (31x13 mm) rectangle with an area of 403mm^2 effectively reducing the overall area to a $\frac{1}{6}$th of the novel rat race coupler.

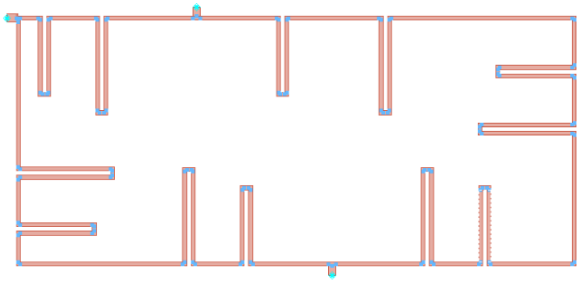

Figure 4.11: Compressed Rat Race coupler

4.4 Complete Network

The final design consists of one ratrace coupler connected to a wilkinson power divider combined to a schiffman phase shifter at each of its' two output ports. By careful design to increase the coupling in the Schiffman phase shifter, see section 4.2, a somewhat stable phaseshift is achieved in the entire GNSS band.

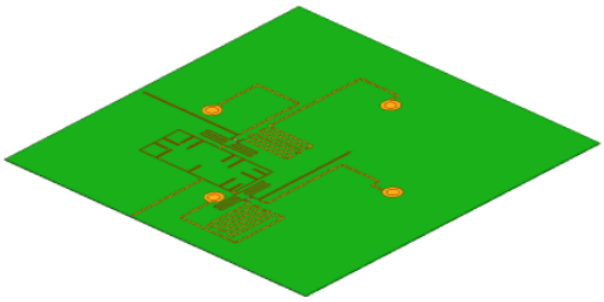

Figure 4.12: Full feed net built in HFSS.

As can be seen in figure 4.13 the relative phase between each port has a stable characteristic of 90°. The deviation has its' maximum at +/- 5 degrees for the entire GNSS band (1164-1610 MHz).

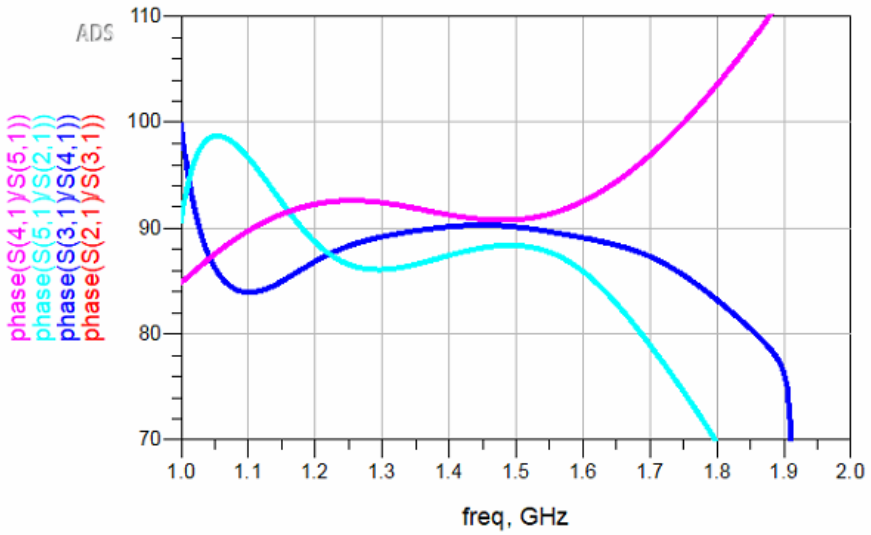

Figure 4.13: Relative phase characteristic between each output branch of the feeding network, simulated in ADS.

The stable phase deviation in this design does however introduce an increased power deviation between ports. The reduced width of the Schiffman section results in an increased impedance meaning we have a modest mismatch meaning an increased power reflected. This results in a maximum mismatch between port 3 and port 4, where the maximum can be seen in the right figure of 4.14 at the lower (1164 MHz) and upper (1610 MHz)- frequencies, where the maximum deviation is approximately 2 dB.

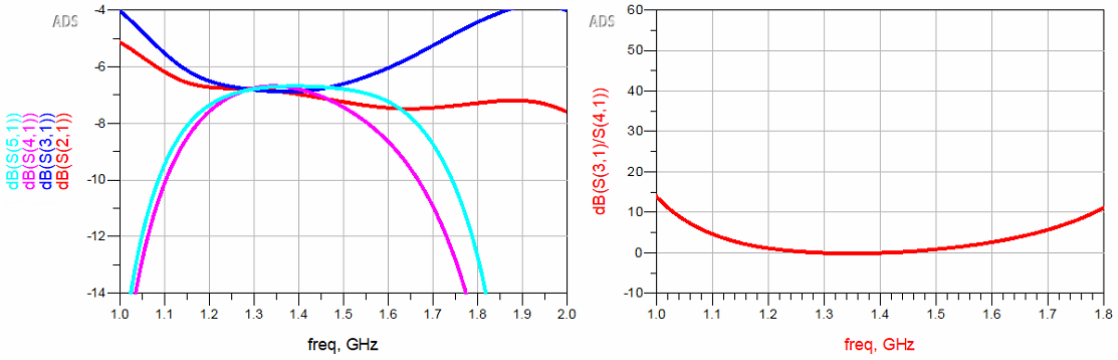

Figure 4.14: Power output at each port in dB (left), maximum power deviation between two ports (right).

5
LNA design

This chapter concludes the steps taken for the design of the LNA and analyze of the data given by the various simulations.

5.1 Design specification

The following specifications in table 5.1 is the initial target specifications for the design of the LNA.

Table 5.1: LNA specific specifications

Return loss S_{11}	<-15dB
Return loss S_{22}	<-20dB
Gain S_{21}	> 20dB
Noise factor NF	< 0.7 dB
Bandwidth	Broad band 1164-1210 and 1550-1610 MHz
Single positive feed	

5.2 Choice of transistor

The choice of transistor was discussed extensively in the beginning, as there are several transistors that have the desired performance, so almost all lack single positive feed, which was one of the design specifications for the project. There were also thoughts of using more ready-made circuits, which in principle are just to connect, however, this would have compromised too much with the actual learning of the project. So after discussion with supervisors, the proposed components for this project is listed in table 5.2.

Table 5.2: Different types of transistors

Transistor name	**Type**	**Main Advantages**	**Main Disadvantages**
Infineon CFY25	JFET	Space grade	Cost > New space
Qorvo FPD750	P-HEMT	inhouse at Ruag	Requires negative voltage
Ommics CGY2107	P-HEMT	Dual LNA, good S_{11} S_{22} match	Requires negative voltage
Broadcom ATF-55143	E-HEMT	Only requires positive voltage	obsolete, no automotive grade
Bipolar transistors	HBT	Can be fed with positive voltage	High noise, no automotive grade

The Infineon transistor would provide a component with space gradation and acceptable gain, but the cost of these components exceeds the classification for this project. In addition, it has a noise factor of over 2dB which makes it unsuitable for this project. The Qorvo and Ommics transistors shows good properties in both matching, noise and amplification, but lack the positive supply that is sought after. The bipolar transistors can work but tend to give a higher noise factor. Further discussions with supervisors at Beyond Gravity made the decision to focus on a single power supply system as this would allow one to connect the power supply with a single coaxial cable and avoid a separate DC power supply and socket. Therefore, the choice was made to continue the design with the Broadcom ATF-55143 due to its only positive DC supply.

5.2.1 Broadcom ATF-55143

This transistor is what is called an Enhancement Mode Pseudomorphic High Electron Mobility Transistor or (E-PHEMT). Enhancement mode means that the transistor begins to conduct current for positive gate voltages, eliminating the need to provide a negative voltage to the circuit. The electrical performance exhibits a very low leakage drain-source current of 10 μA at room temperature, this is achieved due to a buried gate, smaller recess depth and optimization of the InGaAs channel, see figure 5.1 for cross section [12]. The complete system is designed as a microwave amplifier that works in the frequency band of 450 MHz- 6 GHz.

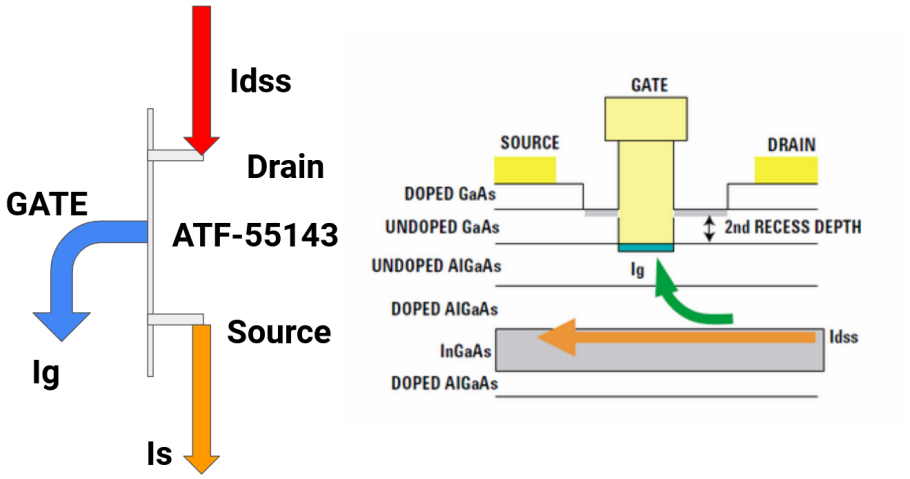

Figure 5.1: Internal structure of ATF-55143. [12]

5.3 Performance curves

5.3.1 DC-analysis

The primary approach to the design was to determine the DC operating point of the transistor, this is done to establish that the amplifier will operate in the active area where the noise ratio, gain and linearity also meet the target specifications. The S parameter of the transistors was implemented in ADS together with gate and drain voltage sources, see figure 5.2. From the data sheet it was determined that the suitable bias point was 3V at the VDS source and that the gate source was at 0.45V. This was to establish a drainage current of about 10mA and a low noise factor. This point of selection is better known as the quiescent point. See figure 5.3 for IV properties and marker m1 for the quiescent point.

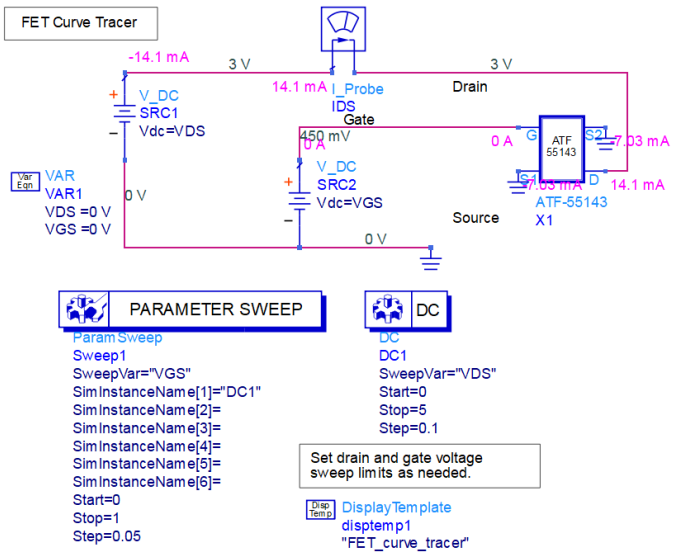

Figure 5.2: Schematic for analyzing IV characteristics

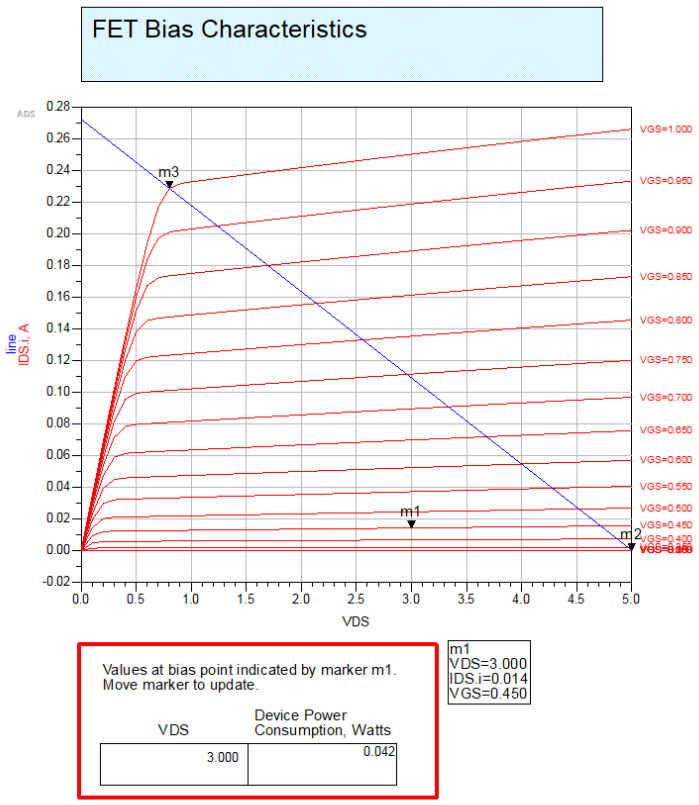

Figure 5.3: IV characteristics, marker m1 sets the quiescent point

5.3.2 S-parameters simulation

The file implemented from previous section also contains the noise figures over the whole frequency of operation. The following graphs in figure 5.5, 5.6, 5.7 demonstrates the performance of the transistor without matching sections, only 50Ω terminations, DC blocks and DC feeds, for the chosen quiescent point. The noise is sufficiently low for the entire bandwidth, furthermore the transistor is not stable over the desired bandwidth and matching of the input and output sections is to be addressed in order to meet the required specifications.

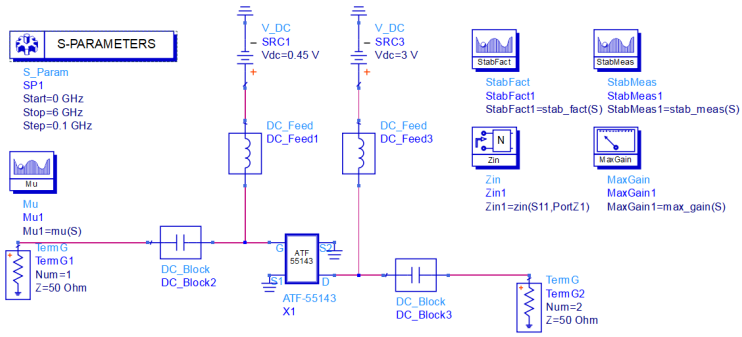

Figure 5.4

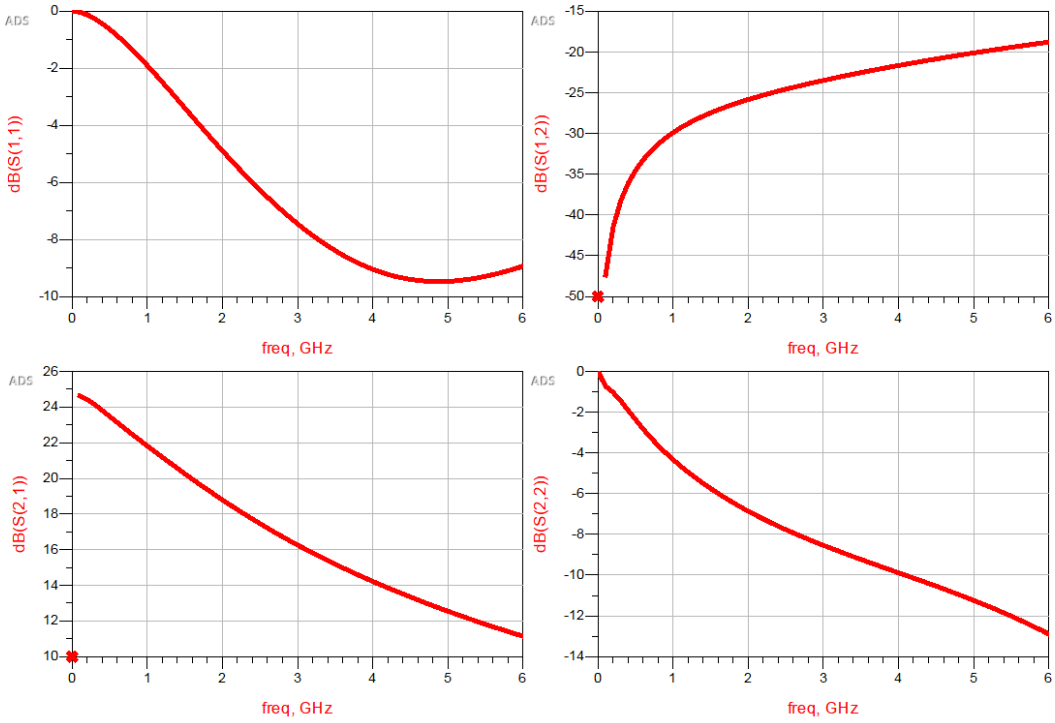

Figure 5.5: S-parameters for chosen bias point

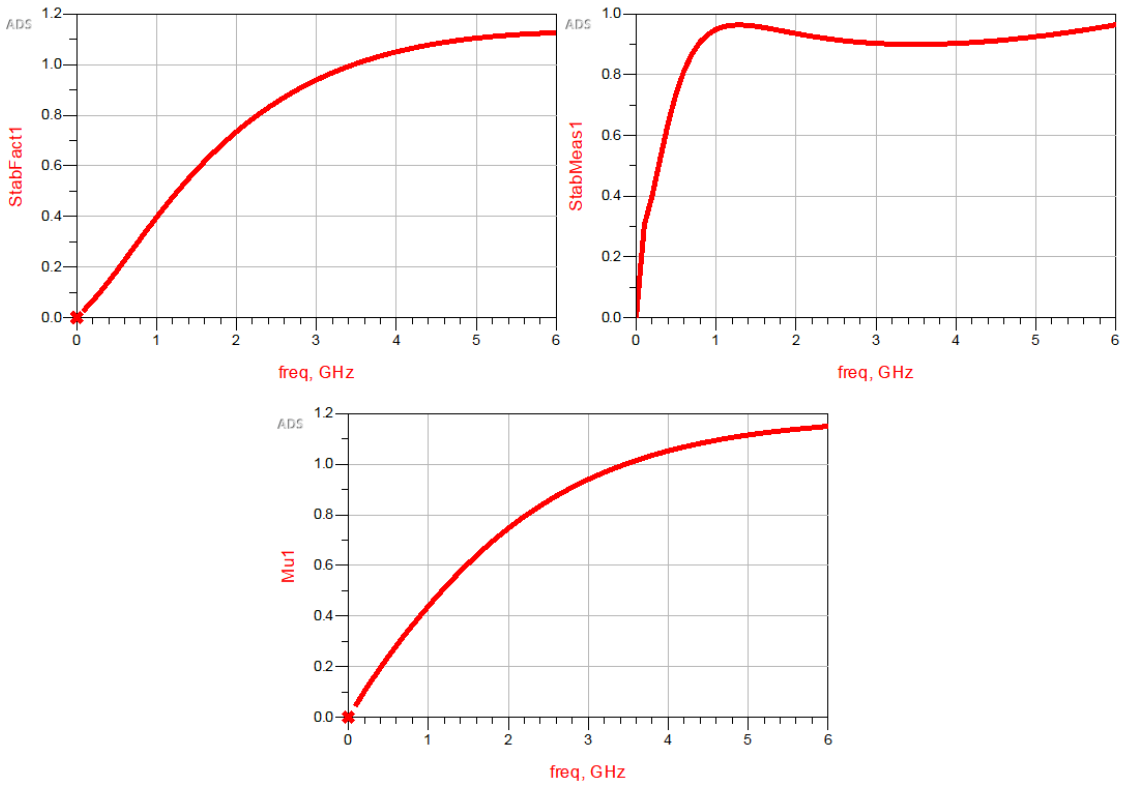

Figure 5.6: Stability simulations

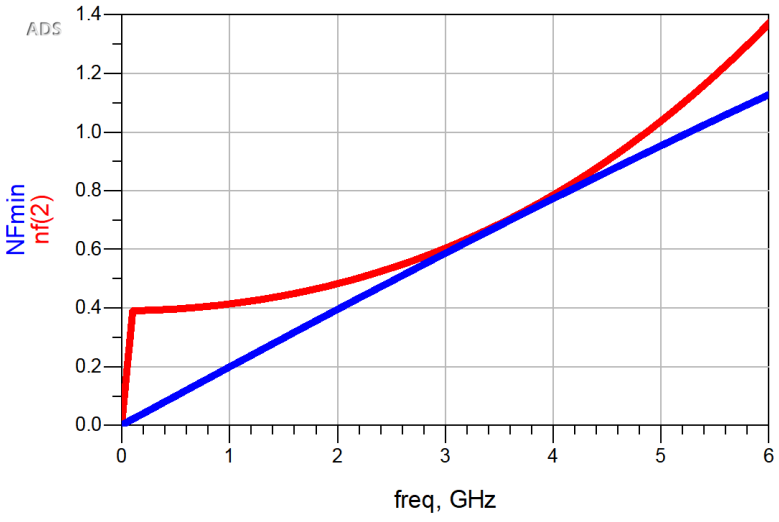

Figure 5.7: Noise simulation

5.4 Transistor Biasing with ideal components

To obtain the bias condition of $V_{DS} = 2.7V$ with a drain current of $I_{DS} = 10mA$, V_{GS} needs to be set at 0.47V. The choice was made to go with a passive biasing network, which over an active bias network yields reduction in size and complexity which was of concern due to the requirements. The passive network is accomplished by using a series of voltage divider resistors, the datasheet for the transistor provided the equations for calculating this. The parameters used is explained below:

V_{DD} Is the power supply voltage
V_{DS} Is the drain to source voltage
V_{GS} Is the gate to source voltage
I_{DS} Is the proposed drain current
I_{BB} Is the current through the voltage divider network

I_{BB} should be chosen with respect to the gate leakage current previously mentioned in section 5.2.1 by conservatively having a value of at least 10 times larger, chosen value for this was set to 0.5mA.

$$R_1 = \frac{V_{GS}}{I_{BB}} \tag{5.1}$$

$$R_2 = \frac{(V_{DS} - V_{GS})R_1}{V_{GS}} \tag{5.2}$$

$$R_3 = \frac{V_{DD} - V_{DS}}{I_{DS} + I_{BB}} \tag{5.3}$$

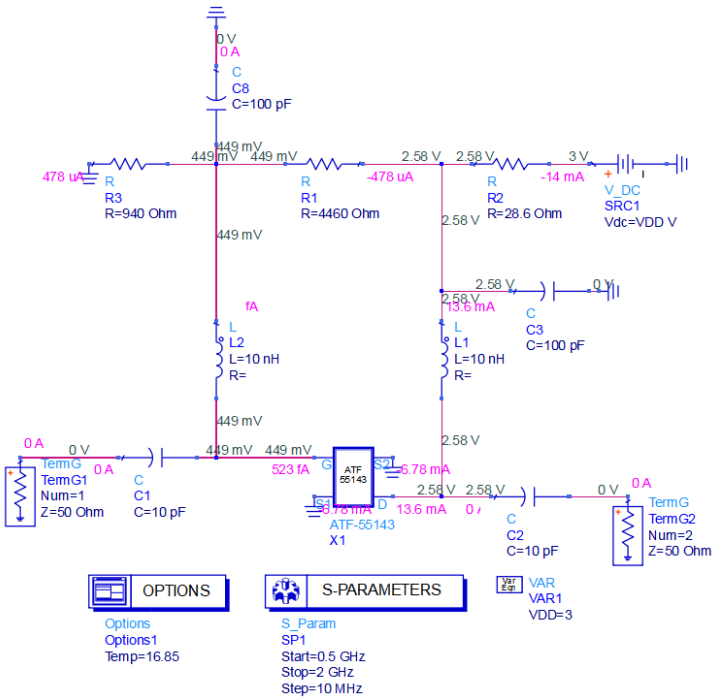

Figure 5.8: Bias network with resistor voltage dividers

The resistor values calculated from above was converted to $R_1 = 4460\Omega$, $R_2 = 28.6\Omega$ and $R_3 = 940\Omega$, figure 5.8 demonstrates the complete bias topology from above values. During this point one can also see that two decoupling capacitors with 100μF as well as two RF chokes of 10nH on both the gate and drain side was implemented. This is to relax the bias network for RF signals leaking into the network.

5.4.1 Conductor and substrate technology

The utilization of microstrip in microwave systems is one of the more commonly used techniques. It is popular because the ease of fabrication and a wide range of impedance and coupling values makes it increasingly ideal in more cases than lumped components in matching networks for example.
Microstrip is printed as a copper strip placed above a certain dielectric with determined permittivity ϵ_r, so by determining the thickness (H) of the dielectric and the width (W) of the strip one can determine a suitable impedance match, see figure 5.9.

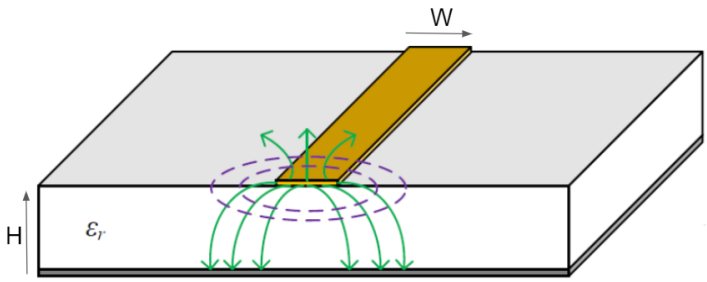

Figure 5.9: Visualization of microstrip technology

The absence of a dielectric above the strip presents with some of the electrical field lines above the strip in the air region, while the rest is concentrated in the dielectric between the strip and the ground plane, hence the permittivity ϵ_r of the dielectric satisfies the effective dielectric constant with the relation:

$$1 < \epsilon_e < \epsilon_r \tag{5.4}$$

This is further more dependant on the substrates' thickness and width and the field lines will for this thesis be considered as quasi-TEM, which is ultimately assuming that the fields is presented in the same way as in a static case. The dielectric used throughout the design process will be the epoxy laminated material FR4, for the main reason with it being less expensive than other materials and suits well for prototype designs. Though with the constraint that the actual permittivity of the material can change depending on manufacturer in the range of 4.05 - 4.6 or even more in some cases. This could severly affect many components in the circuit with it being changes in the actual impedance's of the conductive traces as well as causing shifting in the frequency response. Therefor it is common practice to make the circuit "tuneable" upon fabrication. Furthermore, microstrip technology

will be used as the conductor between transistor and all the corresponding passive components in the network.

5.5 Matching network techniques

The fundamental idea of matching networks arises because amplifiers needs to deliver maximum power to a load and/or perform in a certain way, it is also of importance to remember that the input and output matching networks effect the stability of the transistor. A negative impedance from any side would imply that $|\Gamma_{in}| > 1$ or $|\Gamma_{out}| > 1$ [3]. As a side note of demonstration of a perfectly matched input and output section gives $\Gamma_S = \Gamma_L = 0$ and will reduce the transducer gain function to:

$$G_T = \frac{P_{Delivered}}{P_{Available}} = \frac{|S_{21}|^2(1-|\Gamma_S|^2)(1|\Gamma_L|^2)}{|1-|1-\Gamma_S\Gamma_{in}|^2|1-S_{22}*\Gamma_L|^2} = |S_{21}|^2 \tag{5.5}$$

Where S_{21} is the transistors own amplification. The previous section 2.3.5 of matching networks has already described the fundamentals of this concept a bit more, this section will however consider the design process and a number of theoretical comparisons of design typologies considered and analyzed.

5.5.1 Single stub tuning

One of the more popular techniques of implementing a matching network is by utilizing microstrips. It is done by using a single open or short circuited transmission line, also called stub, which is connected to the main line in parallel or in series with the transmission line. As previously mentioned in microstrip theory section 2.3.5, it was described how impedance can be changed by altering the width and thickness of the dielectric. In single stub tuning, the two parameters which are modified is the distance d from the load to the stubs position and the value of reactance or susceptance controlled by the stub. A simulation of above can be structured as in figure 5.10

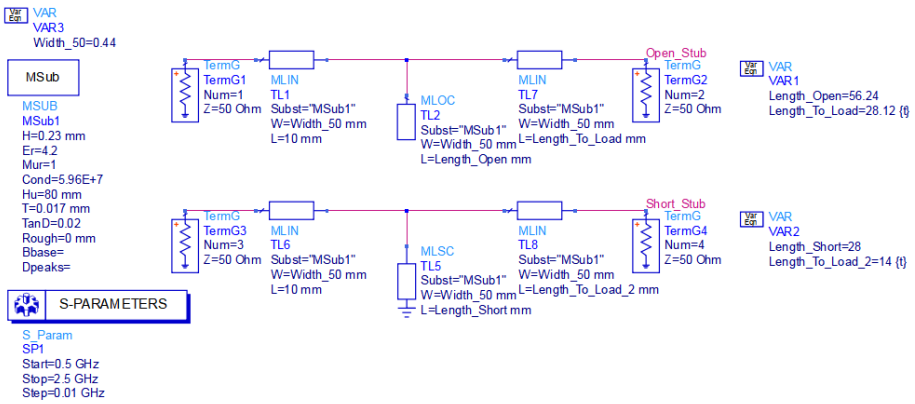

Figure 5.10: Schematic view of open and shorted stubs

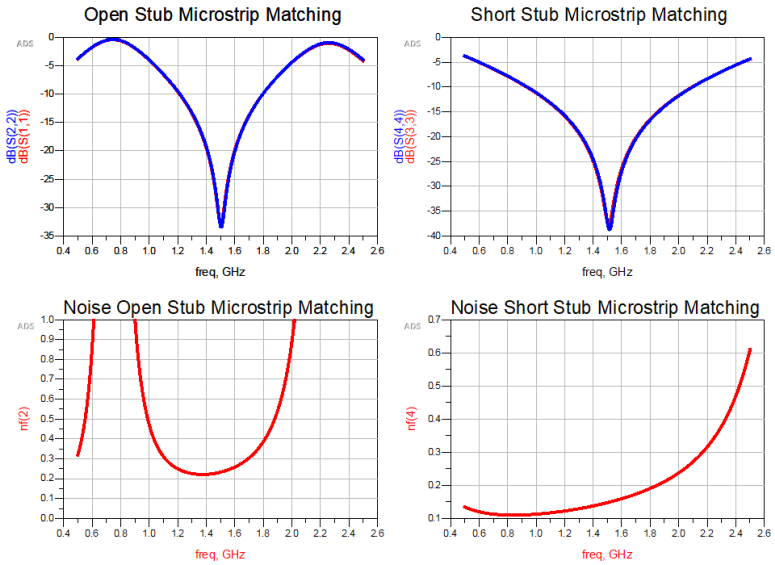

Figure 5.11: Performance graphs of stubs

Referring to figure 5.11, one can see that it is possible to match the load with both types of techniques. What is also important to highlight is the fact that open stubs generally presents with a higher noise which occurs due to the strip tends to radiate more. On the other hand, open stubs are more suitable in circuits where tuning is applicable due to the absence of ground at the end of the stub. A test of both types of techniques was implemented to the circuit for an overall evaluation.

5.5.2 Simulation of shorted stubs matching Network

The values for the widths and lengths of the transmission lines was calculated by using the input and output reflection and trying to match to the center of the smith chart (50Ω). Below figure 5.12 shows the complete circuit match for the input and output section.

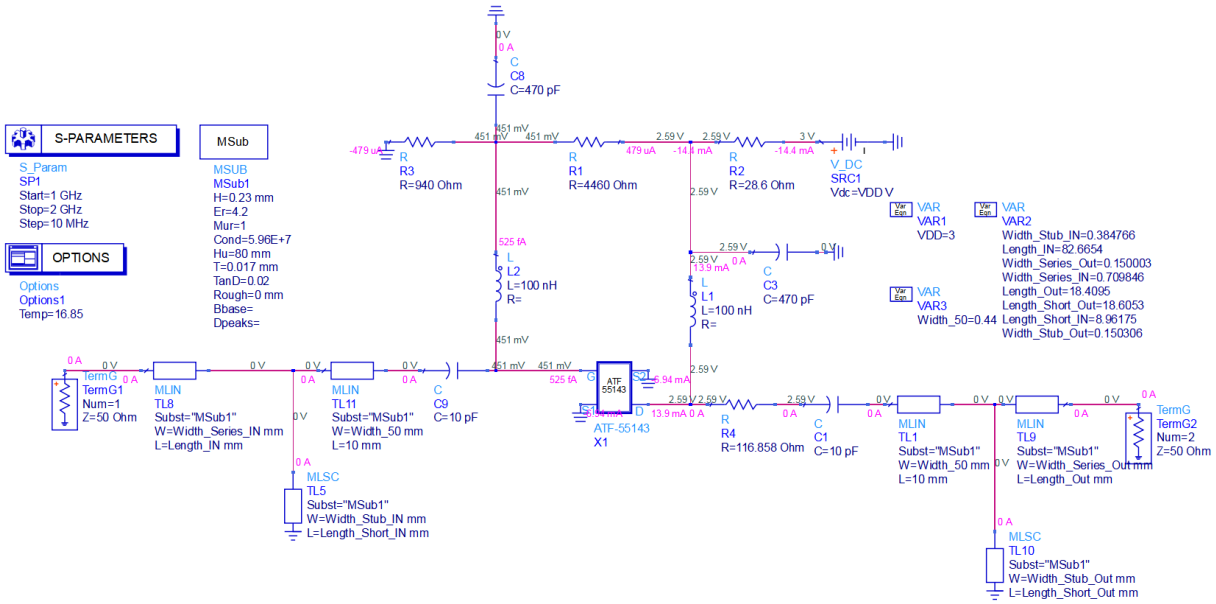

Figure 5.12: Short stub matching at input and output

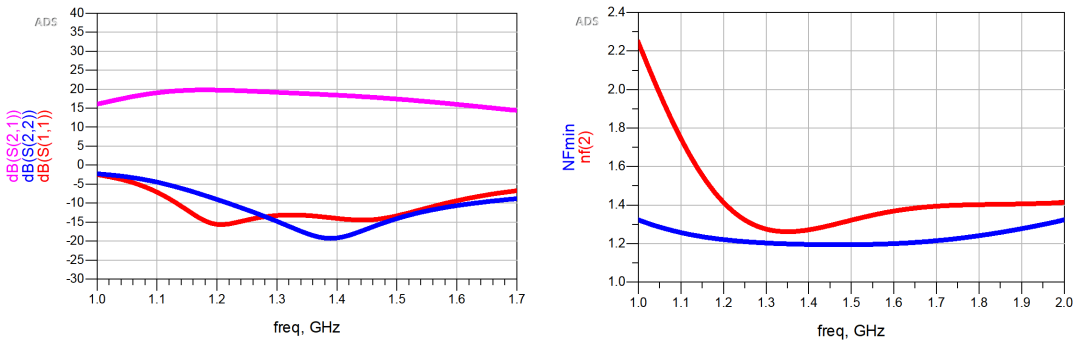

Figure 5.13: (left)Input and output s-parameters of shorted stubs, (right) Noise performance

The overall matching capabilities of this technique shows promising results, especially for the input (S_{11}), see figure 5.13 which gives a return loss below -10dB for the whole bandwidth. The main drawback of this technique demonstrates a more difficult match for output (S_{22}) as well as 3dB lower gain in the upper frequency band. Finally the noise exhibits an increase that is almost twice as high as the design requirement.

5.5.3 Simulation of open stubs matching Network

A similar approach as previous was done with open stubs. Some changes to the output resistance was needed to maintain stability. Figure 5.14 demonstrates the schematic for open stub matching, and figure 5.15 shows to resulting performance.

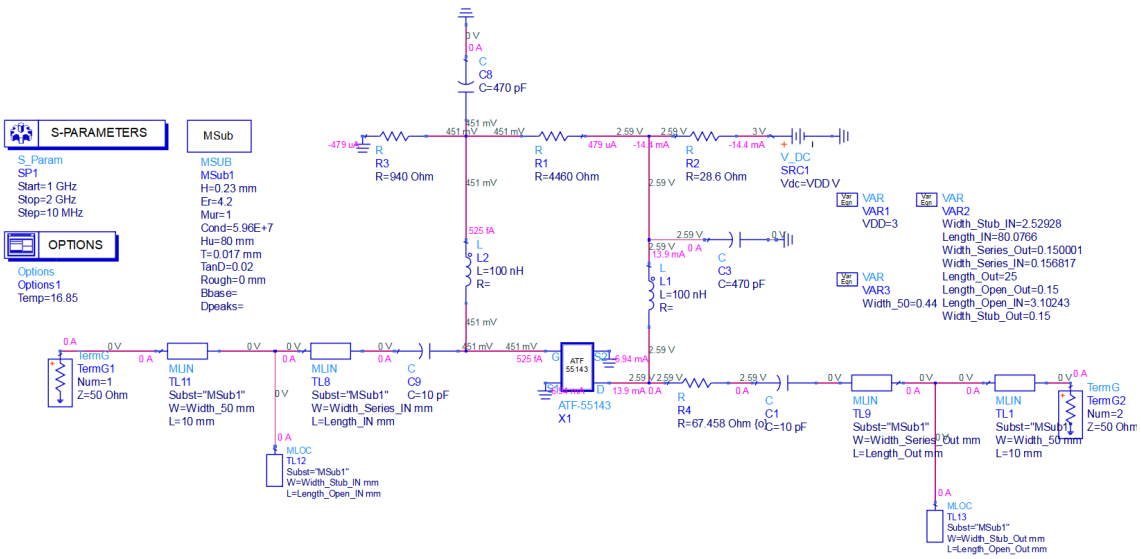

Figure 5.14: Open stub matching at input and output

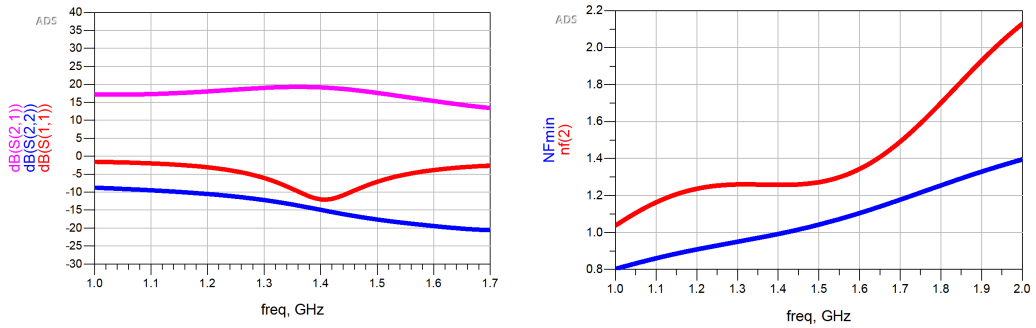

Figure 5.15: (left)Input and output s-parameters of Open stubs, (right) Noise performance

The resulting S-parameters exhibits further degradation to the overall system, with, especially to the input reflection S_{11}. The noise was reduced slightly compared to the latter but the gain was further reduced for both the lower and the upper and lower frequency band.

5.5.4 Lumped Elements Tuning

Using lumped elements provides an easier approach to designing the matching sections, it also enables the designer to change components after fabrication for tuning the circuit. The components can be placed in a similar fashion to the microstrip stubs but with the difference that capacitors and inductors provide the reactive elements. One of the more common ways of implementing them is by creating what is called, π-networks and T-networks, figure 5.16 shows the physical realisation of this.

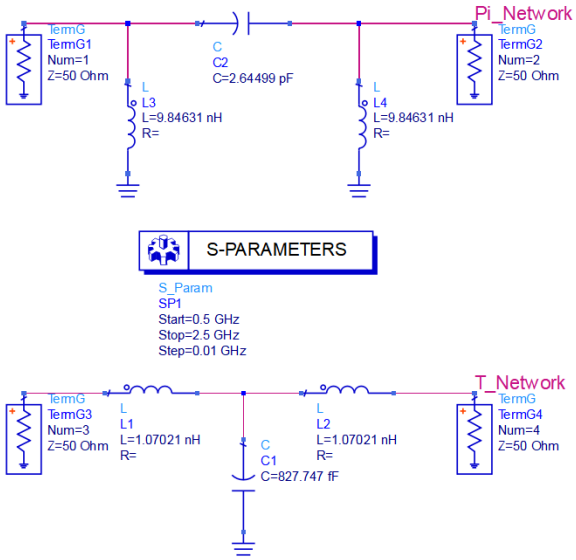

Figure 5.16: π and T matching networks

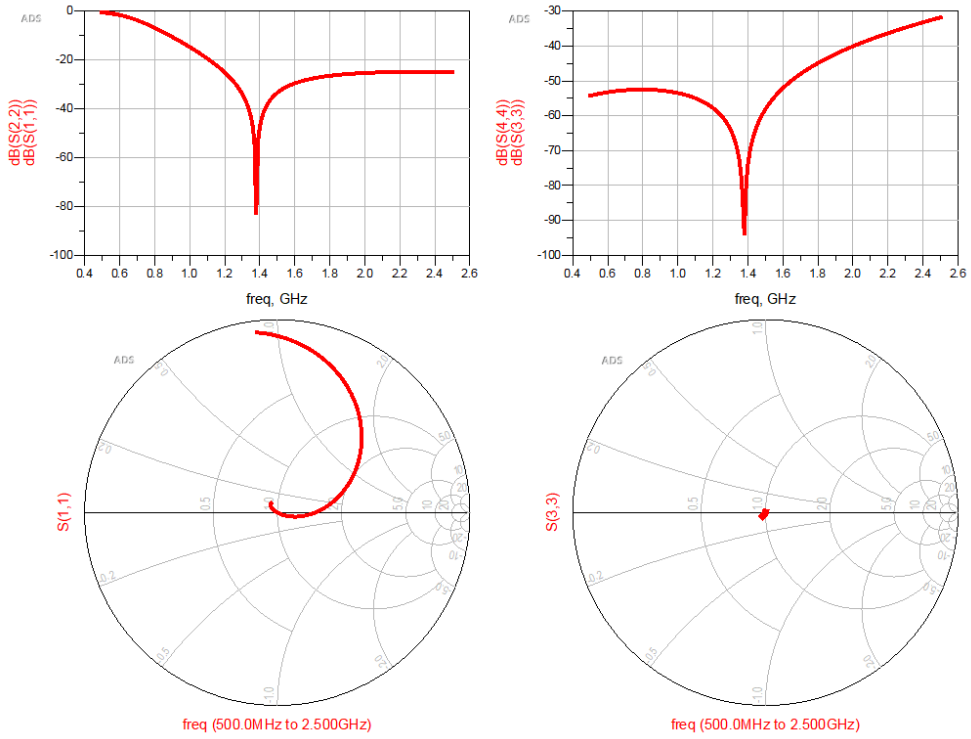

Figure 5.17: Performance curves of π and T matching networks

5.5.5 Simulation of T-Matching Network

The first technique used was implementing the T-network on both the input and output side, and then trying to match to center of the smith chart from the given Γ_S and Γ_L values. The final best design for this type of network is seen in figure 5.18, and the corresponding performance curves in figure 5.19. Also notice the

resistance on both the gate and drain side of the transistor which had to be used for stabilization.

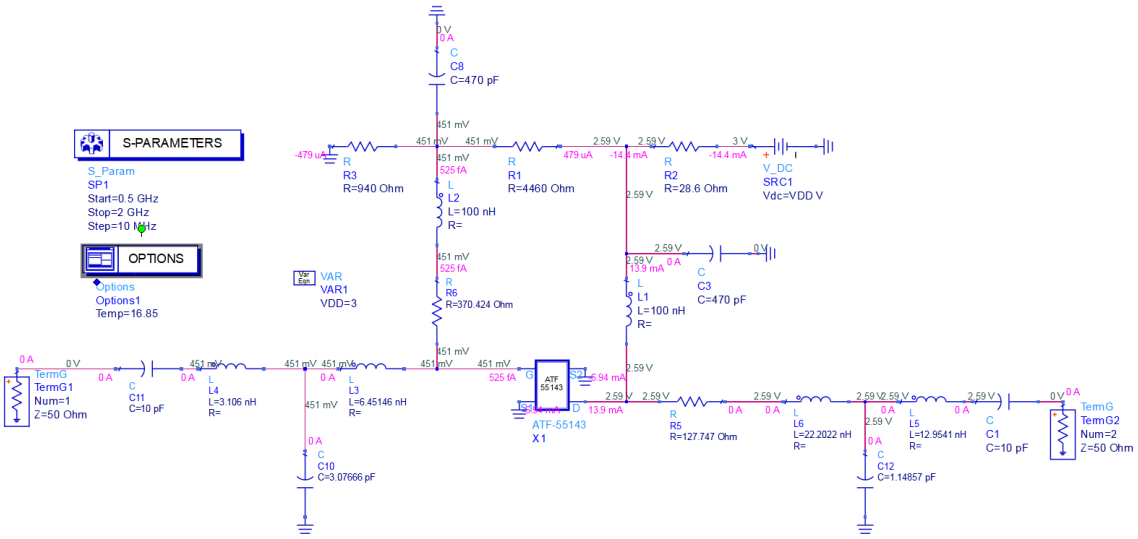

Figure 5.18: Lumped component schematic of T-matching network

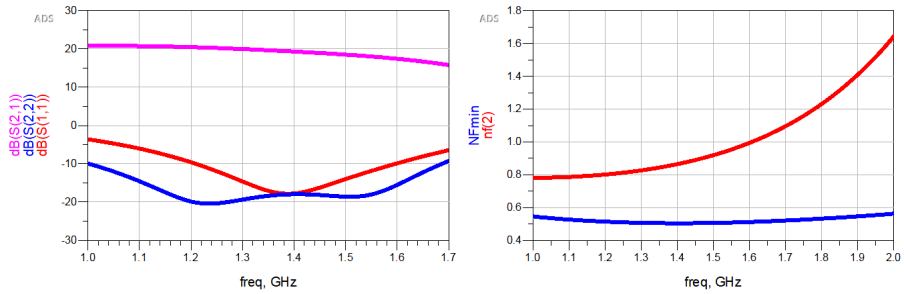

Figure 5.19: Performance curves of T-matching network

The return loss of the input and output section seen in figure 5.19 shows acceptable bandwidth on S_{22} but worse for the input section S_{11}. One key feature that highlights lumped components over microstrip even though ideal components is used here is the noise contribution, the simulated circuit demonstrates that the overall noise figure is about 0.4dB better than with microstrip technology. Furthermore, the gain over the whole frequency band is more or less replicated as with microstrip.

5.5.6 Simulation of π-Matching Network

A similar setup as with the T-network was implemented, and as before some changes to stability resistors had to be addressed. Also the DC-block capacitors was moved in before the π-network because of of current leaking into the grounded inductors of the network. Figure 5.20 shows the complete schematic, and figure 5.21 demonstrates to performance.

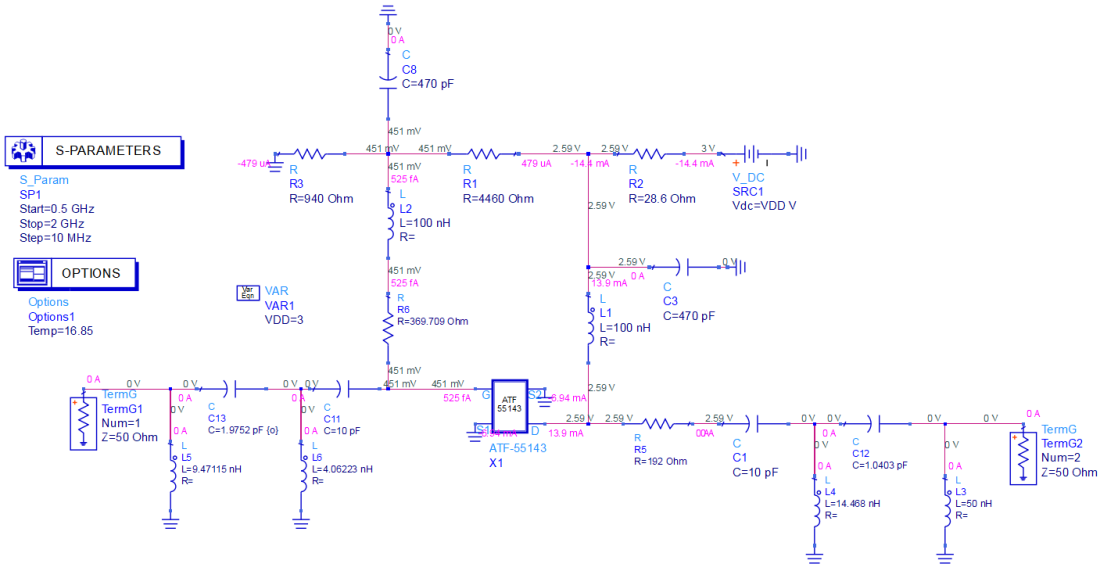

Figure 5.20: Lumped component schematic of π-matching network

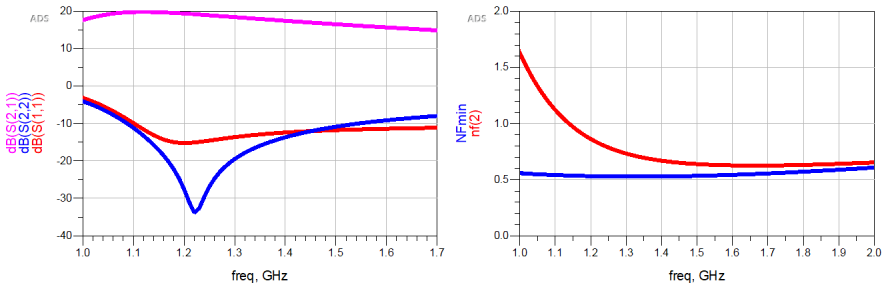

Figure 5.21: Performance curves of π-matching network

The performance of this network exhibits similar noise figures compared to the T-network which is expected. The lower band is also in acceptable range of input and output reflection but the upper band falls outside to acceptable range. The gain again sees a similar outcome as all previous tests.

5.6 Typology investigation

Additional tests with a single-stage transistor showed promising results for matching and optimizing the lower band, but the upper band lacked the bandwidth needed and the gain was compromised too much. As previously mentioned in all previous tests, it was shown that the gain dropped over the upper band. One idea to increase the gain was to give the transistor higher drain and gate voltages and ultimately increase the drain current. Although this would work to some extent, one must also keep in mind that the noise would increase if one uses this method. Discussions with supervisors at Beyond Gravity suggested looking at additional typologies, more

specifically adding another amplification stage to increase the overall gain while keeping the noise figure low.

5.6.1 Dual stage cascade design

When implementing another amplification stage to the network, should make it theoretically possible to double the gain and as previously mentioned by equation 2.22, while keeping the overall noise contributions low. One concern was to what extent this would affect the overall size of the network and/or how large the bias and matching network would become. With this in mind, the choice was made to use the lumped element design for the matching section, mainly for size considerations and noise reduction.

5.6.2 Biasing cascaded design

The bias network not only supplies power to the amplifier, it also plays a role in the stability of the transistors. To provide better control over this, the decision was made to duplicate the bias network for the second stage, making them more separated from each other. This makes it possible to minimize oscillations and isolates potential unwanted RF leakage currents. The previously selected bias point could also be obtained from earlier, with minor changes of the resistors to display actual resistance values. The update voltages is therefor changed slightly to $V_{DS} = 2.69V$ and $V_{GS} = 0.467V$. The complete schematic for bias design before stabilization can be seen in figure 5.22.

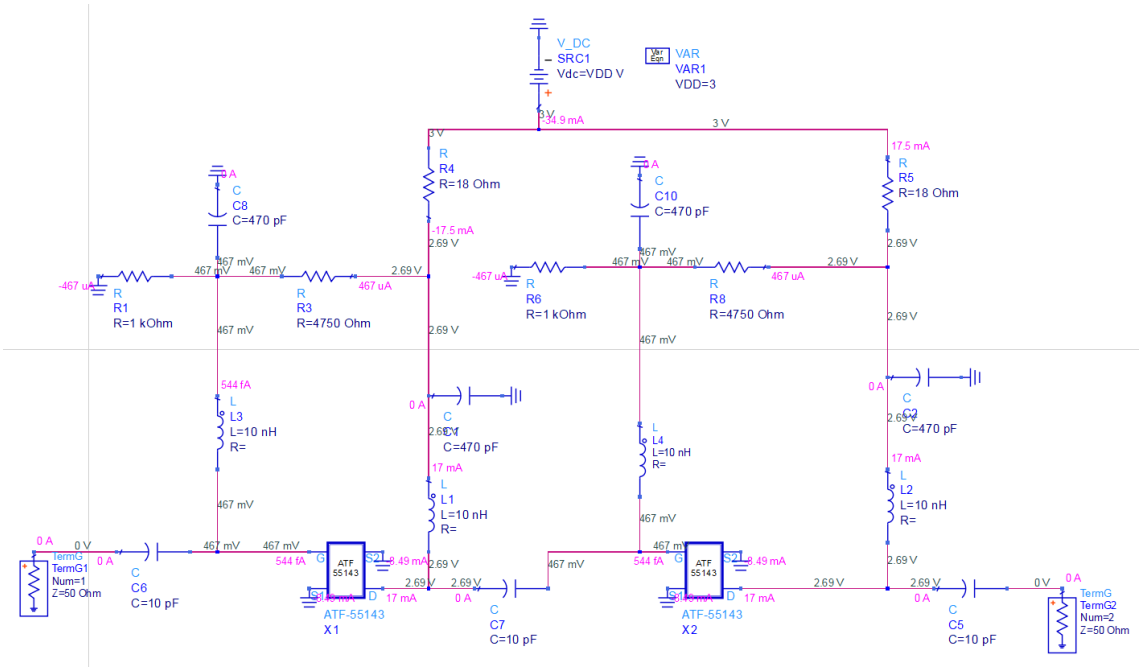

Figure 5.22: Cascade design with corresponding bias networks

5.6.3 Stabilize cascade design

As a more accurate demonstration model, the system needs to be stabilized, and as previously seen, this can easily be done by implementing resistors at certain points in the circuit. A common way to do this is to place them in series or shunt at the output or input of the transistor. It is preferable to stabilize at the output as resistance at the input generally presents a much higher noise figure. Unfortunately, this is not possible with this type of design as a resistance on the output only stabilizes the second stage. Instead, the stabilization had to be done on the input side of both amplifiers. One idea would be to increase the inductance values of the RF chokes as these act as a resistor at higher frequencies. But supervisors at Beyond gravity stated that a general rule of thumb for space components is to avoid high inductive values because these tend to be very reactive and can easily swing in these environments. So instead as a first approach, two resistors were implemented on the input section at both stages in series with the decoupling capacitors C8 and C10, see figure 5.23 for the implementation. This implementation with some tuning to the

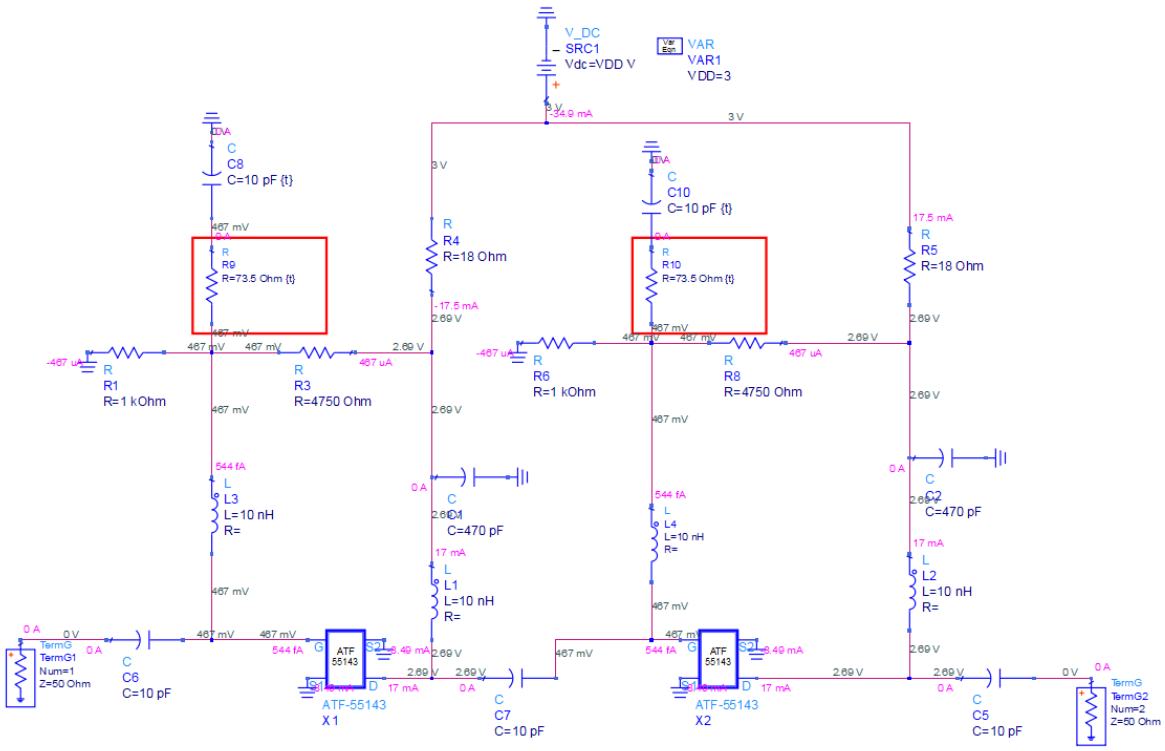

Figure 5.23: Cascade design with stabilization resistors (marked in red)

resistor and capacitance values made the cascaded network stable over the whole bandwidth. Additionally a simulation from 0-10 GHz concluded that the system was unconditionally stable, see figure 5.24

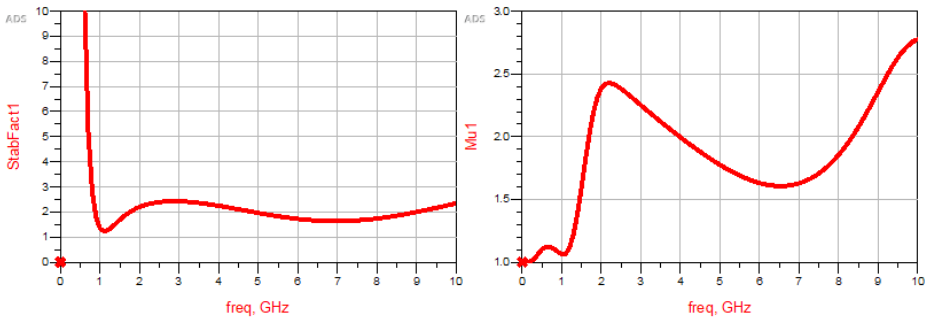

Figure 5.24: Stabilized cascade design

As previously mentioned having a high resistance at the input generally raises the noise and with a resistance of 73.5Ω on the input confirmed this, so in an effort to lower this, a parallel capacitance to the stabilization resistors and series decoupling capacitor was implemented and tuned to optimal value of 8.6 pF respectively. Furthermore, the RF choke inductor on the second stage gate was changed to a resistive load of 81.5Ω instead to balance up the capacitive insertion, see figure 5.25. The overall noise reduction made can be seen in figure 5.26.

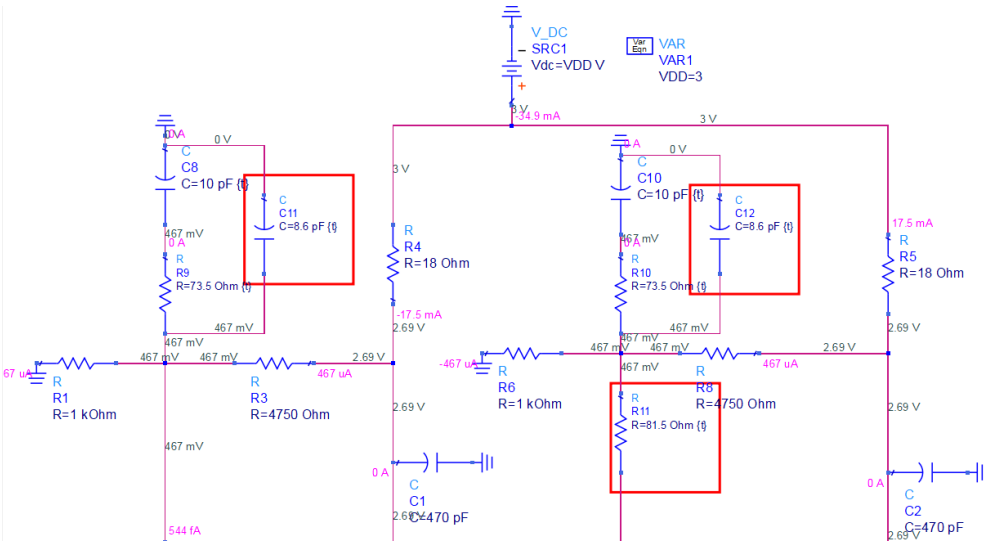

Figure 5.25: Updated cascaded design with optimal noise performance

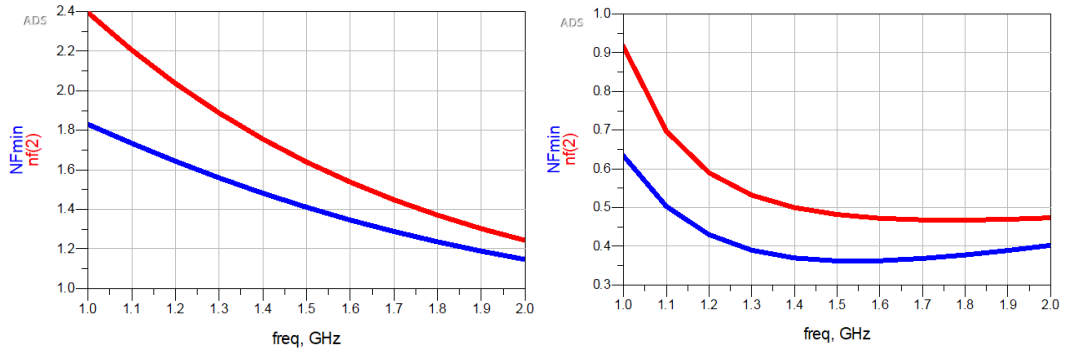

Figure 5.26: Noise without capacitors (left), With capacitors (right)

5.6.4 Noise and Gain circles

Designing an amplifier always brings a balance between optimal noise versus gain. To evaluate this, one can look at the available gain and noise circles at a single frequency, and because this LNA is intended for dual band applications, the following evaluation will look at the center frequencies of both of these. For the lower GNSS band it is 1.185 GHz and for the upper band 1.585 GHz. The ADS components used for this simulation is seen in figure 5.27 together with the lower and upper frequency.

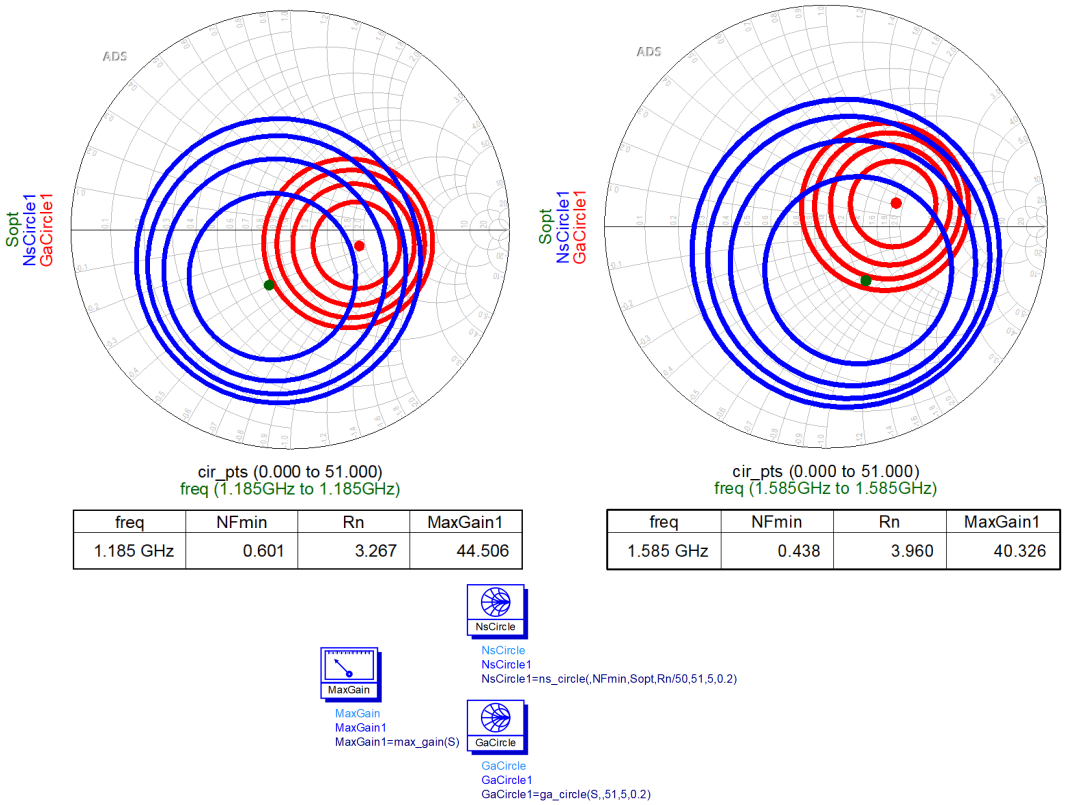

Figure 5.27: Gain and noise circles of lower and upper frequency band

The evaluation confirms appropriate balance between minimum noise and maximum

gain. The noise contribution for the upper band is lower than the below band but at the same time a lower gain. This confirms that some headroom is to be had after a fabrication if test shows the noise is higher than desired, especially for the lower band. It also explains that if the next step of matching is done correct, it should be possible to reach NF_{min} on both input and output at a at a cost of 1dB lower gain on both the upper and lower band, comparing table 5.3 with figure 5.27.

Table 5.3: Noise and gain circle values, values from 5.27

	Noise Circle Values (dB)	Gain Circle Values (dB)
Lower band 1.185 GHz		
1	NF_{min} 0.601	Max gain 44.506
2	0.801	44.306
3	1.001	44.106
4	1.201	43.806
5	1.401	43.606
Upper band 1.585 GHz		
1	NF_{min} 0.438	Max gain 40.326
2	0.638	40.026
3	0.838	39.726
4	1.038	39.426
5	1.238	39.126

5.6.5 Matching network Cascade design

As the previous section about matching network techniques demonstrated, the one which gave the most reasonable noise compared to bandwidth and return loss response was the shunt lumped component T-network. It was therefor the design methodology continuing forward for the cascaded design. A single T-network stage when using lumped components such as before with capacitors and inductors is only suitable for making a perfect match to a certain frequency. For this design the goal was to at a minimum match to the upper and lower band i.e making it dual band. To consider an impedance match over a broad bandwidth or dual band the number of components needs to be multiplied and a proposed design of a 5th order psuedo low pass type design was constructed, see figure 5.28

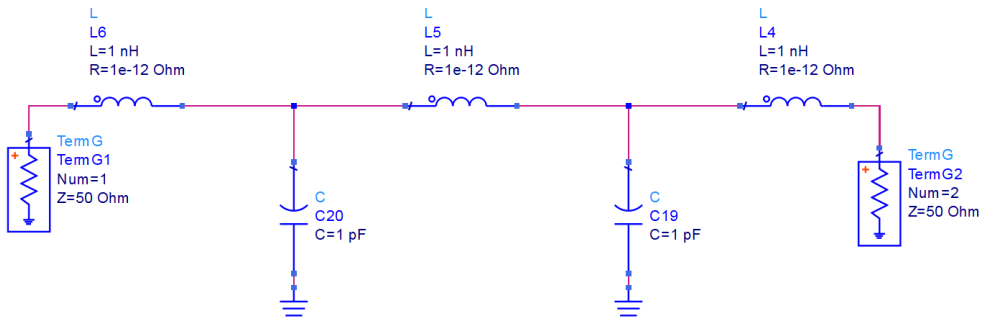

Figure 5.28: Impedance matching 5th order low-pass adaption

This was implemented to the stabilized circuit by looking at the reflection coefficients Γ_S and Γ_L or S_{11} and S_{22} of the center frequency at 1.38GHz. Starting with input side looking at S_{11} at proposed frequency on the smith chart in figure 5.29.

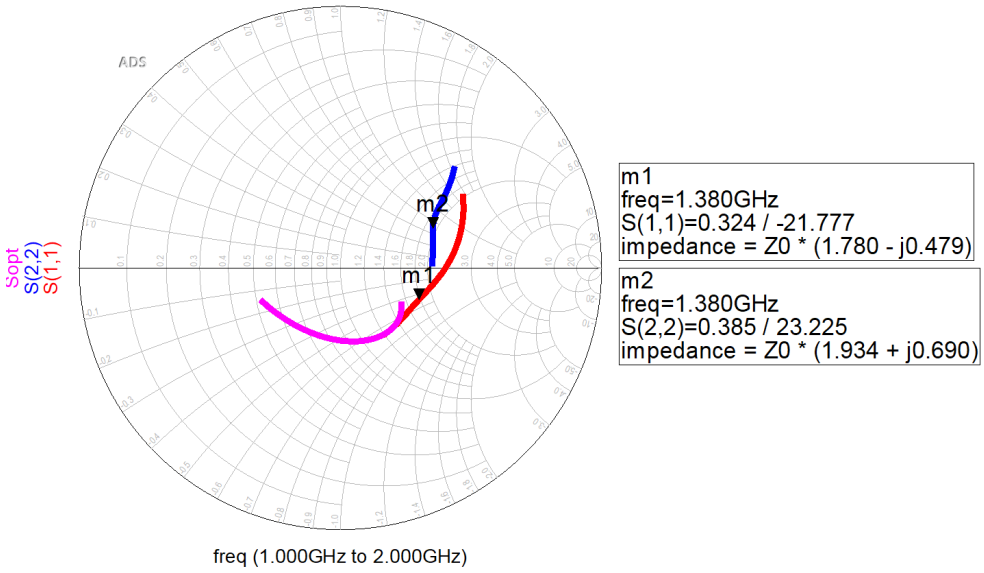

Figure 5.29: Initial S-Paramters of the input and output section

With S_{11} at 89-j*23.9 at 1.38 GHz was this later implemented to the load section in the smith chart tool of ADS using a characteristic impedance Z_0 of 50Ω. Using smith chart for matching, also has a factor that can be used when matching for broadband, this is called the Q-factor which can be seen as two lines centered at the cartesian coordinates of X=0,Y=+/-(1/Q) seen in 5.30. The Q factor is defined as the ratio of frequency to bandwidth, so consequently a high Q value translates to a more narrow band matching and the opposite for low Q. The mathematical definition can also be defined in the form of of which component is used as in 5.6 for an unloaded capacitance and 5.7 for an unloaded inductor. The Q value can also be calculated by bandwidth or reactance to resistance as in equation 5.8 and 5.9. To achieve the optimal Q.

$$Q = \frac{X_c}{R_{ESR}} \tag{5.6}$$

where ESR is the series resistance

$$Q = \frac{X_L}{R} \tag{5.7}$$

where R is the series resistance of the coil

$$Q = \frac{f_c}{\Delta f} = \frac{\omega_c}{\Delta \omega} \tag{5.8}$$

$$Q = |\frac{X}{R}| \tag{5.9}$$

where X is the reactive and R is the real power

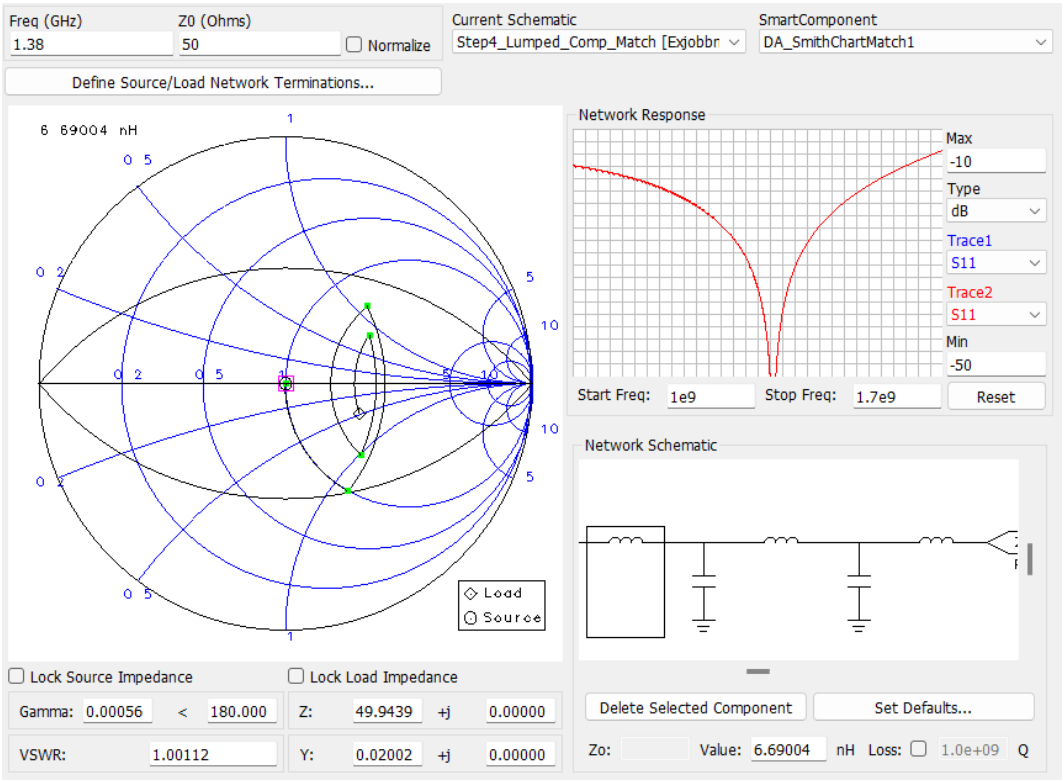

Figure 5.30: Smith chart matching of the input section

By implementing a conservative constant Q curve of 1.2 to the smith chart and overlap the lines of the components which is also a procedure for gaining a broader bandwidth, seen in figure 5.30. The final circuit for the input section is generated by the smith chart tool seen in figure 5.31 with its' corresponding component values and the response of implementing this is seen in figure 5.32

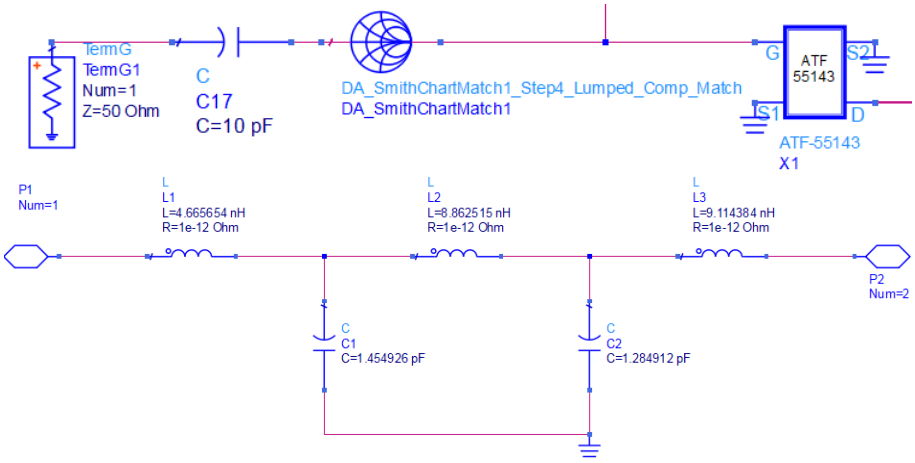

Figure 5.31: Component values for the input matching

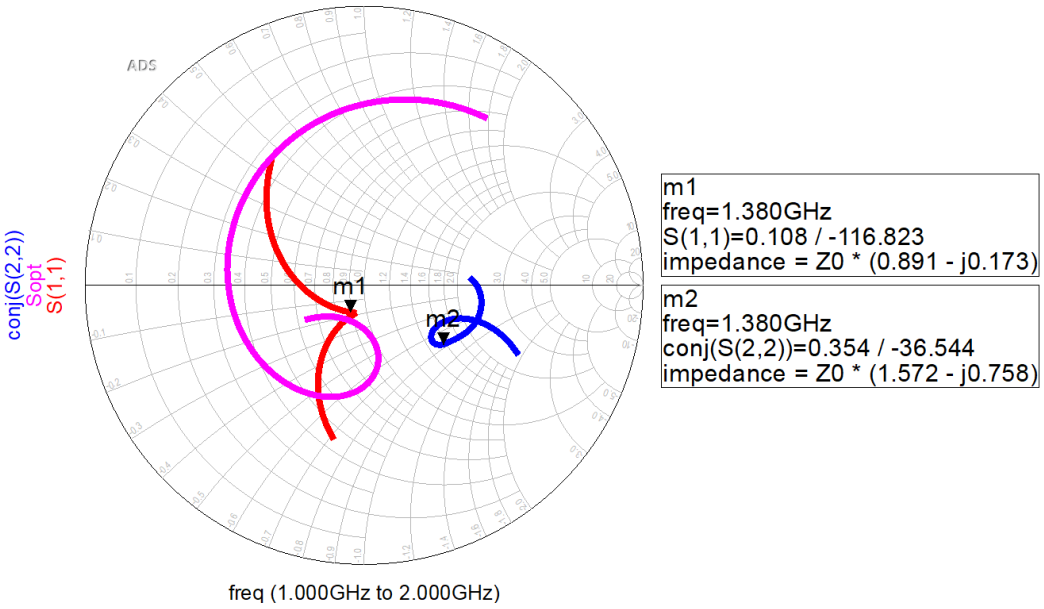

Figure 5.32: S-Parameters after input matching implementation

A similar approach to the output section was done as with the input section, but here simultaneous conjugate match is used as the source impedance. Figure 5.32 shows the matching the conjugated S_{22} value which was taken for smith chart matching.

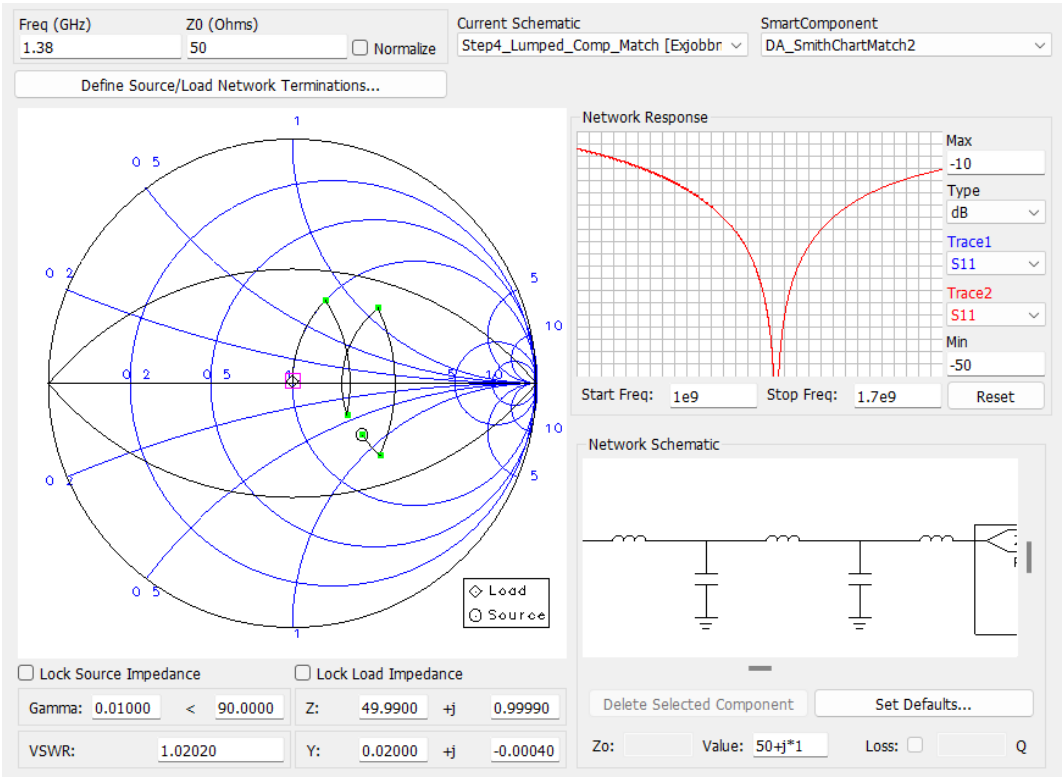

Figure 5.33: Smith chart matching of the output section

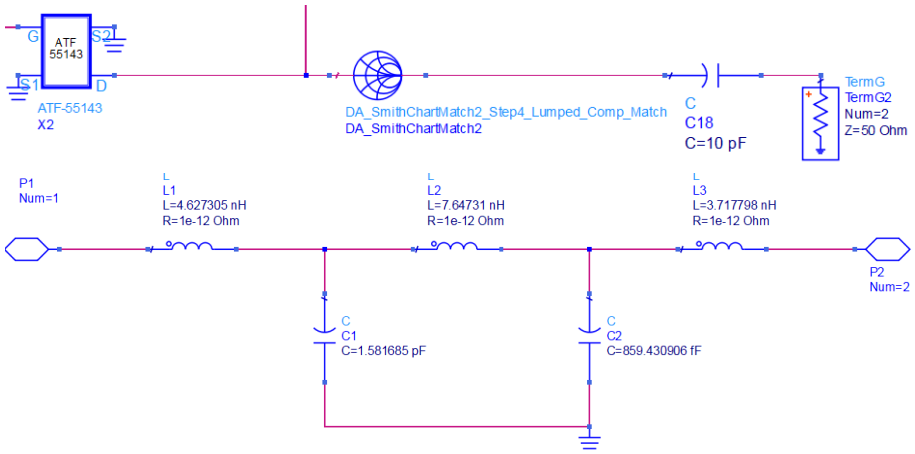

Figure 5.34: Component values for the output matching

A similar circuit was done for the output section seen in figure 5.34 by the values given from the smith chart in 5.33, here an even lower Q value of 0.8 could be used for an even broader match. The complete response for the whole network showed acceptable response for both S_{11} and S_{22} below -10dB with a complete bandwidth of ≈700MHz below -10dB. The overall response is within target in the upper frequency band but S_{22} is about 5dB of target of -15dB in the lower band seen in figure 5.36, moreover is the noise also a to high at this frequency band from figure 5.37

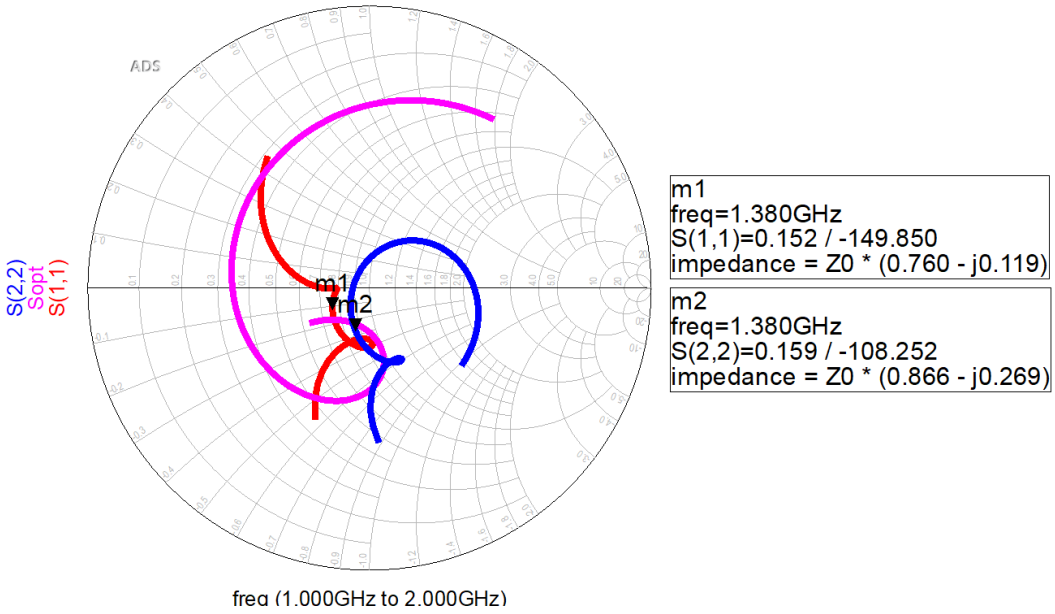

Figure 5.35: Smith chart of input and output S-Paramters after matching implementation

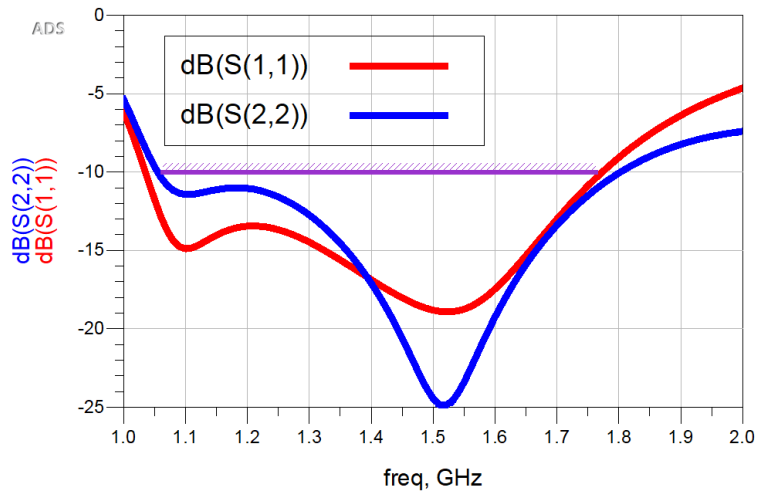

Figure 5.36: Returnloss of implemented matching circuit

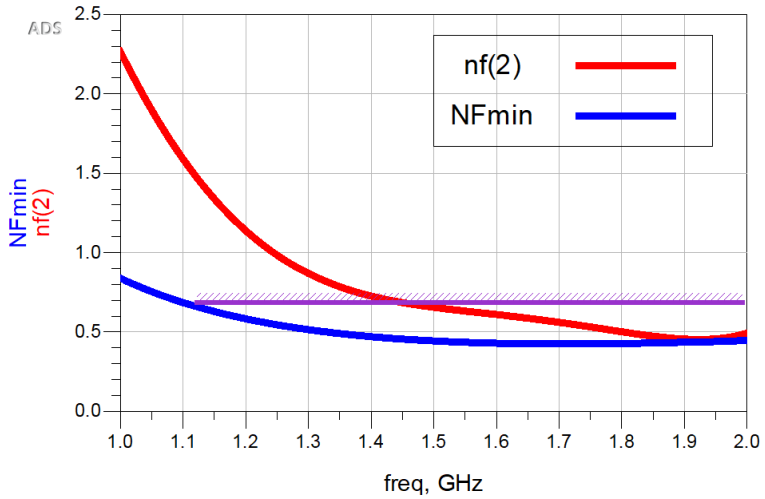

Figure 5.37: Noise for complete network after matching

As a final step the ADS optimetrics tool was used to further fine tune the matching for a better overall response. Goals were set on S_{11},S_{22},$nf(2)$ and the stability factor for a return loss better than -20dB, noise below 0.8dB and stability over the whole frequency band over 1.05. The result showed that the fine tuning improved the performance of all the above mentioned parameters, table 5.4 shows the values before and after tuning. Figure 5.38 demonstrates a return loss of -20dB over the whole bandwidth with an even better response at the bands of interest. The noise is also improved by about 0.5dB better in the lower band, figure 5.39. It should be noted that up to this point only ideal components has been used and is something that has to be taken into consideration for further steps.

Table 5.4: Tuned Matching network components

	Smith chart matching values	Tuned ADS tuning values
Input		
C2	1.92 pF	2.13 pF
C3	1.25 pF	1.27 pF
L1	6.69 nH	7.51 nH
L2	12.48 nH	11.05 nH
L3	7.54 nH	1.5 nH
Output		
C10	1.45 pF	1.48 pF
C11	1.51 pF	1.89 pF
L9	2.42 nH	1.21 nH
L10	9.34 nH	14.15 nH
L11	4.42 nH	8.72 nH

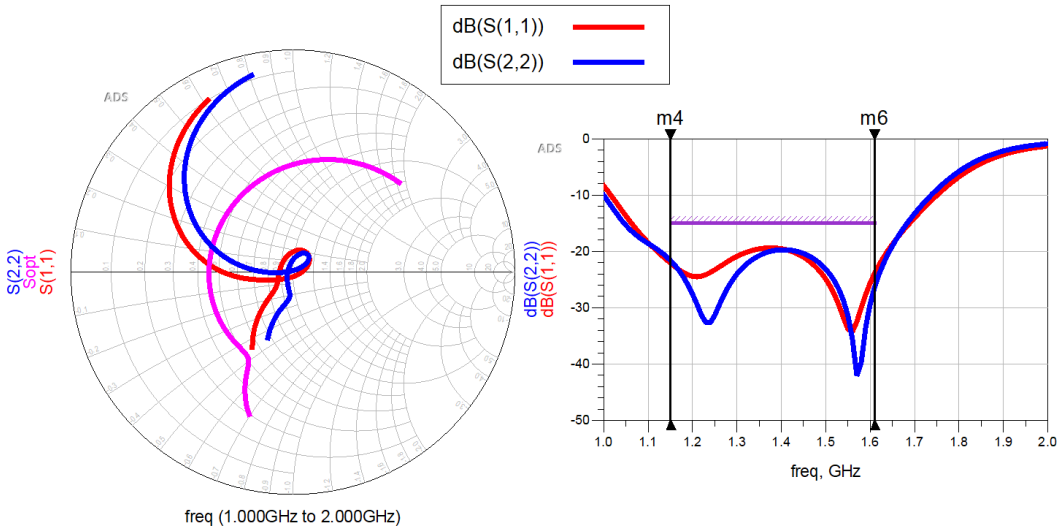

Figure 5.38: Returnloss of implemented matching circuit

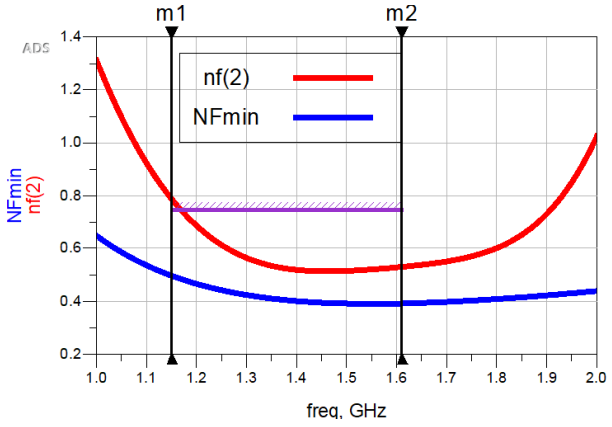

Figure 5.39: Noise for the whole LNA with tuned matching circuit

5.6.6 Microstrip realization

The final step for the LNA design was to realize the network previously determined by utilizing microstrip technology. The losses that microstrip exhibits further increases the noise and lowers the gain which has to be taken into consideration when doing the design, moreover it also effects the matching so further tuning will have to be made as a conclusion.

Firstly, by looking at the given footprint of the transistor seen in figure **??**, the bias network could be constructed above the footprint with the correct dimensions and duplicated to support the second stage transistor. Feed lines were then constructed too both of the inputs of these. Initially, the the matching network components were kept ideal for the tuning, were the idea was to determine the final valued non ideal components afterwards to combat noise and gain deterioration's. Because of the size of the now constructed schematic circuit, it cannot be placed as one picture, the complete schematic network can instead be found in the appendix section. The proposed complete microstrip realization is seen in figure 5.40

Figure 5.40: Microstrip realization of LNA

The lengths for the matching sections on the input side was made as short as possible to minimize noise contributions. For the output, it was seen that increasing the length of the first stub greatly improved the dual matching performance, but it was also noted that the bandwidth of both the upper and lower GNSS frequency bands exhibited a more narrow band than previous tests. The overall noise contribution was also high at approximately 2dB on the upper frequency band. In an effort to try and combat this behaviour, one technique used from [25] utilized two series connected inductive and capacitive grounded stubs. This was to try and suppress the in influence of gate-source capacitance and to suppress the Miller effect of the hybrid gate to drain capacitance [25]. This was to be implemented on the input and output section of the LNA. Because these capacitance's previously mentioned is relatively low, conservative low valued components where proposed as a starting point, where manual tuning for optimum performance were followed. The updated microstrip circuit can be seen in figure 5.41 and the performance of the realized microstrip design can be seen in figure 5.42.

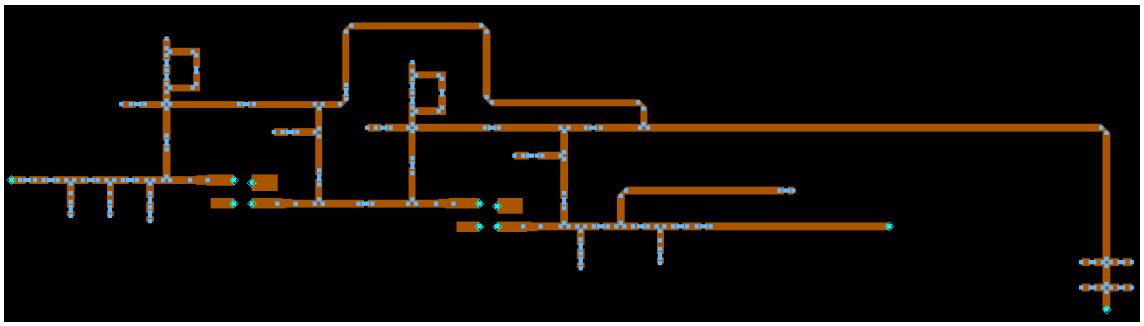

Figure 5.41: Microstrip realization of LNA with third stub implemented on input and output stage

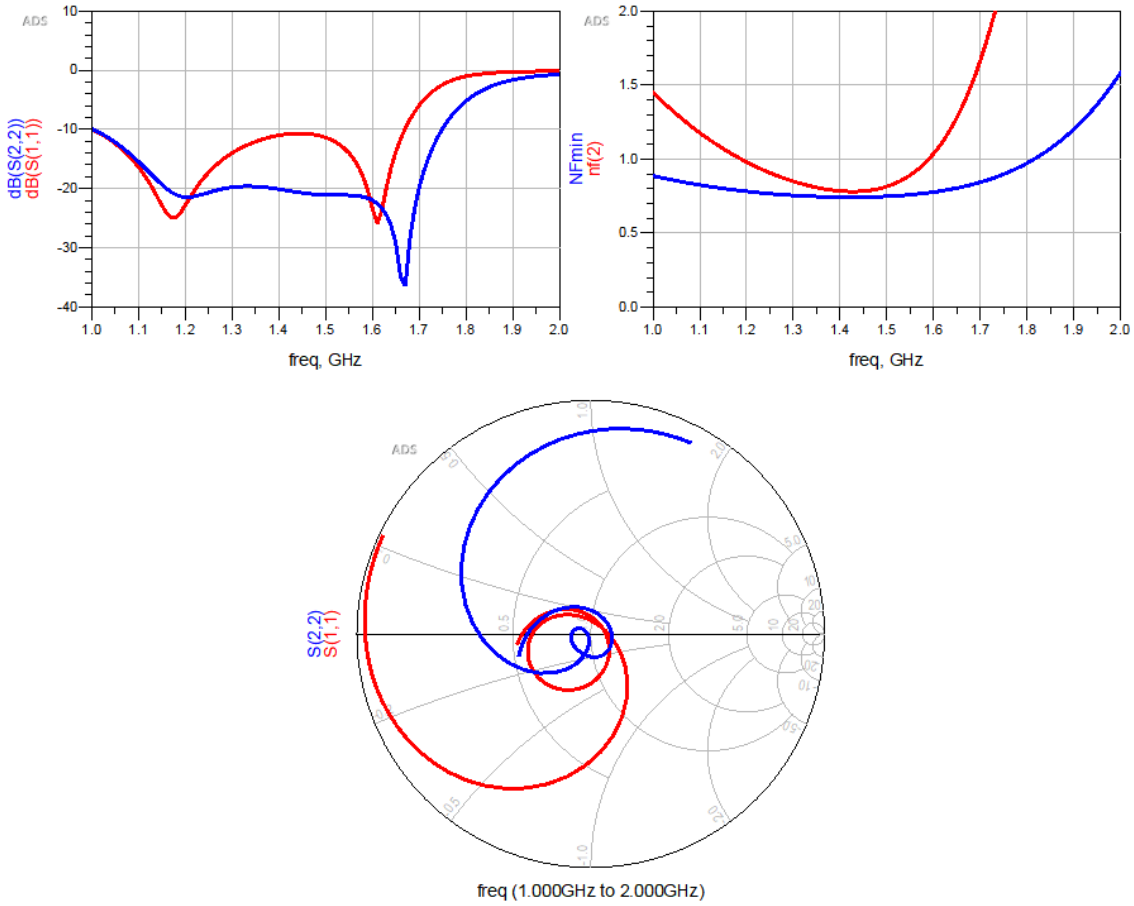

Figure 5.42: Performance of microstrip realized LNA

5.7 Momentum Microwave Simulation

As for many circuits and especially for RF designs, a key consideration is to make EM wave simulation of the traces for a more accurate performance of the circuit. This type of simulations utilize the proposed layout of the microstrip traces, where later a co-simulation is performed by implementing the passive and active lumped

components afterwards. To get accurate results from the EM simulation it is of importance to increase the mesh distribution to approximately 150 cells per wavelength. The substrate where then set to the proposed FR4 with ϵ_r of 4.05 and a thickness of 0.23mm seen in figure 5.44. The trace thickness where set to as from the manufacturer description to 0.018mm.

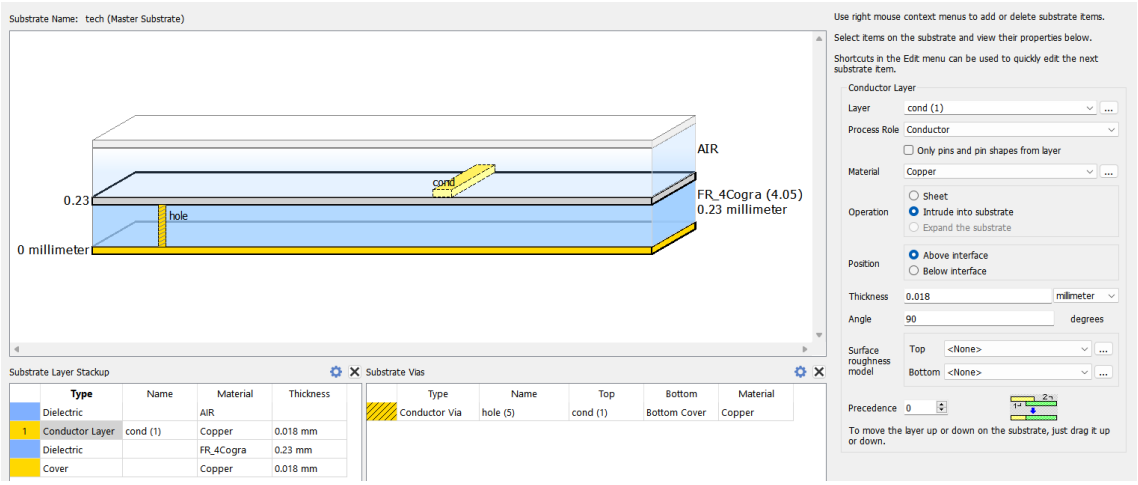

Figure 5.43: Substrate for microstrip circuit

Performing the co-simulation with the same component values previously determined showed the circuit exhibit similar characteristics with slight variations to the output section S_{22}, the noise contribution where similar as well seen in figure 5.45. In an effort to combat the slight changes, a second optimization was performed to the same parameters as previous.

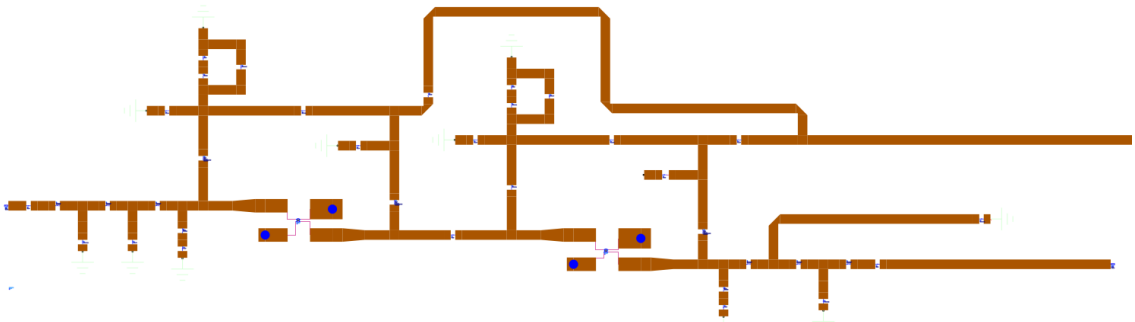

Figure 5.44: CO-simulation of EM wave momentum circuit

The components where now implemented as non ideal, which means the LNA exhibits a more realistic performance, and show a more accurate performance to the noise, where the most influential components to consider where the inductors. The highest noise contribution is known to be located on the input section of the LNA, and it is therefor of great importance to take this section into consideration. It is also known that the RF choke on the input place a crucial role and while keeping this connected in serial with an resistor was seen to present with a much higher noise floor then previously exhibited. The quick solution for this was not only to tune the

input and output matching networks, but also by lowering the gate resistance values, by doing this it was seen to give great improvements to the overall system, the finalized performance of the LNA can be seen in figure 5.47 and the final component values list can be seen in table **??**

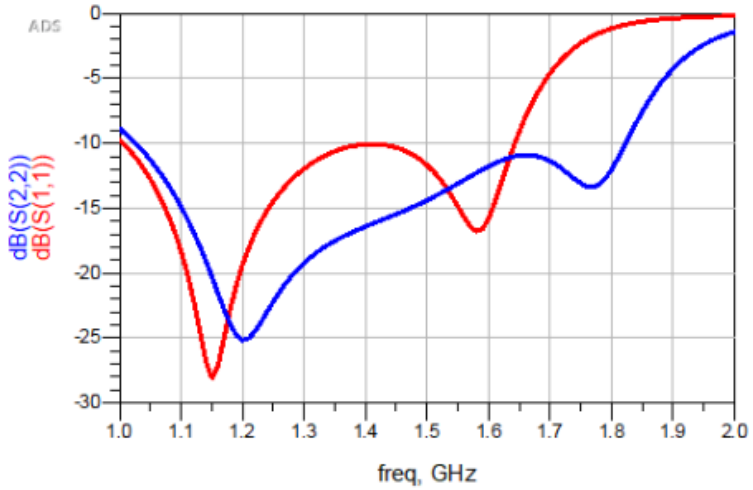

Figure 5.45: Performance before optimization tune

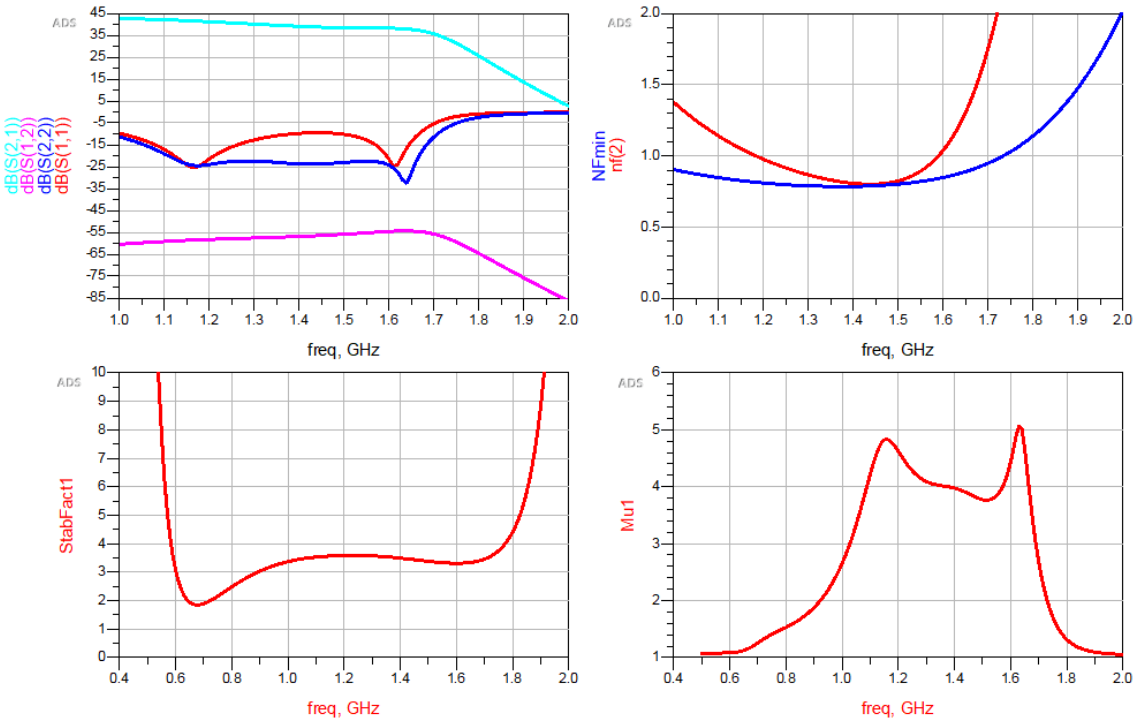

Figure 5.46: Performance after optimization tune

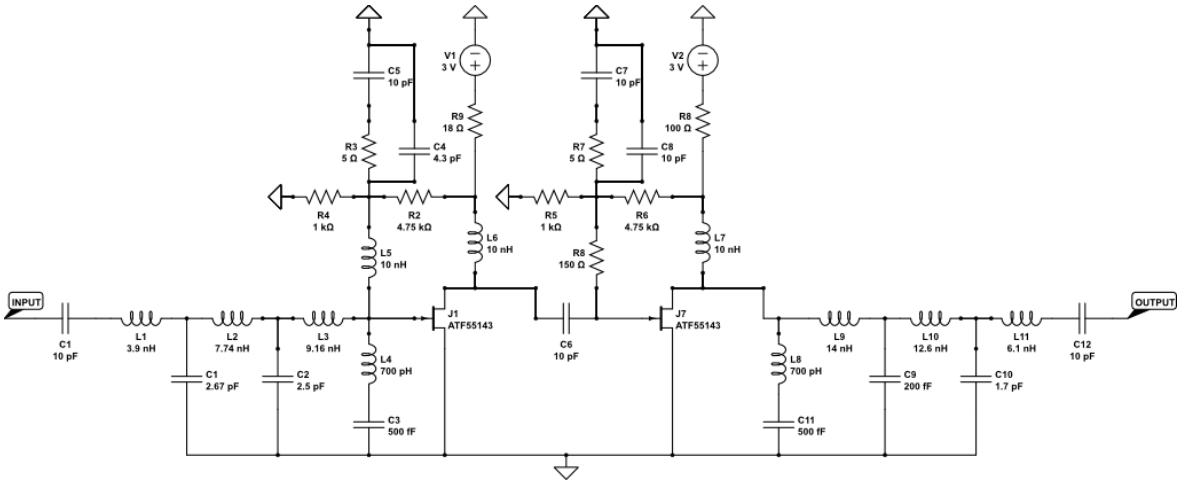

Figure 5.47: Complete LNA circuit

6
Layout generation and assembly

This chapter concludes the steps taken to merge all the elements previously discussed and finalize them to make a complete circuit. Some of the design requirements used for this is determined from manufacturer COGRA and is used here throughout.

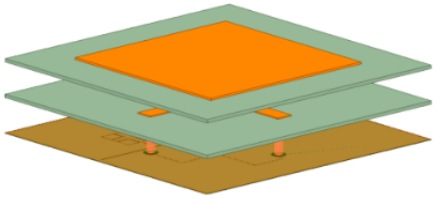

Figure 6.1: Complete visualization of the antenna.

6.1 Combining Elements

All elements previously discussed and determined would be merged and interconnected. This was to be done in ADS due to the previous layout generation of the flow network and LNA design had been done in ADS. Although the circuits were minimized as much as possible, aligning it correctly was not straight forward at first. The four supply probes that reached the capacitive elements in the middle of the antenna were fixed and could not be moved to retain the properties of the antenna. To make it easier to visualize and finally determine the location of the feed network, it was initially implemented to HFSS. There are techniques in ADS using reference points, but by doing this first technique, a complete EM wave simulation can also be performed to verify performance. The lengths from the four starting points in the feed network also needed to have the same lengths for each probe, since a length deviation in any of these would give an undesired phase shift. But at the same time, the lengths also needed to be minimized to keep the losses as low as possible. The final location of the feed network can be seen in the figure 6.2.

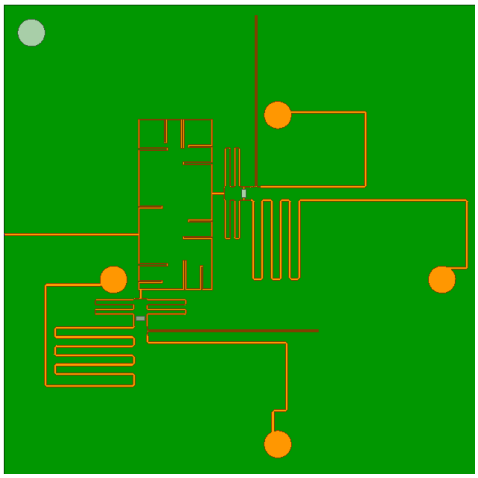

Figure 6.2: Location of feed network with added lengths to probes (HFSS)

The microstrip traces of the LNA could also be implemented in the same way for visualization purposes, but because of the active and passive components would an EM simulation in HFSS be possible. The proposed layout was determined to as close as possible to the input section of the rat race, see figure 6.3.

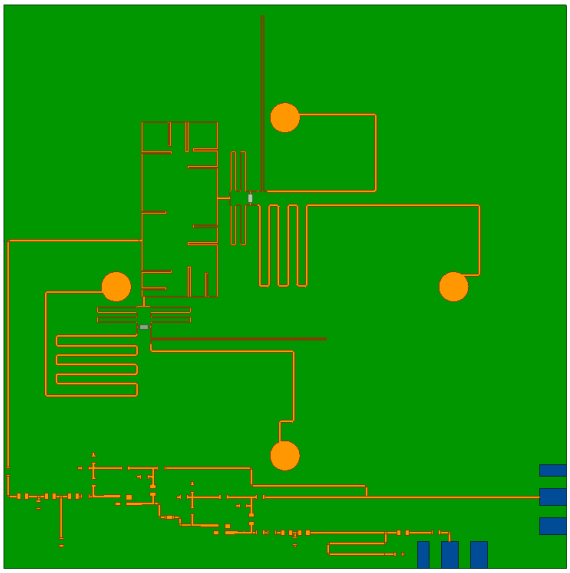

Figure 6.3: Location of feed network and LNA (HFSS)

The implementation of both of the elements on the FR4 substrate shows the size is sufficient for both of the elements, while keeping the same characteristics as before. Likewise could this now easily be moved to ADS to generate the final layout seen in figure 6.4

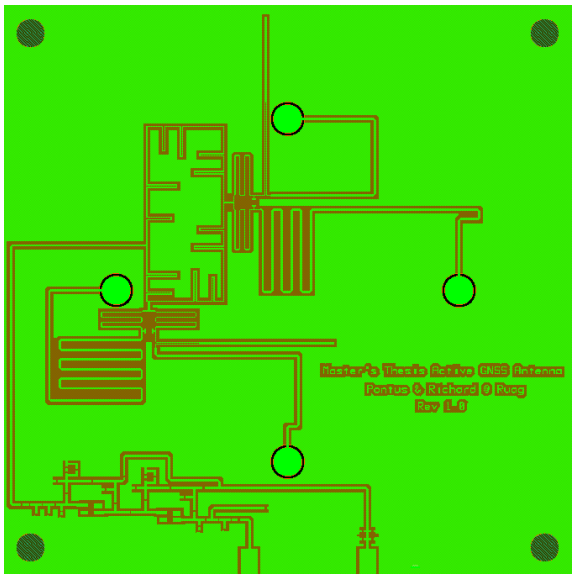

Figure 6.4: ADS layout implementation

The height of the substrate between ground and conductors has as previously described been set to 0.23mm, while this is sufficient for the conductors would this not be feasible for fabrication and would give a very fragile design. Instead the manufacturer makes a 4 layer PCB resulting in a thickness of approximately 1.6mm. The traces grounding layer will still be the first layer below the traces of 0.23mm but plated via holes from the top conductor to the bottom layer ground will have to be implemented to achieve the grounding effect, this is more commonly known as via stitching. Moreover vias is also commonly used as a form of shielding, when working with RF designs a common problem if traces are close to each other is crosstalk and EM interference in the conductors. To minimize this, one can use via holes placed in one or more rows alongside the conductor traces, this is more commonly referred to as via shielding. By implementing the latter, would it simultaneously help with the stitching. It should also be mentioned here that the decision was made to keep the top grounding layer at 0.5mm from the traces to further benefit the shielding. The complete circuit with vias implemented is seen in figure ref 6.5, the plated holes are black in the figure and the corner holes is for structural purposes and is therefor not plated.

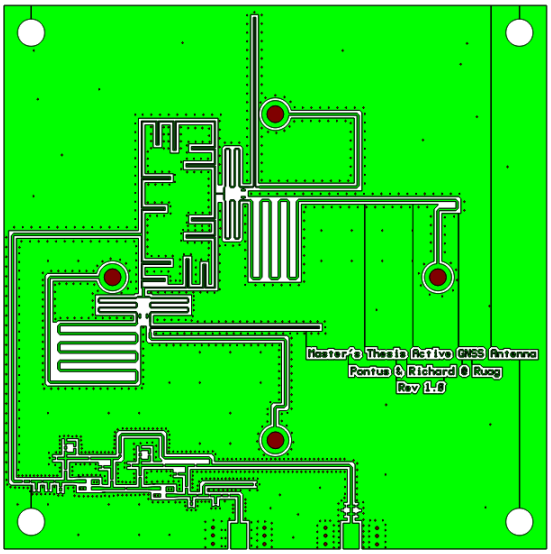

Figure 6.5: Complete layout of bottom layer for fabrication

6.2 Antenna fabrication

The complete antenna unit is constructed by three layers, where the latter discussed in previous section forms the bottom layer. The remaining middle and top layer will keep the same thickness as the bottom layer, but the grounding for the antenna is constructed from the bottom layer. Therefore the patch elements for the middle and top surface only needs to be constructed with the substrate of 1.6mm. The substrate should keep the same dimension as the bottom layer with the microstrip patches printed above. Figure 6.6 shows the layout sent to manufacturer with drill holes.

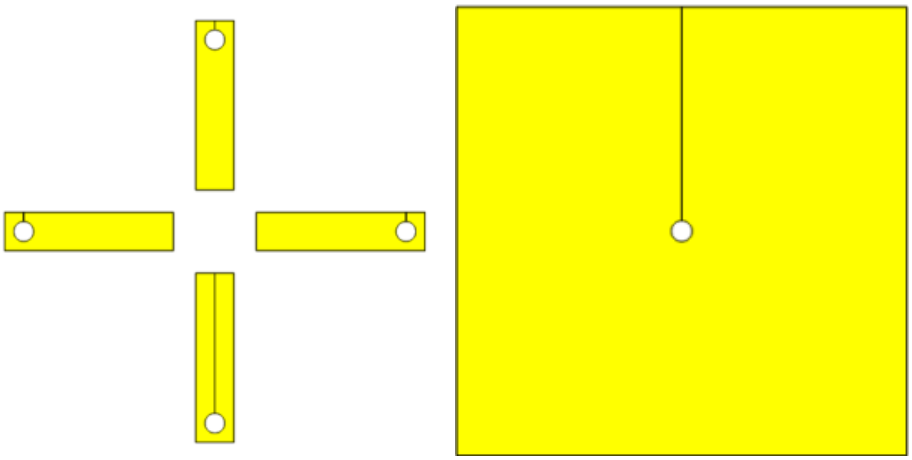

Figure 6.6: Middle antenna layer (left), top antenna layer (right)

6.3 Assembly

Upon arrival of the PCB.s, tests of the traces were made to confirm that the manufacturing had been done correctly. Next the assembly of the LNA began by soldering all the chosen passive and active components. Here the voltage was also tested at different locations, especially around the drain and gate of the transistors to establish the correct bias point. The complete circuit with soldered components can be seen in figure 6.7.

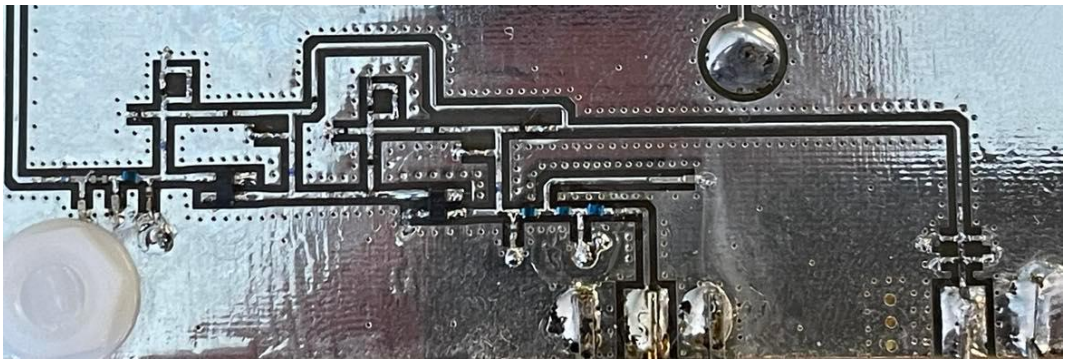

Figure 6.7: Finalized LNA

For the antenna, the copper rods were cut to the correct size and soldered on to the PCB and the middle antenna sheet, similarly with the middle grounded rod. Lastly the PVC support rods for every corner was measured to the correct lengths and rigged to the antenna. The fully assembled antenna is seen in figure 6.8,6.9 and 6.10.

Figure 6.8: Assembled antenna top view

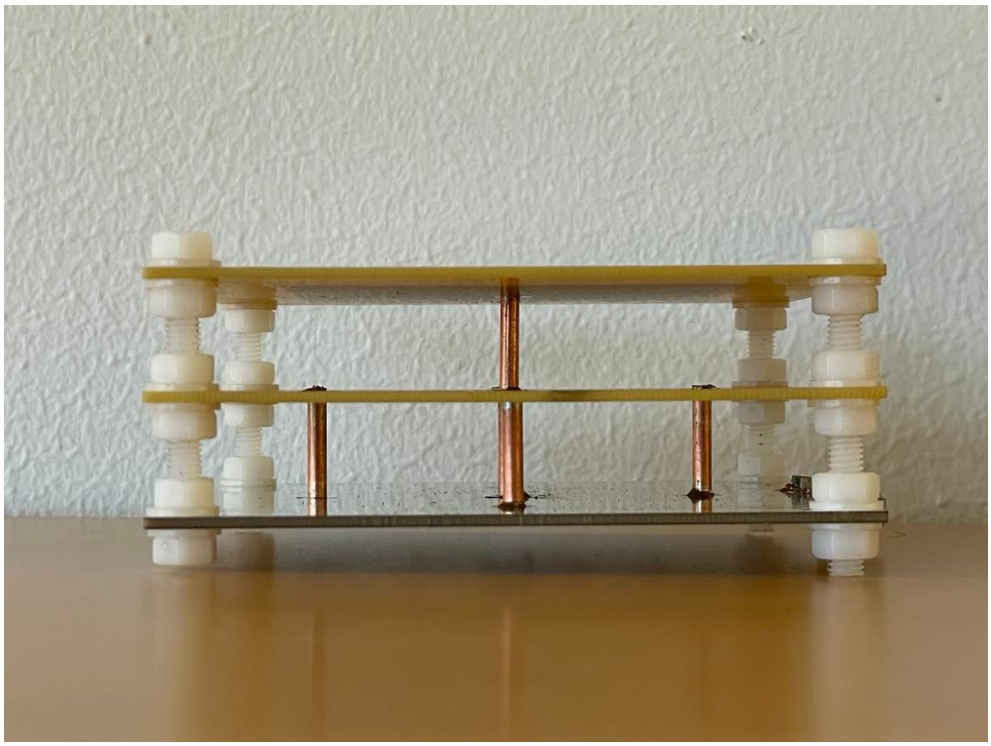

Figure 6.9: Assembled antenna side view

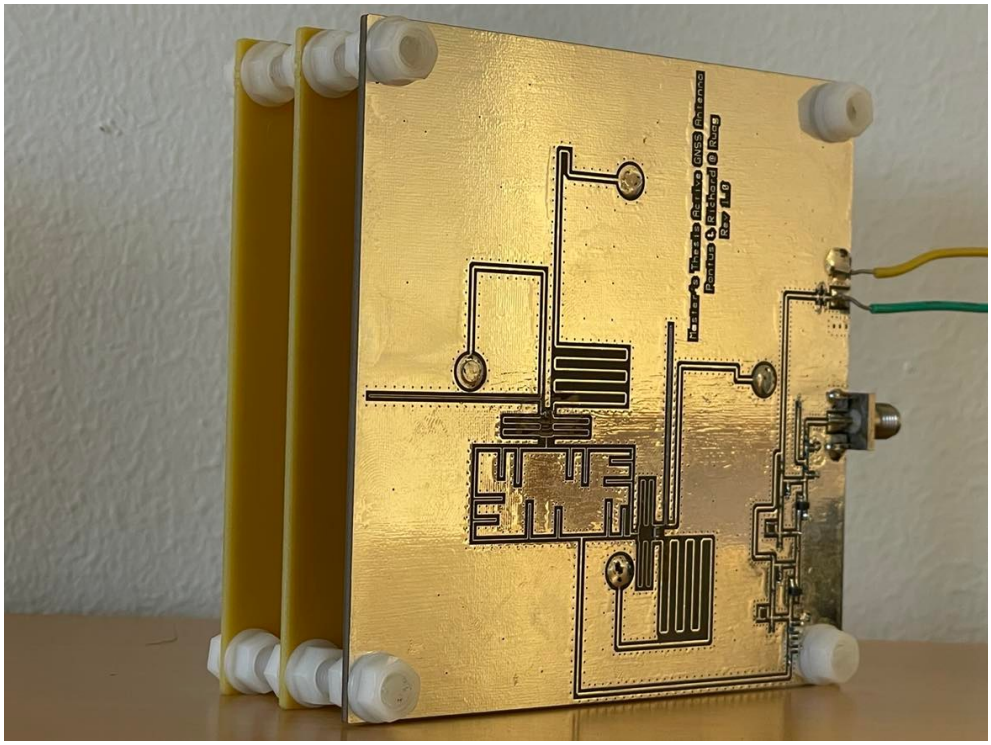

Figure 6.10: Assembled antenna bottom view

7
Results

The measurements made on the physical circuit are divided into three different sections where a VNA analyzer has been utilized in order to measure the scattering parameters of the antenna and LNA separately. Measurements has also been made in an anechoic chamber and finally noise measurements has been made on the LNA circuit to measure the noise figure.

7.1 LNA measurment with VNA

The first measurements were made by separating the feeding network and antenna from the LNA circuit. The measurements were made on the input and output of the LNA and showed that there were two dips in both S_{11} and S_{22} for L1 and L5 as shown in simulations, although by a large offset in frequency domain.

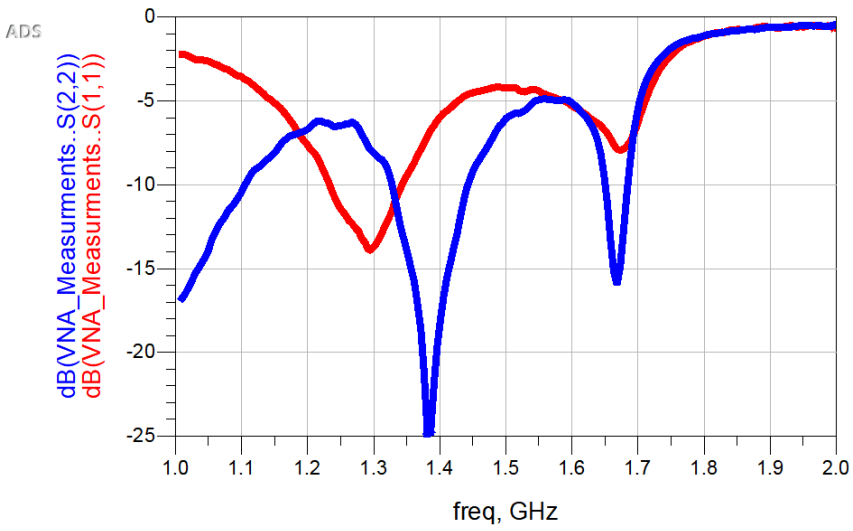

Figure 7.1: First VNA measurements of LNA circuit. S_{11} and S_{22}.

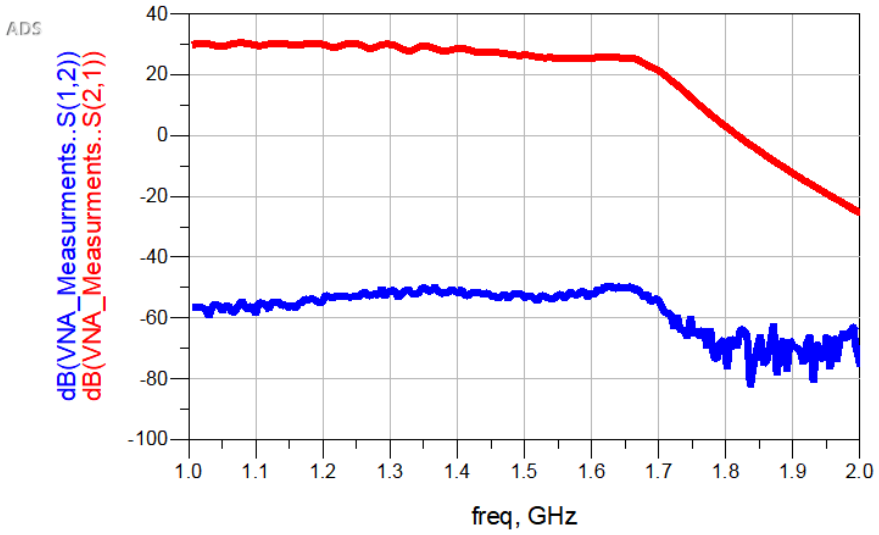

Figure 7.2: First VNA measurements of LNA circuit, S_{12} and S_{21}.

In most microwave circuits tuning is always needed after physically realizing a simulated circuit. The shift in frequency most likely depends on the shifted ϵ_r in the FR4 substrate as mentioned in 5.4.1, since calculations were made on a dielectric constant of 4.6 while the physical substrate has an ϵ_r ≈4.05-4.17 in the frequency range of 1-2 GHz. A total of nine iterations of new simulations and soldering were made in order to realize the circuit with the Scattering parameters shown in figure 7.4. By using an FEM simulation in ADS with a dielectric constant of 4.05 all the components present in the input and output feeding networks have been changed to their proper values for a shift in ϵ_r.

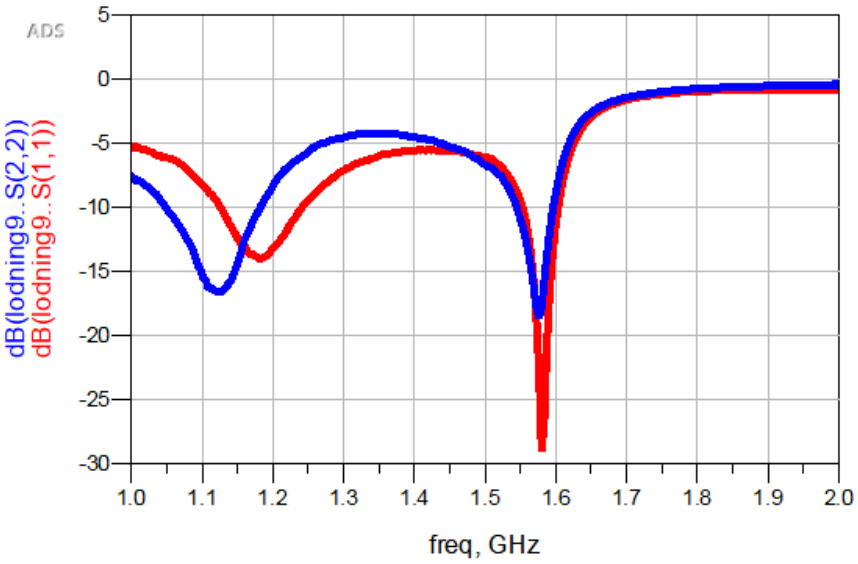

Figure 7.3: VNA measurements of LNA circuit after fine tuning components. S_{11} and S_{22}

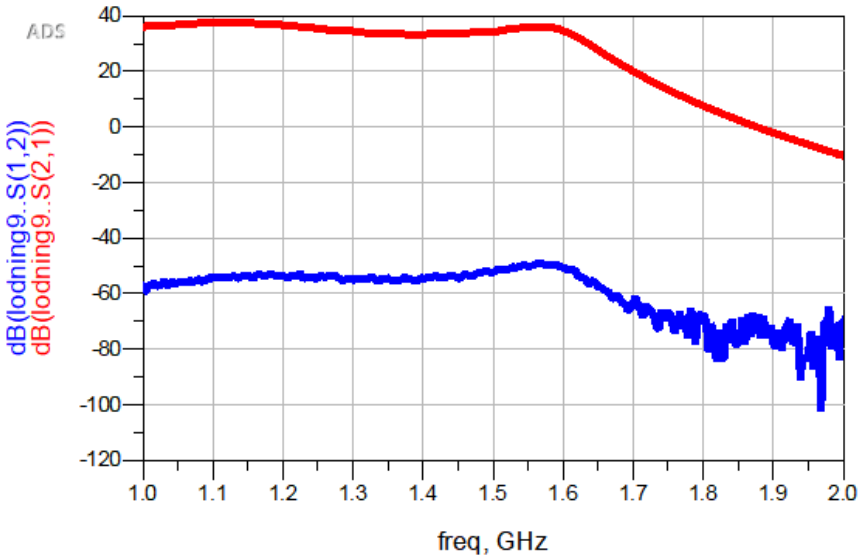

Figure 7.4: VNA measurements of LNA circuit after fine tuning components S_{12} and S_{21}

Table 7.1: Matching network components

	Component values $\epsilon_r = 4.6$	Component values $\epsilon_r = 4.05$
Input		
C2	3.9 pF	3.3 pF
C3	3.9 pF	3.3 pF
C4	1 pF	0.5 pF
L1	2.3 nH	3.1 nH
L2	4.4 nH	5.9 nH
L3	6.8 nH	7.8 nH
L4	0.7 nH	
Output		
C9	1 pF	
C10	2.5 pF	2.2 pF
C11	0.5 pF	0.2 pF
L8	0.7 nH	
L9	12 nH	12.3 nH
L10	9.6 nH	5.75 nH
L11	6.8 nH	5.1 nH

7.2 Noise Measurements

The noise measurements was performed on the isolated LNA circuit. The graph presented in figure 7.5 represents the noise figure when the LNA is connected to a source voltage of 3 V drawing approximately 23 mA. The resulting noise is suf-

ficiently low on the lower frequency band but raises to about 2dB for the upper band.

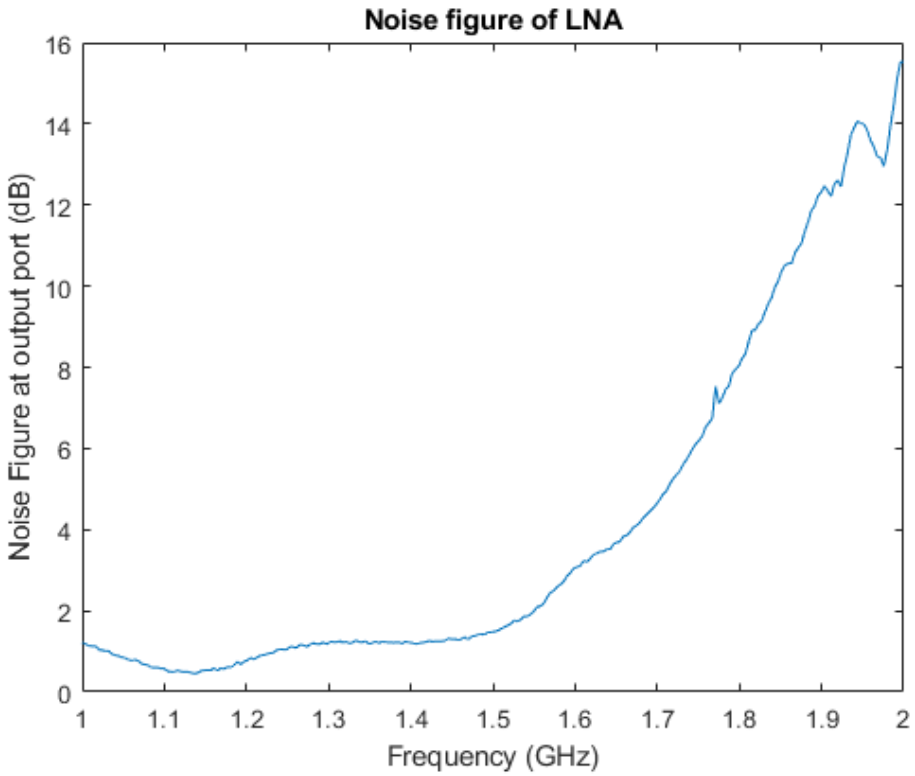

Figure 7.5: Noise measurement of the LNA at the output port (NF(2)).

7.3 Antenna measurements with VNA

A similar approach as with the previous measurements with the LNA was performed for the antenna but isolated from the LNA, this was to determine the impedance bandwidth. The resulting response can be seen in figure 7.6.

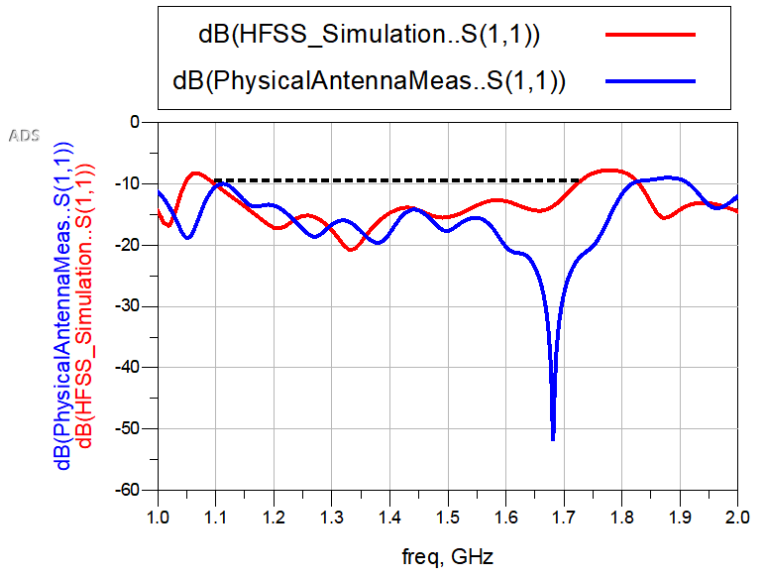

Figure 7.6: Antenna response from VNA measurement

The results concludes that the antenna exhibits similar characteristics as with the simulation from HFSS, apart from a slight frequency shift to the response which can be due to minor variation in the actual permittivity of the substrate used for fabrication, or human error during assembly. But the result shows that the antenna is withing the requirements regarding impedance bandwidth.

7.4 Measurements in an anechoic chamber

The measurements presented in this section are performed in the anechoic chamber at Beyond gravity, where the directivity, gain and axial ratio are measured. The measurements are done for two separate cases: The antenna without the LNA circuit present and the antenna connected to the LNA circuit.

Figure 7.7: Antenna mounted in the anechoic chamber.

Results presented in figures sections 7.4.1 and 7.4.2 are all measured for the same three parameters. Measurements are done at 19 distinct frequency points for 2 separate transmitted polarizations, X and Y (vertical and horizontal). At each frequency point ϕ is swept from 0 to 180 degrees at 2 degree intervals. Phi represents the azimuth angle meaning we start at ϕ=0, at boresight and measure until the antenna is facing away from the transmitter. At each azimuth angle, the antenna is measured at 180 θ angles ranging from 0 to 360 degrees at 2 degree intervals. This in practice is the antenna doing a full revolution around the Z-axis.

Table 7.2: Measured frequencies

f1	1140.0 MHz	f11	1300.0 MHz
f2	1150.0 MHz	f12	1310.0 MHz
f3	1164.0 MHz	f13	1540.0 MHz
f4	1176.5 MHz	f14	1550.0 MHz
f5	1189 MHz	f15	1559.0 MHz
f6	1207.1 MHz	f16	1575.4 MHz
f7	1214.0 MHz	f17	1591.0 MHz
f8	1240.0 MHz	f18	1600 MHz
f9	1260.0 MHz	f19	1610 MHz
f10	1278.5 MHz		

7.4.1 Measurements without amplifier

Figures 7.8, 7.9 and 7.10 measured the directivity of the antenna, see equation 2.9 over θ angles from 0-360 degrees. The co-polarization can be seen in blue and the cross polarization is seen in red.

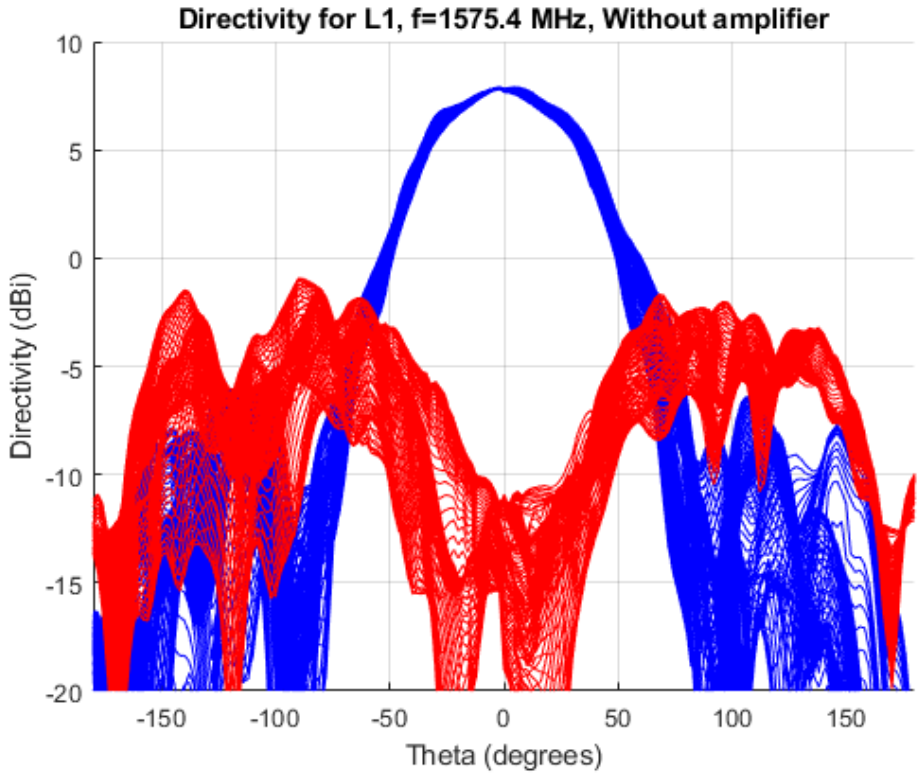

Figure 7.8: Directivity for L1, Blue: Co-pol (RHCP), Red: Cross-pol (LHCP).

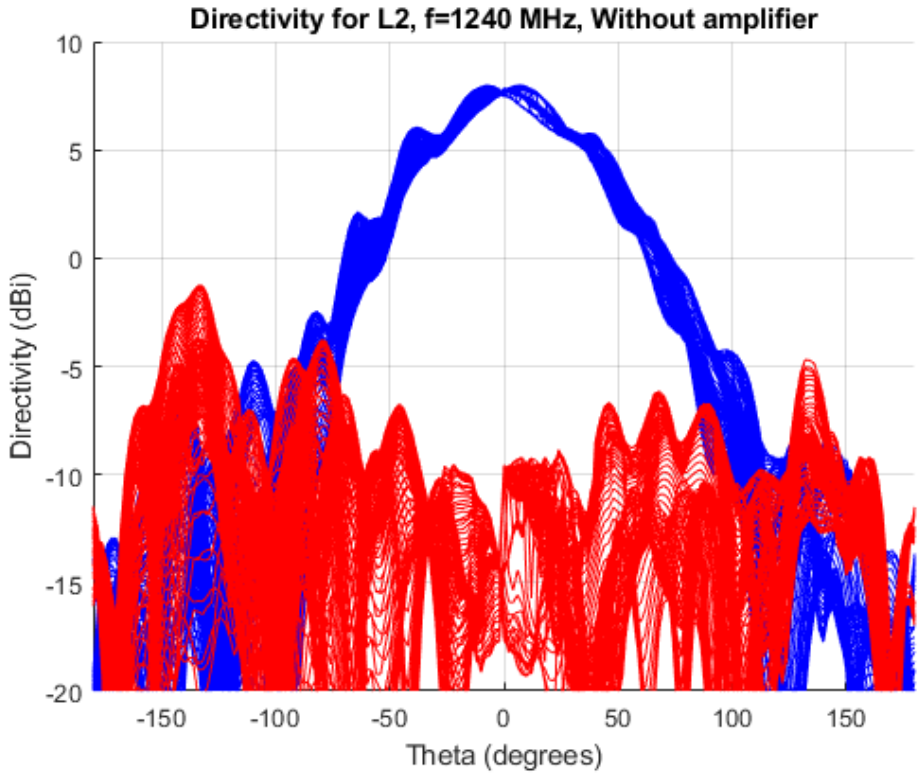

Figure 7.9: Directivity for L2, Blue: Co-pol (RHCP), Red: Cross-pol (LHCP).

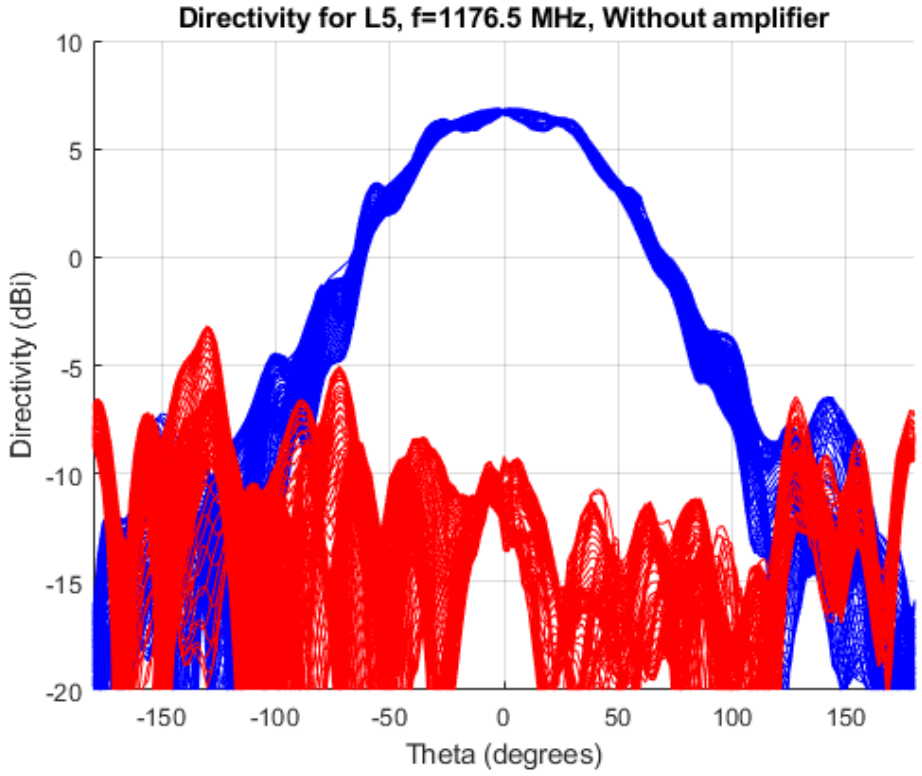

Figure 7.10: Directivity for L5, Blue: Co-pol (RHCP), Red: Cross-pol (LHCP).

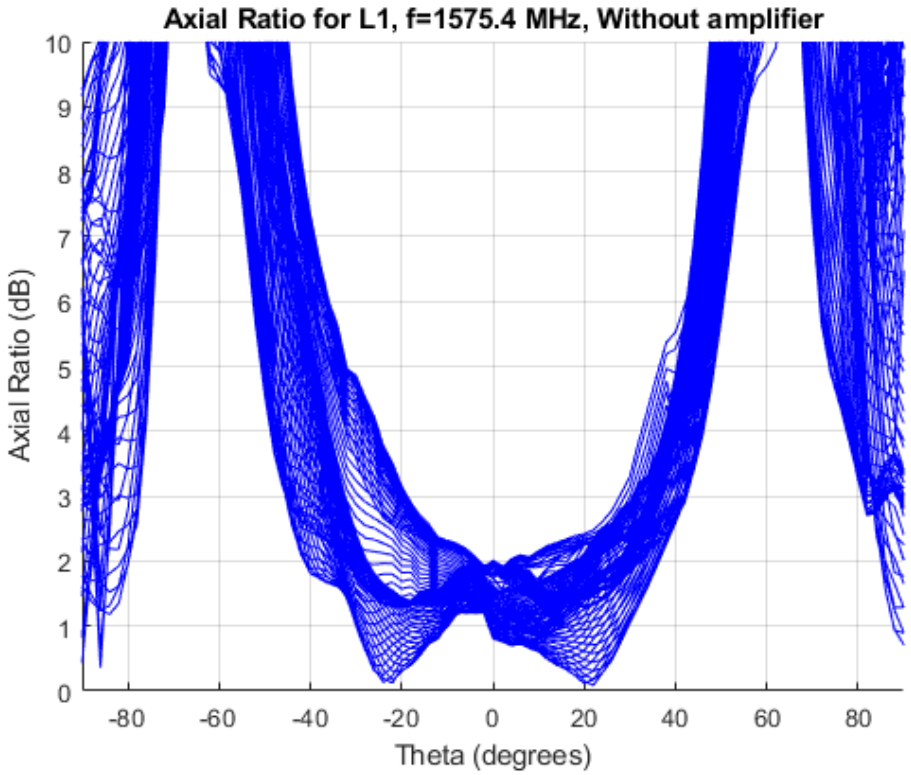

Figure 7.11: Axial Ratio for L1, Blue: Co-pol (RHCP), Red: Cross-pol (LHCP).

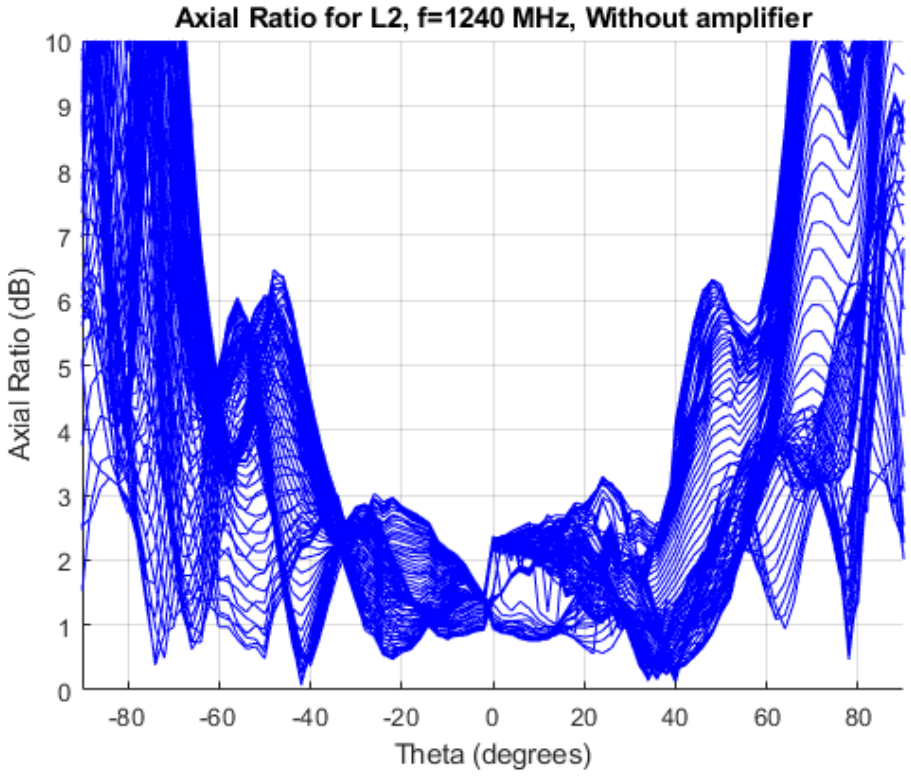

Figure 7.12: Axial Ratio for L2, Blue: Co-pol (RHCP), Red: Cross-pol (LHCP).

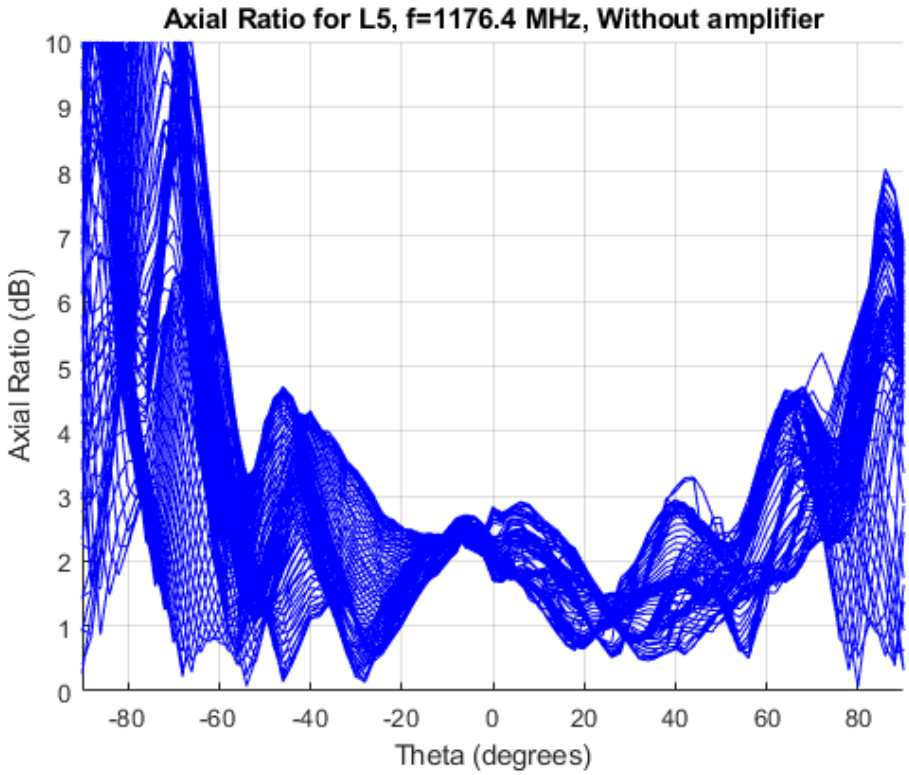

Figure 7.13: Axial Ratio for L5, Blue: Co-pol (RHCP), Red: Cross-pol (LHCP).

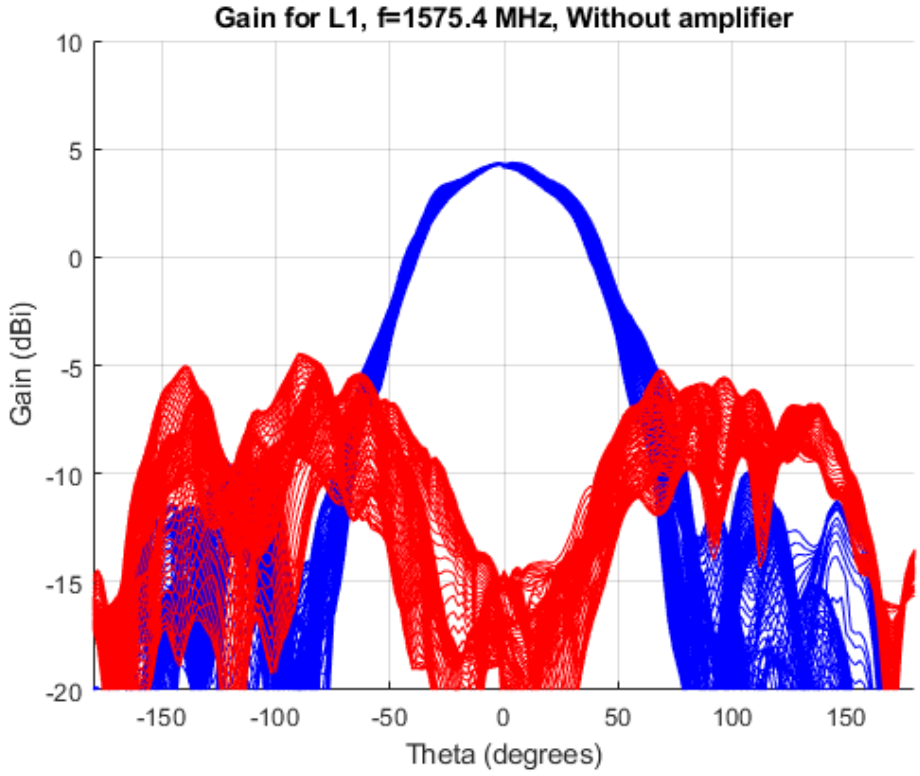

Figure 7.14: Actual gain for L1, Blue: Co-pol (RHCP), Red: Cross-pol (LHCP).

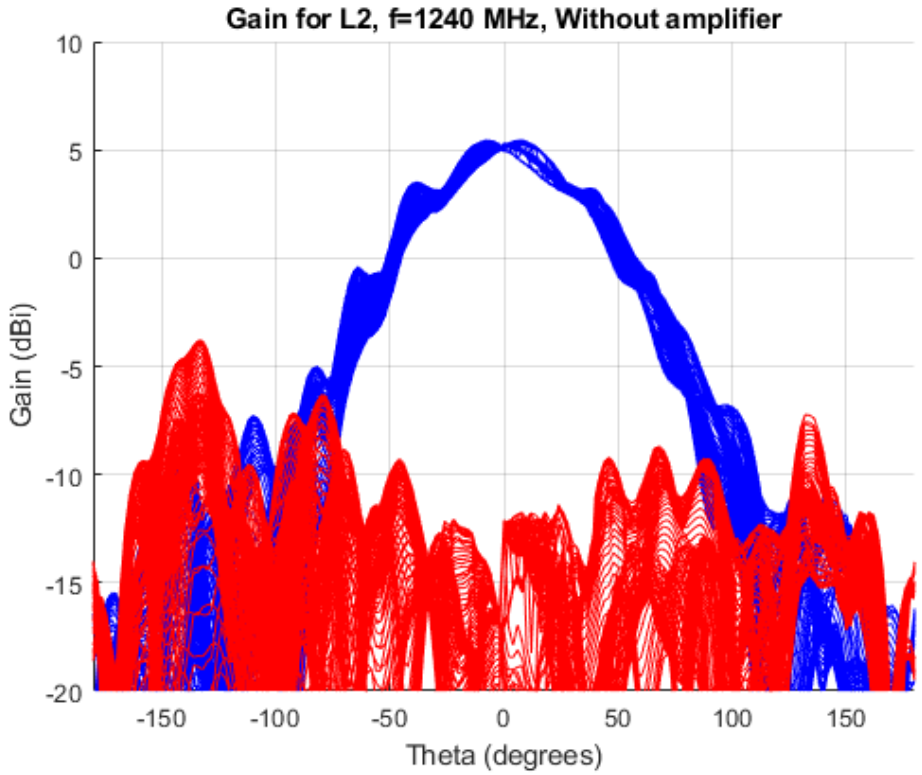

Figure 7.15: Actual gain for L2, Blue: Co-pol (RHCP), Red: Cross-pol (LHCP).

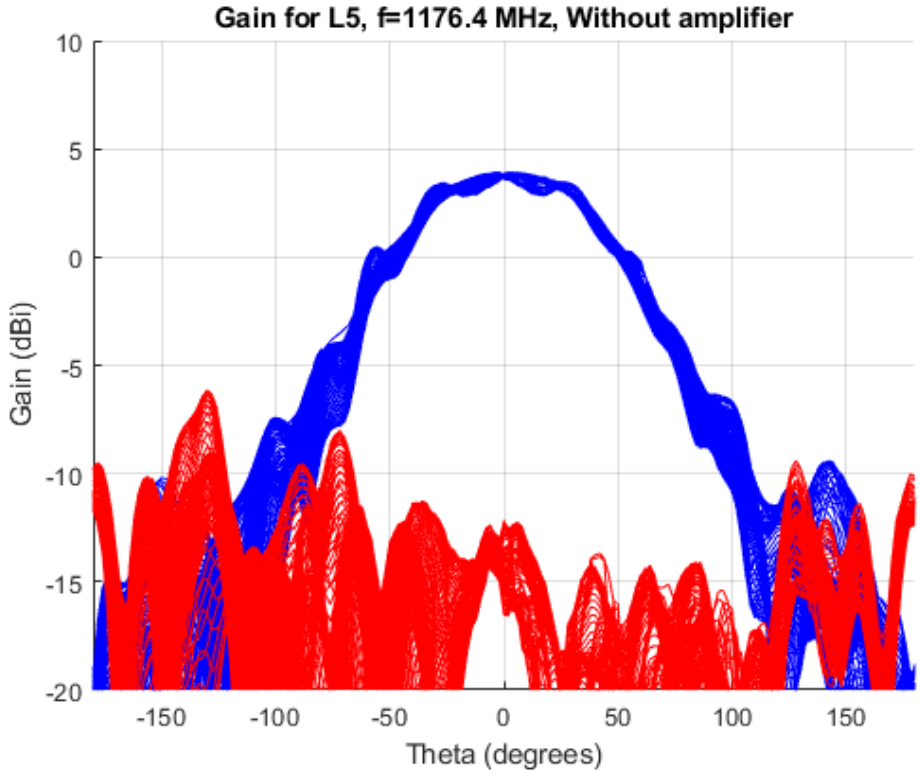

Figure 7.16: Actual gain for L5, Blue: Co-pol (RHCP), Red: Cross-pol (LHCP).

7.4.2 Measurements with LNA circuit

The measurements performed in this section have been done over the exact same frequency points, theta and phi sweeps as the ones made in section 7.4.1, but in these measurements the antenna is connected to the LNA circuit.

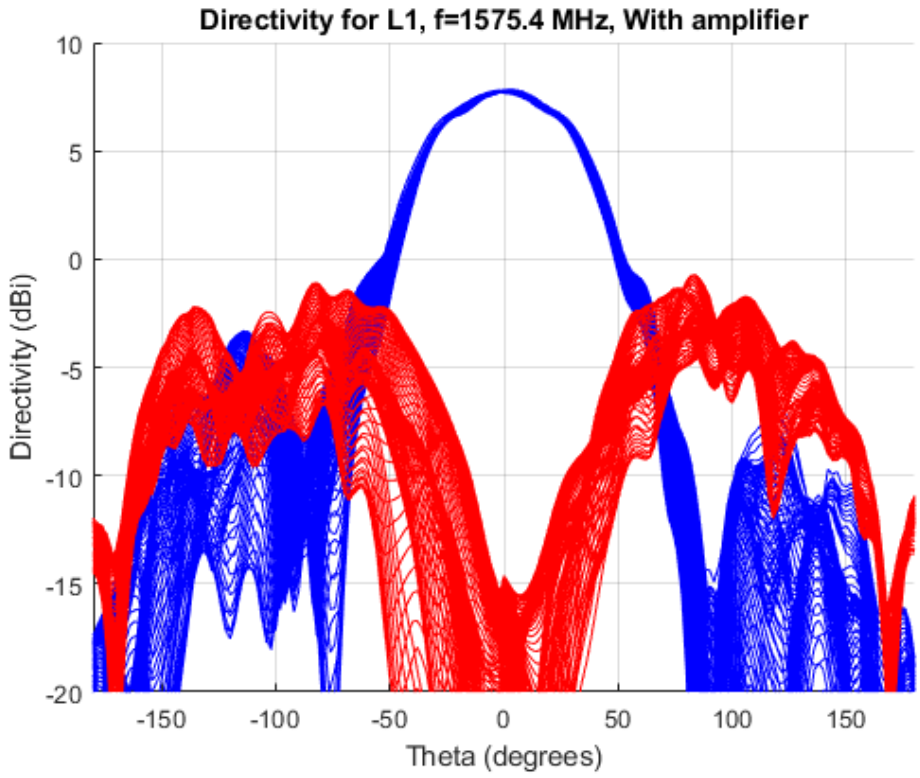

Figure 7.17: Directivity for L1, Blue: Co-pol (RHCP), Red: Cross-pol (LHCP).

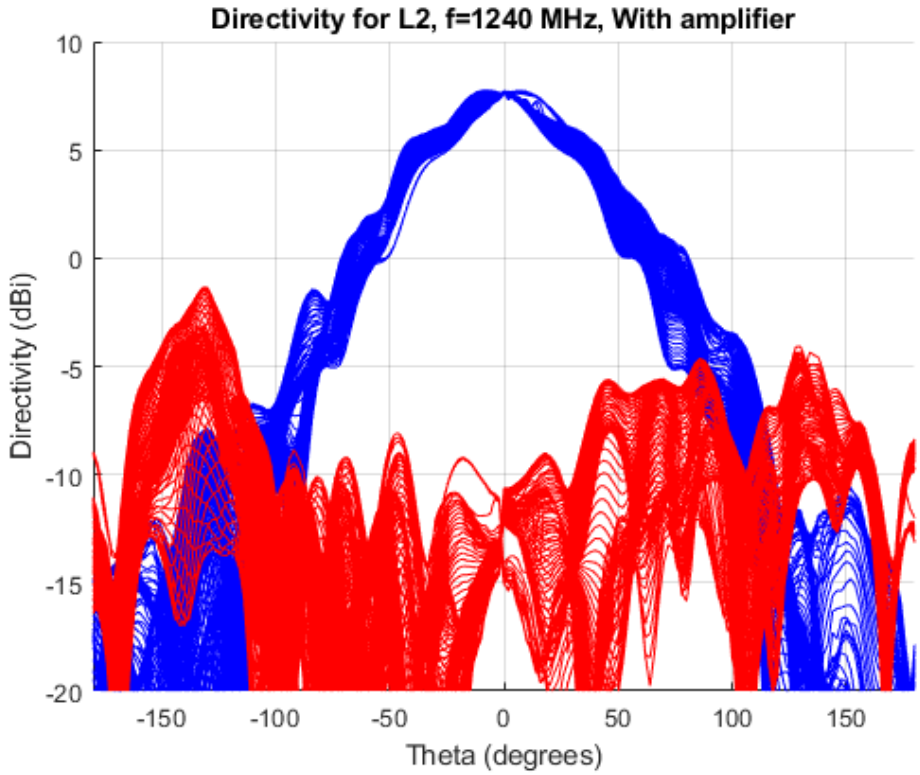

Figure 7.18: Directivity for L2, Blue: Co-pol (RHCP), Red: Cross-pol (LHCP).

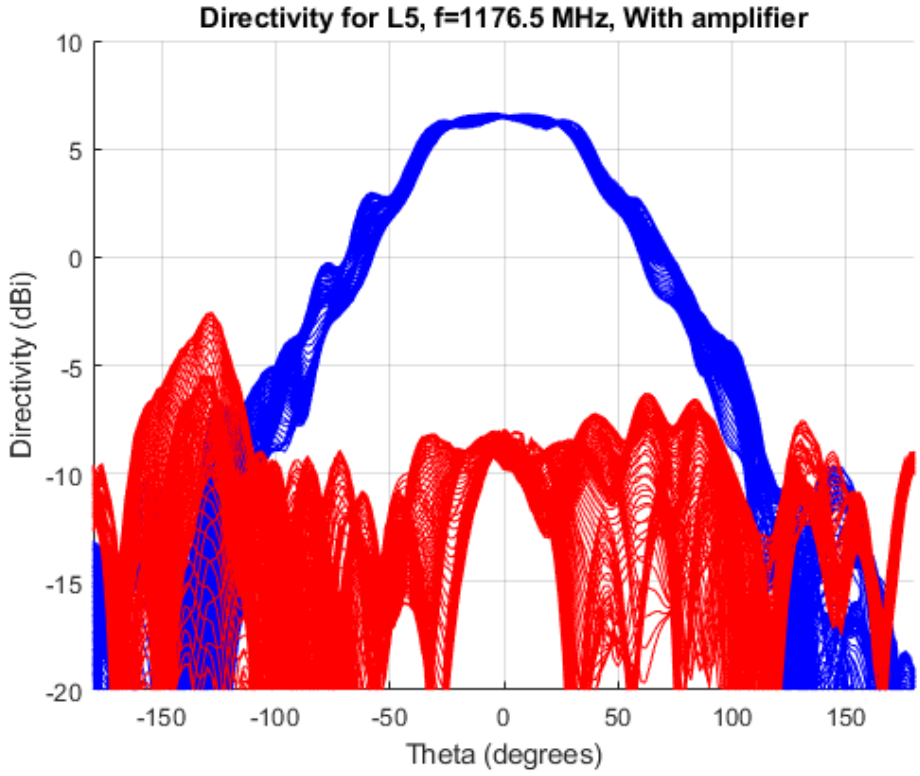

Figure 7.19: Directivity for L5, Blue: Co-pol (RHCP), Red: Cross-pol (LHCP).

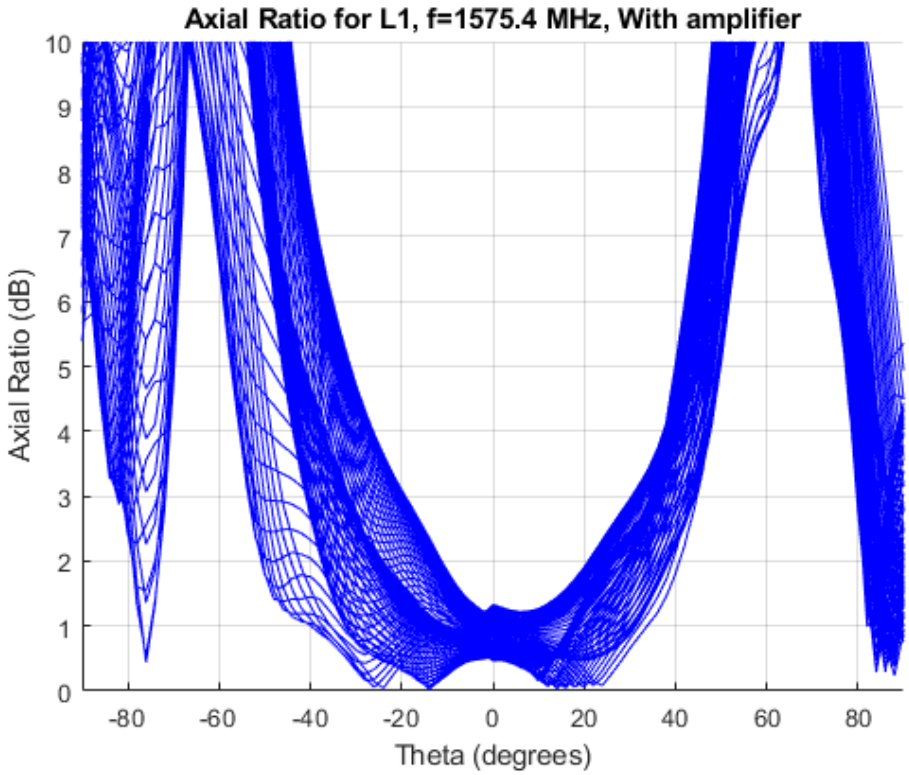

Figure 7.20: Axial ratio for L1, Blue: Co-pol (RHCP), Red: Cross-pol (LHCP).

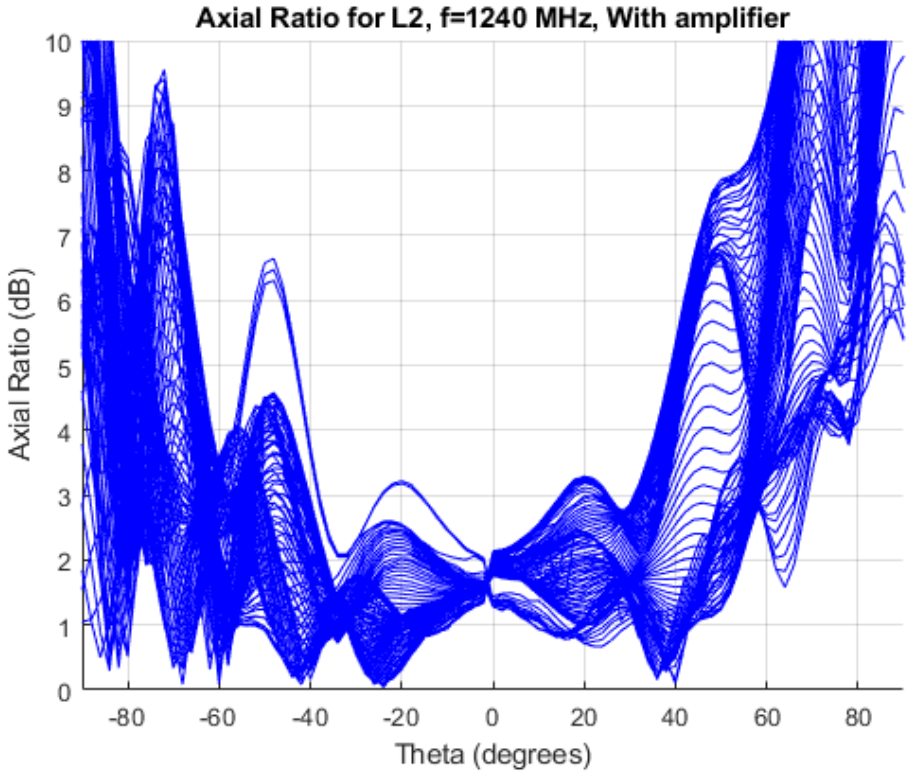

Figure 7.21: Axial ratio for L2, Blue: Co-pol (RHCP), Red: Cross-pol (LHCP).

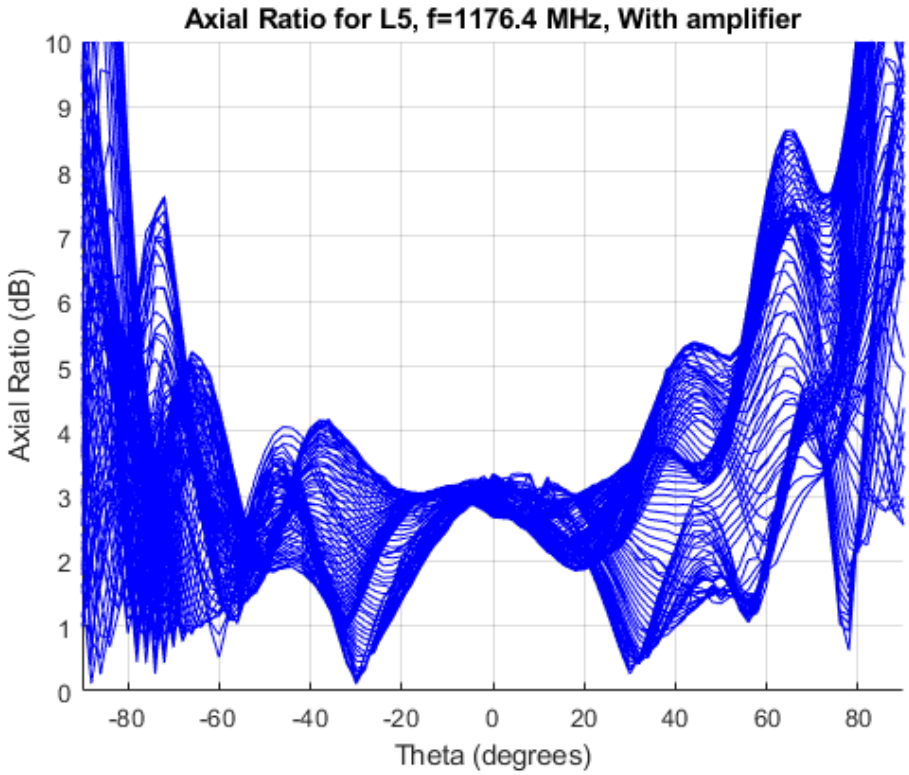

Figure 7.22: Axial ratio for L5, Blue: Co-pol (RHCP), Red: Cross-pol (LHCP).

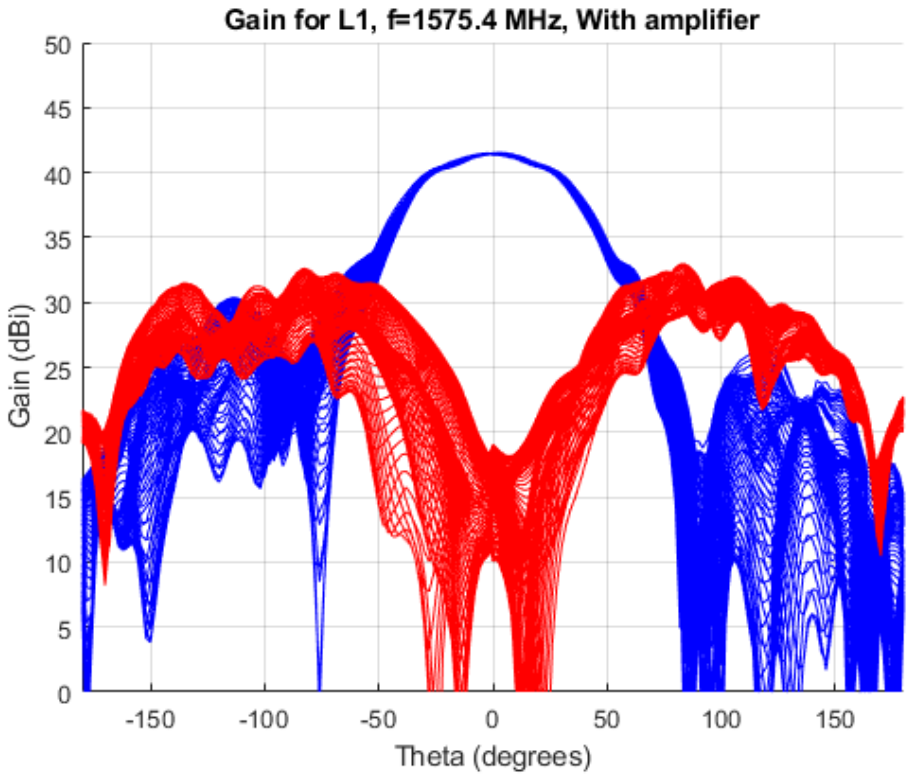

Figure 7.23: Actual gain for L1, Blue: Co-pol (RHCP), Red: Cross-pol (LHCP).

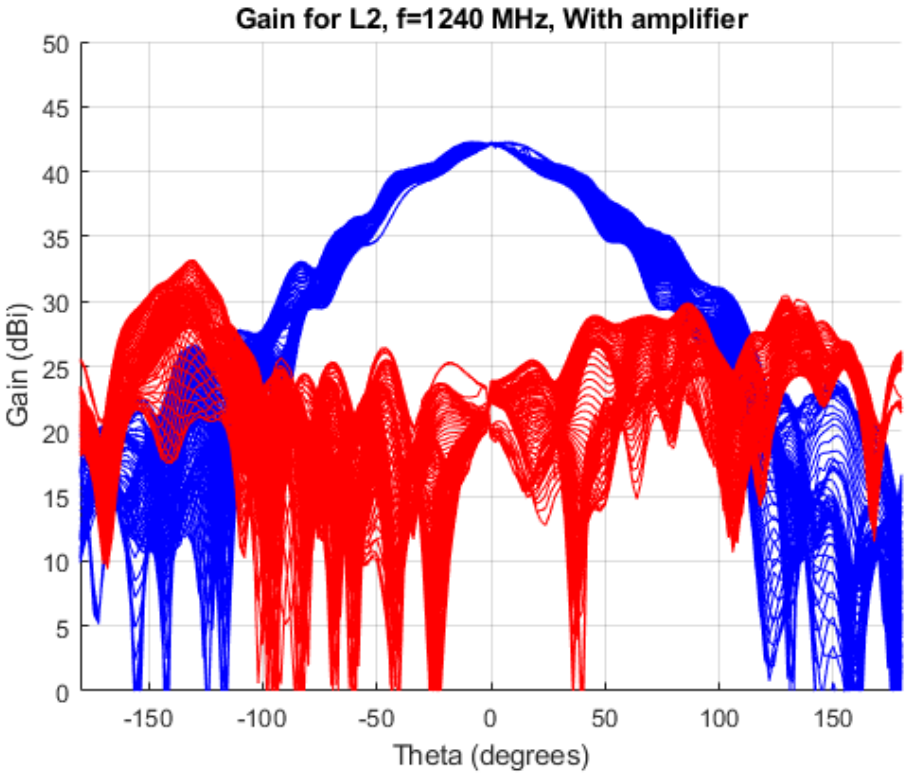

Figure 7.24: Actual gain for L2, Blue: Co-pol (RHCP), Red: Cross-pol (LHCP).

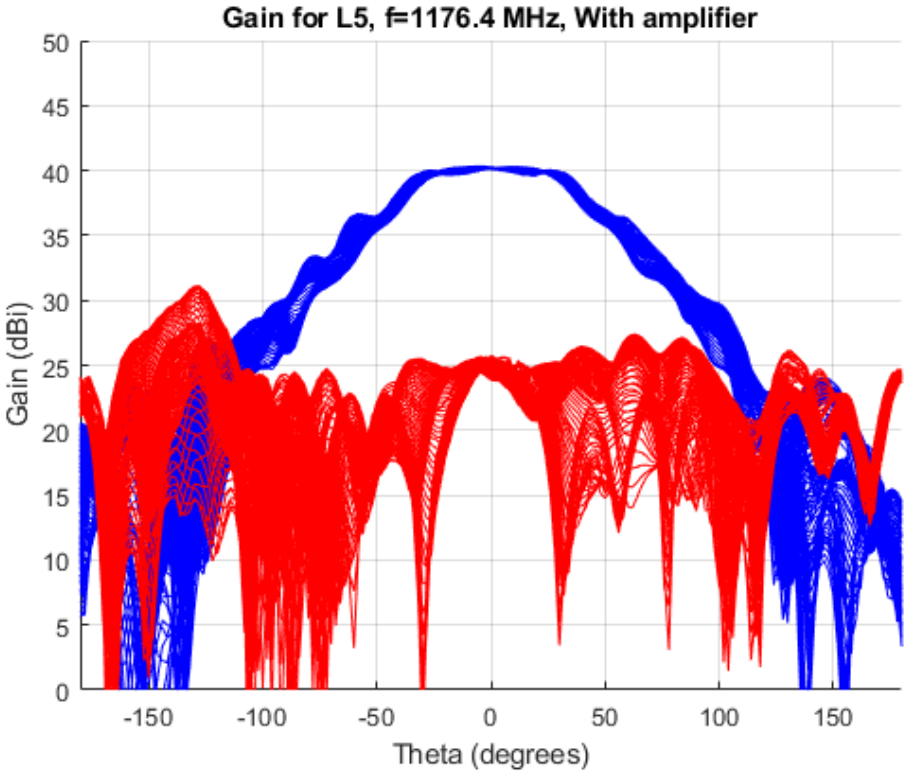

Figure 7.25: Actual gain for L5, Blue: Co-pol (RHCP), Red: Cross-pol (LHCP).

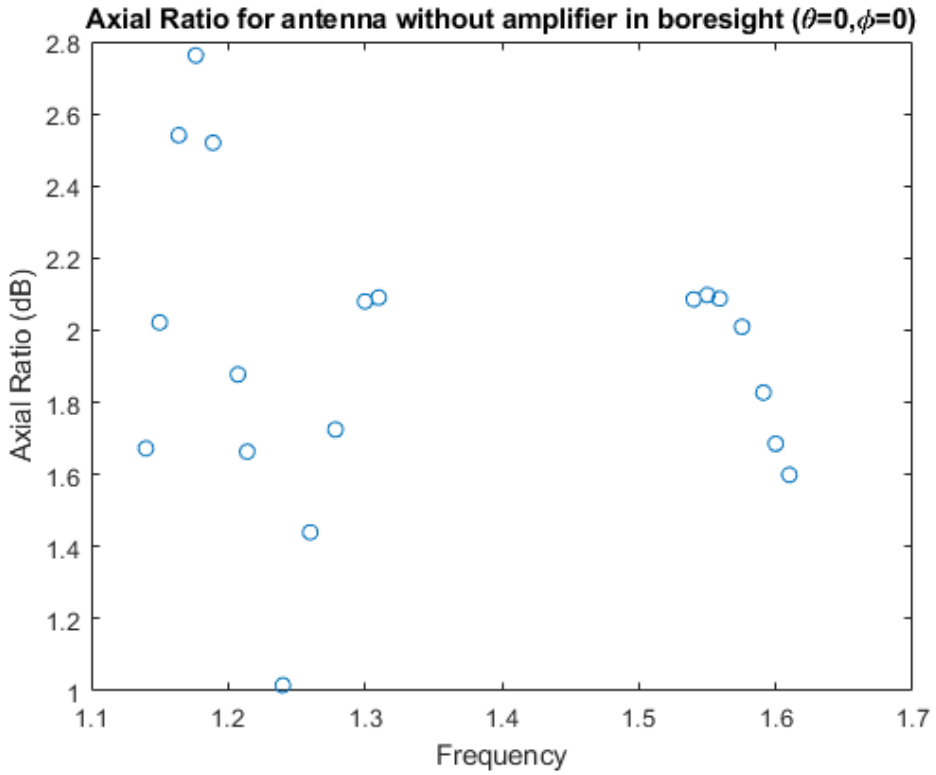

Figure 7.26: Axial Ratio at each measured frequency of the antenna without LNA.

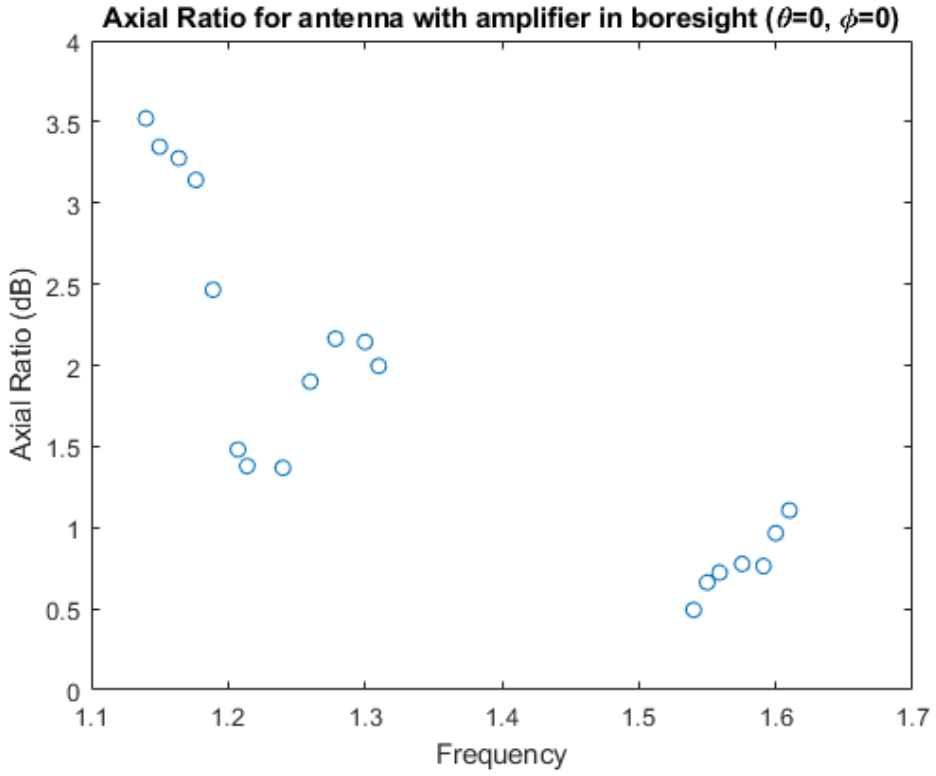

Figure 7.27: Axial Ratio at each measured frequency of the antenna with LNA.

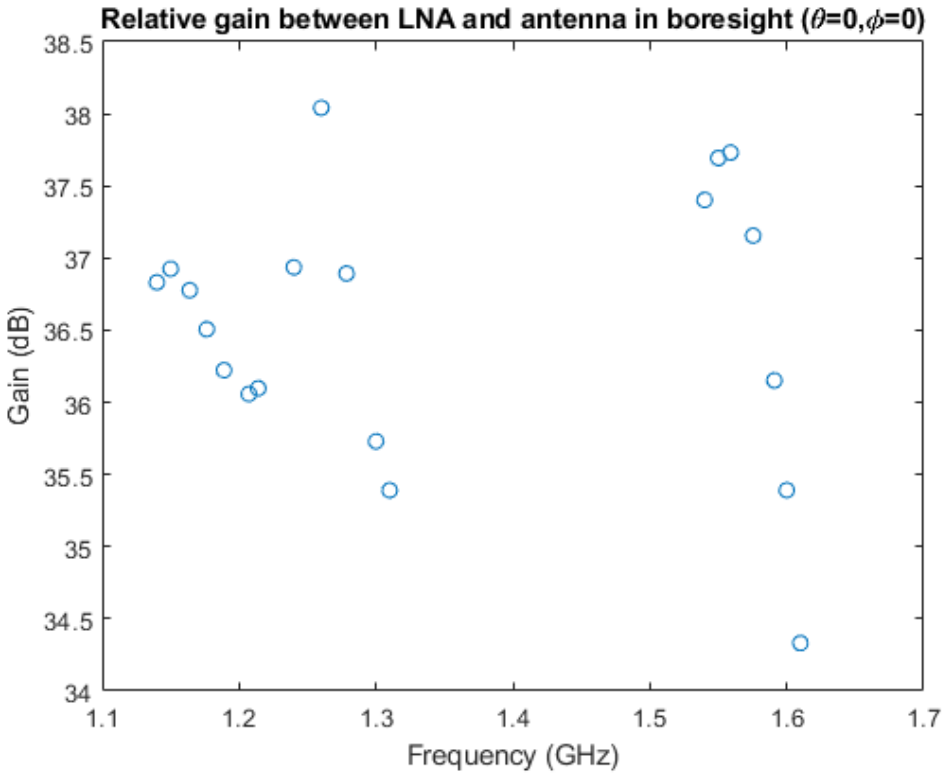

Figure 7.28: Relative gain between the LNA and antenna.

8

Discussion

In any project containing construction of an analog system, there will always be refinements to be made after the physical circuit has been manufactured. In our case we have found multiple upgrades to certain parts of each subdivision of this project (Antenna, Feeding Network and LNA) respectively. But initiating with the results: the first realization was made while conducting measurements on the circuitry on the antenna and LNA separately. Simulations for systems (Antenna and feeding network) containing only passive components tend to show quite an accurate result compared to the actual measurements made. The return loss for the output port of the antenna is closely related to the simulated FEM results acquired from HFSS as can be seen in the figures below.

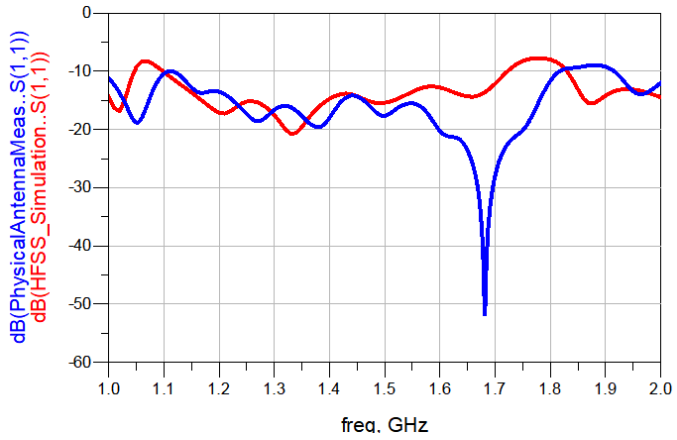

Figure 8.1: Antenna without LNA, measured results (blue), simulated results (red).

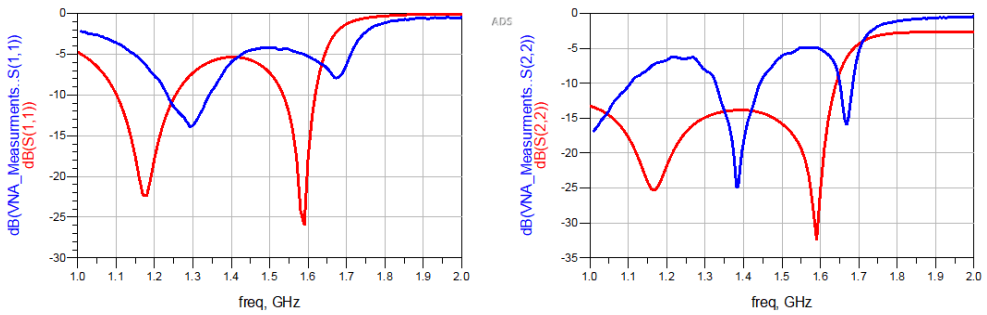

Figure 8.2: LNA separated from antenna, measured results (blue), simulated results (red), for S_{11} (left) and S_{22} (right).

The measurement of the antenna closely corresponds to the simulated results while the simulated results of the LNA circuit is frequency shifted by almost 300 MHz, see figure 8.2 in the lower GPS L5 band, and by roughly 100 MHZ for the upper GPS L1 band. The larger difference in measurements can be attained due to multiple variables. But the first one is that we modeled the dielectric constant ϵ_r of the FR4 material incorrectly. During the simulations we have been modeling with ϵ_r=4.4-4.6, since it is the most common constant to use in both HFSS and ADS.

After conducting the measurements we revised amongst eachother different parameters that could have been the root to the large frequency mismatch and came to the conclusion that the FR4 substrate provided from the manufacturer cogra has a lot lower dielectric constant of 4.05 than we had simulated. And even though they specify the ϵ_r of their material being 4.05, since FR4 is a volatile material having a high tolerance the absolute dieletric constant could still vary to be as low as 3.95 or 3.9. So the first phase of fine-tuning was deducted by performing new simulations in ADS with a new dielectric constant of the FR4 material and subsequently tuning and optimizing new parameter values for new components for the matching sections to realize a low input and output return loss (S_{11} and S_{22}) for the LNA section.

A total of 15 iterations of soldering new components had to be performed before we saw a somewhat close resemblance to the simulated results from ADS. The large amount of times needed for "re-soldering" is mainly due to the poor components, mainly conductors and inductors, found at beyond gravity. Since the components are not for space applications they often had a very high tolerance even for low reactance components. Subsequently this means that a capacitor with a reactance of 0.5 pF has a tolerance of +/- 0.25 pF, meaning that even though a correct component is chosen for our intended design the result from our measurement could differ quite alot from the simulated results. By tuning each component individually we could see what type of behaviour was to be expected if a component value was shifted by fractions of a pF or nH. For most components the change of 0.25 pF/nH had no large overall behaviour change for the input and output return loss, but for some vital components there was not only a big change in behaviour of the overall characteristics but also quite a large frequency shift for both S_{11} and S_{22}. Therefore we had to use the "trial-and-error" method in order to slowly obtain the intended results. It is worth to mention that we only used the poor components found at the office in order to know what type of components to order (having less tolerance and therefore being more reliable).

Another reoccurring issue has been to perform simulations in HFSS. At beyond gravity there has been a computer to perform simulations in HFSS, but there has been high competition to simulate circuits on the said computer. We attempted to do the simulations via student licenses on our own personal computers, but there are limitations on the maximum number of mesh elements which was exceeded when executing simulations on the latter stages of combining the feed network with the antenna element, leaving us to do all simulations via the computers available at Chalmers.

During the early stages where we had to test different parameters of the antenna this more often than not meant that we had to do rather large parametric analyzes in order to minimize the return loss of the output ports of the antenna design. On multiple occurrences the remote connection was either interrupted due to connection errors or another student connecting to the computer physically resulting in us having to redo simulations again which proved to be quite time consuming. There were also problems with corrupt files for our design related to connecitivity issues and us having to login via a new remote connection. This effectively led to more stress due to the already narrow time constriction for the project overall.

The measurements conducted in the anechoic chamber are closely resembled to the ones we saw during simulations, where we expected an axial ratio of 3 dB or lower in the entire band and a gain of over 3 dB in boresight for all frequencies. In boresight the ratio between co and cross polarization reaches an acceptable level of roughly 15 dB, but when increasing θ to 40-50 degrees the co and cross polarization reaches almost the same level for some frequencies. In regular GNSS positioning this might pose an an issue if the antenna were placed on Earth for example, where reflected components of the transmitted RHCP polarization will take the form of the cross polarized LHCP component, which will result in a higher uncertainty when calculating the position of an object. For this type of design where the communication is between two satellites and the receiver is looking out in space, this will not cause any issues due to the transmitter having roughly a 20-30 dB compression of unwanted LHCP transmitted components compared to the RHCP, something we have discussed with our supervisors.

8.1 Future work

One especially interesting article [13] has solved the issue of retaining a stable power division over a wide bandwidth for both output ports of the Schiffmann phase shifter. As could be seen from simulations when increasing the frequency the deviation in power from the common input port to the output ports P2, Coupled Line Coupler (CLC) section and P3, transmission line section of the Schiffman phase shifter increased exponentionally mainly due to the decreased width of the coupled line section resulting in a higher impedance of the section compared to that of the transmission line section. The wideband balun type design in [13] makes use of shorted and open $\frac{\lambda}{8}$ stubs before and after the meander line section, i.e the CLC-section of their feeding network design resulting in a maximum relative phase deviation of +/- 6° and a maximum amplitude deviation of +/- 0.3 dB. This is something that we would have liked to implement but could not due to time constrictions. Our design currently has a maximum amplitude deviation of roughly +/- 2dB while having a maximum relative phase deviation of +/- 5°.

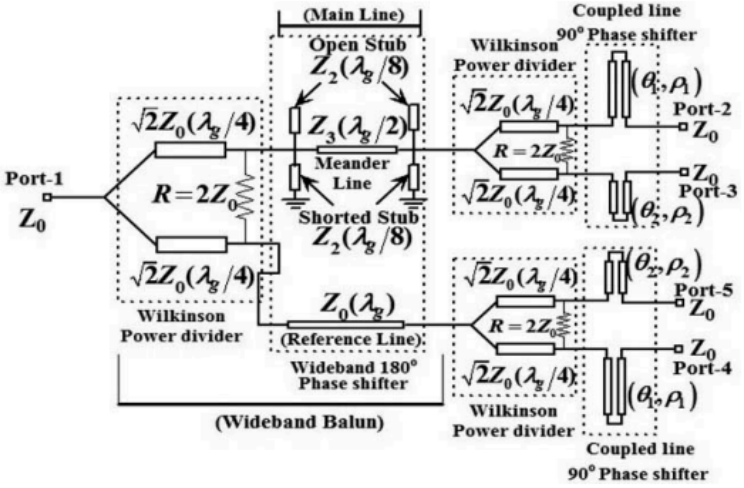

Figure 8.3: Electrical circuit for the wideband balun design, from [13]

Narrowing the width of the CLC-section provided less phase deviation but subsequently caused issues regarding power division. In the current state the design has a maximum power deviation (between P2 and P3) at the lower and upper frequency band since the design is designed to have equal power division at a frequency of 1.385 GHz (inbetween the L1 and L5 band). The maximum difference simulated is estimated to be somewhere between 1 to 1.5 dB, but when simulating for higher and lower frequencies outside the band it was seen that the power division will be a problem for a potential future design if one were to manufacture an even more wideband design to include ISM/Bluetooth or Wi-Fi bands.

9
Conclusion

As can be seen from table 3.1, all specified antenna specifications have been achieved except for the gain for a θ angle over 65 and 80 degrees respectively. In boresight the directivity and gain is above 3 dB, although the gain is 2-3 dB lower than the directivity of 6-7 dB due to losses in transmission lines which is to be expected. The return loss of the input and output matching sections of the LNA do not align perfectly in frequency, but are frequency shifted slightly relative to each other, see figure 7.4. This can be resolved if more time is spent on tuning the components. The noise figure is below 0.7 dB in the lower L5 band, but reaches as high as 2.5 dB in the upper frequency (L1) band. The high noise figure in the upper frequency band is most likely due to three factors. The frequency band being shifted slightly combined with the Q-value being higher than the ones used in simulations resulting in higher resistivity in the actual components used, increasing the overall noise. Finally the stabilization method utilized in this design most likely is not the most suited to suppress noise, since simulations show that a high resistor on the input section is required to ensure stability.

Bibliography

[1] J. Sanz Subirana, JM. Juan Zornoza and M. Hernandez-Pajares, "GPS, Glonass and Galileo Frequency bands." [Online]. Available: https://gssc.esa.int/navipedia/index.php/GNSS_signal

[2] Unknown Editor, "S-parameters." [Online]. Available: https://www.microwaves101.com/encyclopedias/s-parameters

[3] D.M. Pozar, "Microwave Engineering, Wiley, 2012. ProQuest Ebook Central,." [Online]. Available: https://ebookcentral.proquest.com/lib/chalmers/detail.action?docID=2064708

[4] everything RF, "What is an Anechoic Chamber?" [Online]. Available: https://www.everythingrf.com/community/what-is-an-anechoic-chamber

[5] Antenna Test Lab Company 2021, "Measuring Passive Antenna Gain." [Online]. Available: https://antennatestlab.com/antenna-education-tutorials/gain-dbi-passive-antenna

[6] E. Pelliccia, R. Vincenti Gatti, P. Angeletti, G. Toso, "A Dual-Band Circularly Polarized Patch Array Antenna for Phase-Only Beam Shaping with Element Rotation. Electronics 2021, 10, 643." [Online]. Available: https://doi.org/10.3390/electronics10060643

[7] M. Awais, A. Bilal, and S. Salamat, "A Low Cost Coplanar Capacitively Coupled Probe Fed Stacked Patch Antenna for GNSS Applications," Progress In Electromagnetics Research Letters, Vol. 99, 11-18, 2021." [Online]. Available: https://www.jpier.org/PIERL/pier.php?paper=21050306

[8] Y. Guo, K. Khoo and L. C. Ong, "Wideband Circularly Polarized Patch Antenna Using Broadband Baluns, in IEEE Transactions on Antennas and Propagation, vol. 56, no. 2, pp. 319-326, Feb. 2008." [Online]. Available: https://doi.org/10.1109/TAP.2007.915427

[9] S. Gao, L. Qi, Z. Fuguo, "Circularly Polarized Antennas, New York : John Wiley Sons, Incorporated, 2014. [Online]." [Online]. Available: https://ebookcentral.proquest.com/lib/chalmers/detail.action?docID=1527856

[10] Stündle, "Wilkinson Power Divider." [Online]. Available: https://en.wikipedia.org/wiki/Wilkinson_power_divider

[11] ——, "Rat Race coupler." [Online]. Available: https://en.wikipedia.org/wiki/Rat-race_coupler

[12] Avago Technologies, "Characteristics of E-pHEMT vs. HBTs." [Online]. Available: https://www.eeweb.com/characteristics-of-e-phemt-vs-hbts/Accessed: April20,2022

[13] B. Dwivedy, SK. Behera,D. Mishra, "Wideband multiple phase shift quad feed network for polarization reconfigurable antennas, Electromagnetics, vol. 37,

no. 8, pp. 483–492." [Online]. Available: https://doi.org/10.1080/02726343.2017.1392708

[14] F. Tamjid, F. Foroughian, C. M. Thomas, A. Ghahreamani, R. Kazemi and A. E. Fathy, "Toward High-Performance Wideband GNSS Antennas-Design Tradeoffs and Development of Wideband Feed Network Structure," in IEEE Transactions on Antennas and Propagation, vol. 68, no. 8, pp. 5796-5806." [Online]. Available: https://doi.org/10.1109/TAP.2020.2983800

[15] U. U. Hussine, Y. Huang and C. Song, "A new circularly polarized antenna for GNSS applications," 2017 11th European Conference on Antennas and Propagation (EUCAP), 2017, pp. 1954-1956." [Online]. Available: https://doi.org/10.23919/EuCAP.2017.7928742

[16] P-S.Kildal, "Foundations of Antenna Engineering: A Unified Approach for Line-of-Sight and Multipath, Artech House." [Online]. Available: https://ebookcentral.proquest.com/lib/chalmers/detail.action?docID=4537960

[17] Ansys, "Ansys HFSS Best-In-Class 3D High Frequency Electromagnetic Simulation Software." [Online]. Available: https://www.ansys.com/products/electronics/ansys-hfss

[18] Electronics-notes.com, "What is an Anechoic Chamber?" [Online]. Available: https://www.electronics-notes.com/articles/test-methods/rf-vector-network-analyzer-vna/what-is-a-vna.php

[19] A. Balanis, "Antenna Theory: Analysis and Design, 4th ed., Hoboken, NJ, USA: John Wiley Sons, Incorporated, 2016. [Online]." [Online]. Available: https://ebookcentral.proquest.com/lib/chalmers/detail.action?docID=4205879

[20] A. A. M. Shah Sadman and M. Hossam-E-Haider, "Design of a 2 × 3 Microstrip Patch Phased Array Antenna for GNSS Augmentation, 2020 23rd International Conference on Computer and Information Technology (ICCIT), 2020, pp. 1-6,." [Online]. Available: https://doi.org/10.1109/ICCIT51783.2020.9392680

[21] W. L. Langston, D. R. Jackson, "Impedance, axial-ratio, and receive-power bandwidths of microstrip antennas," IEEE Antennas and Propagation Society International Symposium (IEEE Cat. No.02CH37313), 2002, pp. 882-885 vol.2." [Online]. Available: https://doi.org/10.1109/APS.2002.1016786

[22] B. M. Schiffman, "A New Class of Broad-Band Microwave 90-Degree Phase Shifters,in IRE Transactions on Microwave Theory and Techniques, vol. 6, no. 2, pp. 232-237, April 1958." [Online]. Available: https://doi.org/10.1109/TMTT.1958.1124543

[23] J. Quirarte and J. Starski, "Novel schiffman phase shifters," *IEEE Transactions on Microwave Theory and Techniques*, vol. 41, no. 1, pp. 9–14, 1993.

[24] J.U.R Kazim et al., "A Miniaturized 3dB Rat-Race Coupler Utilizing Meandered Lines, 2021 1st International Conference on Microwave, Antennas Circuits (ICMAC)." [Online]. Available: 10.1109/ICMAC54080.2021.9678260

[25] Faaiqah Kamsaini, "Design and Development of Two-stage Low-noise Amplifier (LNA) using E-pHEMT Technology for C-band Application." [Online]. Available: https://doi.org/10.1088/1757-899X/864/1/0121260

10

Appendix 1

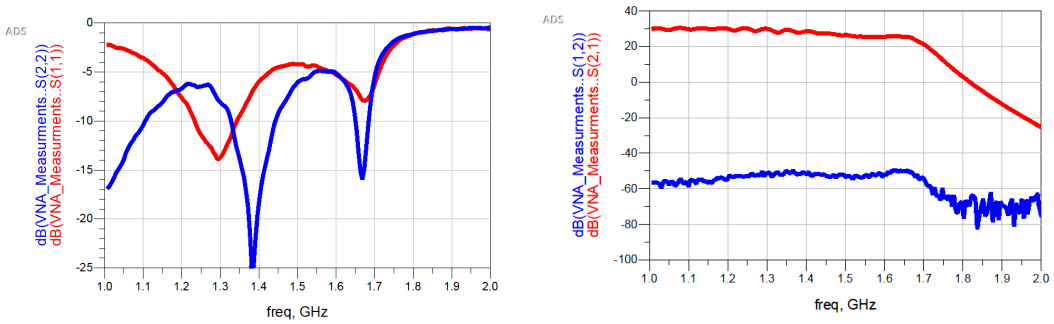

Figure 10.1: First VNA measurements of LNA circuit. S_{11} and S_{22} (left), S_{12} and S_{21} (right).

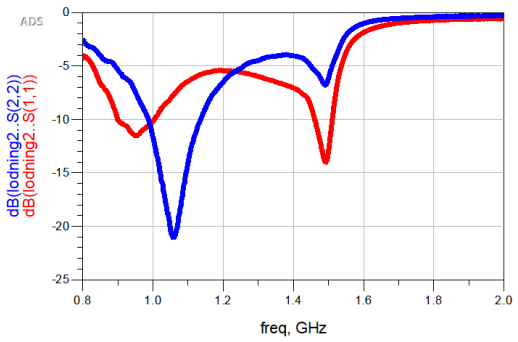

Figure 10.2: Second VNA measurements of LNA circuit. S_{11} and S_{22}.

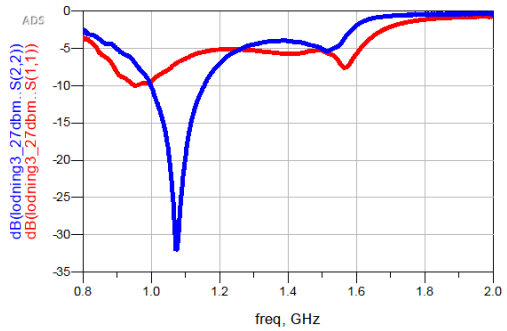

Figure 10.3: Third VNA measurements of LNA circuit. S_{11} and S_{22}.

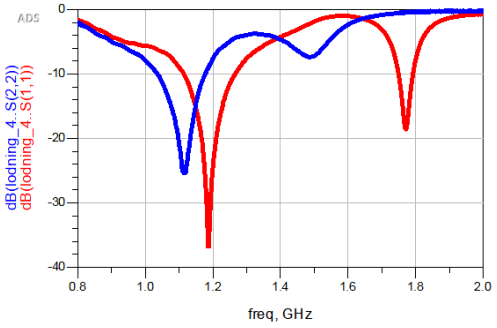

Figure 10.4: Fourth VNA measurements of LNA circuit. S_{11} and S_{22}.

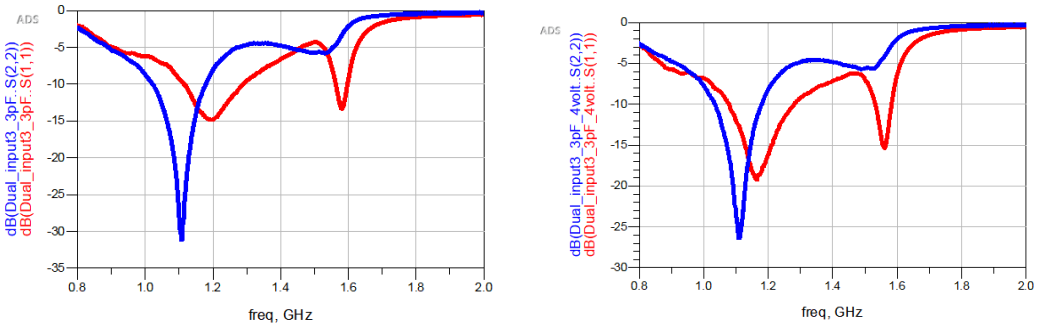

Figure 10.5: Fifth VNA measurements of LNA circuit. S_{11} and S_{22} 3V (left), 4V (right).

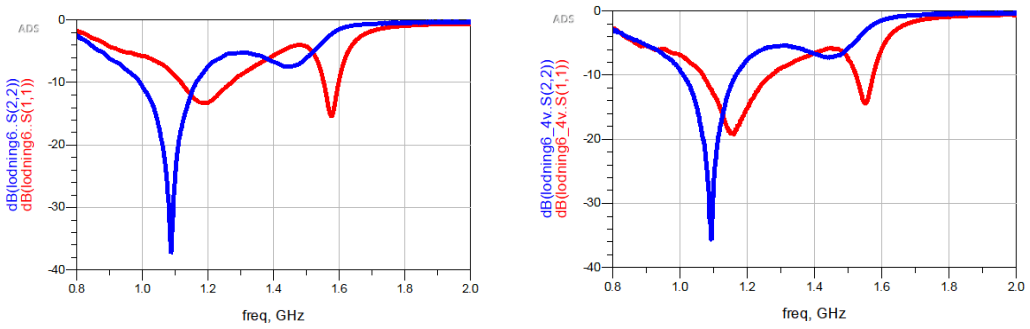

Figure 10.6: Sixth VNA measurements of LNA circuit. S_{11} and S_{22} 3V (left), 4V (right).

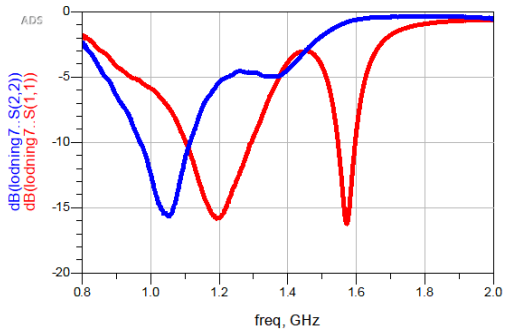

Figure 10.7: Seventh VNA measurements of LNA circuit. S_{11} and S_{22}

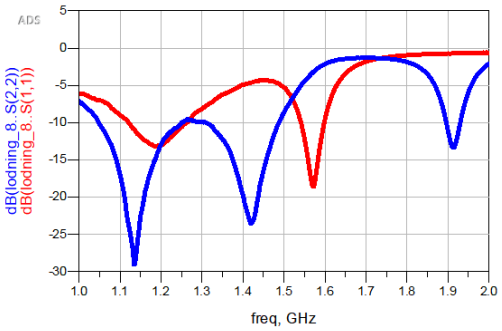

Figure 10.8: Eigth VNA measurements of LNA circuit. S_{11} and S_{22}

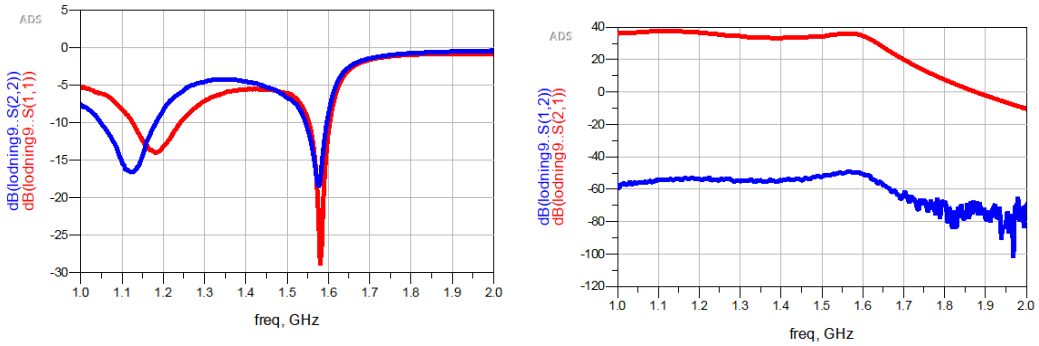

Figure 10.9: Ninth VNA measurements of LNA circuit. S_{11} and S_{22} (left), S_{12} and S_{21} (right).

DEPARTMENT OF SOME MICROTECHNOLOGY AND NANOSCIENCE
CHALMERS UNIVERSITY OF TECHNOLOGY
Gothenburg, Sweden
www.chalmers.se

CHALMERS
UNIVERSITY OF TECHNOLOGY